DIFFERENTIAL STRAIN ANALYSIS: APPLICATION TO SHOCK
INDUCED MICROFRACTURES

by

ROBERT WAYNE SIEGFRIED, II

B.S., California Institute of Technology
(1972)

SUBMITTED IN PARTIAL FULFILLMENT
OF THE REQUIREMENTS FOR THE
DEGREE OF

DOCTOR OF PHILOSOPHY

at the

MASSACHUSETTS INSTITUTE OF TECHNOLOGY

(February, 1977)

Signature redacted

Signature of Author . .
                              Department of Earth and Planetary Sciences
                                                      December 28, 1976

Signature redacted

Certified by . . .
                                                      Thesis Supervisor

Signature redacted

Accepted by .
              Chairman, Departmental Committee on Graduate Students

DIFFERENTIAL STRAIN ANALYSIS: APPLICATION TO SHOCK
INDUCED MICROFRACTURES

by

ROBERT WAYNE SIEGFRIED, II

Submitted to the Department of Earth and Planetary Sciences

on December 28, 1976 in partial fulfillment of the requirements

for the Degree of Doctor of Philosophy

ABSTRACT

Microcracks control the behavior of many physical pro-
perties of rocks at pressures below a few kilobars, corre-
sponding to depths of about 10 km on the earth and up to 50 km
on the moon. The differential strain analysis (DSA) technique
was developed to characterize microcracks with respect to
closure pressure and orientation. The DSA technique allows
detailed study of the crack distributions produced by various
processes, and the effect of these cracks on elastic
properties.

The crack distributions in two suites of rock samples
that had been subjected to known conditions of shock loading
were characterized with DSA. The qualitative effect of
parameters such as mineralogy, grain size, initial crack
distribution, shock pressure, and shock duration on the shock-
induced crack distribution in a rock sample was determined.

Comparison of the crack distributions in six returned
lunar samples with those of the experimentally shocked samples
indicates that the crack distribution in situ in the lunar
crust is likely to be different than that in the returned
samples. Thus, measurements of the elastic properties of
returned lunar samples as a function of pressure should not
be used directly to estimate the variation of elastic pro-
perties with depth in the moon.

Name and Title of Thesis Supervisor: Gene Simmons,
                                       Professor of Geophysics

TABLE OF CONTENTS

Chapter 1

Introduction

One primary aim of the study of physical properties of rocks, especially as a function of pressure and temperature, is to interpret measurements made in situ of such parameters as velocity of elastic waves, temperature, and electrical conductivity in terms of rock type and physical state. In order to apply meaningfully laboratory measurements to the interpretation of field data, the parameters that control particular physical properties must be discovered and characterized both in the lab and in the field.

The physical properties of rocks are controlled both by the properties of their constituent minerals and the textural manner in which these minerals are assembled to form a rock. Voids in the form of pores and cracks exert a particularly large influence on elastic properties (e.g. elastic wave velocities, compressibility) since the elastic properties of common rock forming minerals differ little from each other as compared to the contrast in properties between these minerals and an air or liquid filled void. Adams and Williamson (1923) were first to attribute the strong pressure dependence of elastic velocities to the presence of cracks, and several subsequent authors have reaffirmed the importance of cracks in controlling the physical properties of rocks at low pressures (e.g. Thill et al., 1969; Brace, 1965; Simmons, 1964a and b; Birch, 1960 and 1961).

We have developed a technique, termed differential strain

analysis (DSA) for characterizing the cracks in rocks in terms of porosity, closure pressure, and orientation. The technique is described in Simmons et al. (1974) and more fully in Chapter 2 of this thesis.

Simmons et al. (1975) use the DSA technique to show that the crack distributions in the returned lunar samples differ substantially from the distributions in typical terrestrial igneous rocks, including some shocked samples. Possible causes for this difference include multiple shocking on the lunar surface, differences in the duration and intensity of lunar and terrestrial shock processes, differences in the pre-shock crack distributions of lunar and terrestrial rocks, and the presence in the returned lunar samples of cracks formed when the sample was excavated by a shock event. If the latter effect is important, the crack distributions in the returned samples could differ significantly from the crack distribution in situ on the moon. Thus, the procedure of directly applying laboratory physical property measurements to the interpretation of lunar seismic data, as practiced by Toksöz et al. (1973), Trice et al. (1974), Simmons et al. (1973) and others might be inappropriate.

In order to help assess the importance of the various crack producing processes operating on the moon, we have attempted to determine the relation between shock induced microcrack distributions and such factors as pre-shock porosity, grain size, shock pressure, shock duration, and mineralogy. A qualitative knowledge of the way in which these parameters

affect shock-induced microfractures will allow us to make a meaningful interpretation of the crack distributions in lunar samples.

Shock effects in rocks, including shock induced microcracks, have been used for the recognition and study of terrestrial impact craters, as well as the study of the effects of underground nuclear explosions (Dence et al., 1968; Short, 1966, 1968; Borg, 1973). The correct interpretation of microfractures produced in such field situations requires knowledge of the parameters controlling shock induced microcrack distributions that can only be gained through experiments with controlled shock conditions and well characterized samples.

We have used the DSA technique to characterize the microfracture distributions in two sets of samples shocked under controlled conditions. In Chapter 3 we describe the microcracks produced in a set of samples having a range of initial crack porosity, mineralogy, and grain size that were subjected to similar shock conditions with an explosive driver plate apparatus. These experiments were performed to allow us to assess qualitatively the effect of various preshock sample parameters on shock induced crack distributions.

The samples studied in Chapter 4 are taken from a granite block shocked in a laboratory scale hypervelocity impact experiment. The rock samples are taken at various distances from the impact point so that the effect of shock pressures in the range from two to twenty kilobars on samples having identical initial characteristics can be determined.

Chapters 2 through 5 of this thesis have been prepared as individual manuscripts. Citations among the various chapters are therefore in manuscript form, including appropriate co-authors. All citations dated 1977 refer to various chapters of this thesis, as indicated below:

Siegfried and Simmons, 1977   Chapter 2

Siegfried, McQueen, and Simmons, 1977   Chapter 3

Siegfried, Hörz, and Simmons, 1977   Chapter 4

REFERENCES

Adams, L.H. and E.D. Williamson, On the compressibility of minerals and rocks at high pressures, Franklin Inst. J., 195, 475-529, 1923.

Birch, F., The velocity of compressional waves in rocks to 10 kilobars, part 1, J. Geophys. Res., 65, 1083-1102, 1960.

Birch, F., The velocity of compressional waves in rocks to 10 kilobars, part 2, J. Geophys. Res., 66, 2199-2224, 1961.

Borg, I.Y., Extent of pervasive fracturing around underground nuclear explosions, Int. J. Rock Mech. Min. Sci., 10, 11-18, 1973.

Brace, W.F., Some new measurements of linear compressibility of rocks, J. Geophys. Res., 70, 391-398, 1965.

Dence, M.R., M.J.S. Innes and P.B. Robertson, Recent geological and geophysical studies of Canadian craters, in Shock Metamorphism of Natural Materials, edited by B.M. French and N.M. Short, 339-362, Mono, Baltimore, Md., 1968.

Short, N.M., Effects of shock pressures from a nuclear explosion on mechanical and optical properties of granodiorite, J. Geophys. Res., 71, 1195-1215, 1966.

Short, N.M., Nuclear-explosion-induced mocrodeformation of rocks: An aid to the recognition of meteorite impact structures, in Shock Metamorphism of Natural Materials,

edited by B.M. French and N.M. Short, 185-210, Mono, Baltimore, Md.,1968.

Simmons, G., Velocity of compressional waves in various minerals at pressures to 10 kilobars, J. Geophys. Res., 69, 1117-1121, 1964a.

Simmons, G., Velocity of shear waves in rocks to 10 kilobars, 1, J. Geophys. Res., 69, 1123-1130, 1964b.

Simmons, G., T. Todd, and H. Wang, The 25-km discontinuity: implications for lunar history, Science, 182, 158-161, 1973.

Simmons, G., R. Siegfried, and D. Richter, Characteristics of microcracks in lunar samples, Proc. Sixth Lunar Sci. Conf., 3, 3227-3254, 1975.

Simmons, G., R. Siegfried, and M. Feves, Differential strain analysis: a new method for examining cracks in rocks, J. Geophys. Res., 79, 4383-4385, 1974.

Thill, R.E., R.J. Willard, and T.R. Bur, Correlation of longitudinal velocity variation with rock fabric, J. Geophys. Res., 74, 4897-4909, 1969.

Toksöz, M.N., A.M. Dainty, S.C. Solomon, and K.R. Anderson, Velocity structure and evolution of the moon, Proc. Fourth Lunar Sci. Conf., Geochim. Cosmochim. Acta, suppl. 4, vol. 3, 2529-2547, 1973.

Trice, R., N. Warren, and O.L. Anderson, Rock elastic properties and near-surface structure at Taurus-Littrow, Proc. Fifth Lunar Sci. Conf., Geochim. Cosmochim. Acta, suppl. 5, vol. 3, 2903-2911, 1974.

Chapter 2

Characterization of Oriented Cracks with

Differential Strain Analysis

INTRODUCTION

The precise characterization of microcracks in rocks is important in geology and geophysics for several reasons. Many workers have shown previously that microcracks dominate the behaviour of the physical properties of rocks at pressures below several kilobars (Adams and Williamson, 1923; Thill et al., 1969; Brace, 1965; Simmons, 1964a and b; Birch, 1960 and 1961; for example). Knowledge of the nature of the crack population with depth in situ is essential in correctly interpreting field measurements of such physical properties as seismic velocity and electrical conductivity. In addition, microcracks in a rock can be used to study its past history (Simmons and Richter, 1976; Richter et al., 1976; Batzle and Simmons, 1976).

The new technique, differential strain analysis (DSA) (Simmons, et al., 1974), was developed to characterize the distribution of crack porosity with crack closure pressure in a rock sample. We have used it on about 75 samples and have extended it to obtain information about crack orientation as a function of closure pressure. In this paper, we describe its present state.

In differential strain analysis, linear strain under hydrostatic loading is measured in several directions with very high precision. The surfaces of a sample are handlapped and BLH SR-4 foil electric resistance strain gauges are mounted directly on the sample surface with Tra-Con 2101 epoxy. The sample is vacuum dried at 40°C and 10^{-2} torr and then vented with dry nitrogen and

encapsulated in Dow-Corning sylgard 186 to exclude the pressure medium (hydraulic oil). A fused silica sample is prepared similarly to the rock sample and exposed to the same pressure conditions. The strain in the fused silica sample is then subtracted (during data processing) from the strain in the rock sample in order to eliminate errors due to instrument drift, variations in lead resistance, etc. If the actual strain curve of the rock is desired, it can be calculated from the differential strain curve using measurements of the compressibility of fused silica vs. pressure (Peselnick et al., 1967).

Walsh (1965) derived expressions relating volumetric crack porosity and crack aspect ratio to compressibility. Morlier (1971) used Walsh's results to show that the distribution function for crack porosity vs. aspect ratio could be obtained from the strain vs. pressure curve. Both Walsh and Morlier used elliptical and penny-shaped models for cracks. Because we have not observed any elliptical or penny-shaped cracks in the thirty rocks that we have examined with scanning electron microscopes, we prefer to describe our results using parameters which are independent of a specific model for crack shape. Instead of aspect ratio, we use closure pressure, defined as the pressure at which a crack closes completely. For elliptical and penny-shaped models, closure pressure (P_c) is related to aspect ratio (α) by the relation:

$$P_c = nE\alpha$$

where E is the matrix Young's modulus and n is a dimensionless constant on the order of 1, which depends on whether a plane stress, plane strain, or penny-shaped model is used (Walsh, 1965).

The basic quantity obtained from DSA data is the zero pressure strain tensor in a sample due to the presence of cracks that close at a given pressure. The trace of this tensor is the volumetric strain (or crack porosity) due to cracks that close at the particular pressure. The volumetric strain can be determined with only three orthogonal gauges on a sample. One gauge on a sample allows determination of the zero pressure linear strain in the direction of the gauge due to cracks closing at a given pressure.

THEORETICAL BASIS OF DSA

Walsh (1965) calculated volumetric compressibility for a rock containing elliptical or penny-shaped cracks. We have extended his method to the calculation of the compressibility tensor, replacing the penny-shaped or elliptical crack models with the more general assumption of linear crack closure. Linear crack closure means that strain is linear over any pressure range in which no cracks close completely. This assumption is verified experimentally (at least for low-porosity igneous rocks) by the observation that the strain curves of some rocks are linear over pressure ranges of several hundred bars. The other assumptions include a homogeneous distribution of non-interacting cracks in a homogeneous, isotropic matrix. We use this approach rather than those approaches which include crack interactions (e.g., the self-consistent approach of O'Connell and Budiansky, (1974)) due to the simplicity involved in inverting the strain data to obtain crack parameters. We believe that this approach is satisfactory in igneous rocks where crack porosities are at most a few percent.

Definition of terms:

ε_{ij} = strain tensor of cracked solid

$\hat{\varepsilon}_{ij}$ = differential strain tensor

ε_{ij}^{m} = average matrix strain of solid

η_{ij} = strain due to the presence of cracks

$\zeta_{ij}(P_c)$ = zero pressure strain due to the presence of cracks closing completely at $P \leq P_c$

$\nu_{ij}(P_c)dP_c$ = zero pressure strain due to the presence of cracks closing between P_c and $P_c + dP_c$

$$(\nu_{ij} = d\zeta_{ij}/dP_c)$$

β_{ij} = compressibility tensor of cracked solid

β_v^m = volumetric compressibility of matrix material

If a pressure increment δP is applied to a solid, the incremental strain due to the presence of cracks is the difference between the observed strain and the average matrix strain:

$$\delta\eta_{ij} = \delta\varepsilon_{ij} - \delta\varepsilon_{ij}^m \tag{1}$$

Betti's reciprocal theorem (Love, 1927) allows us to calculate the average matrix strain of a porous solid under hydrostatic pressure P. Consider a volume (V) of solid containing one pore under two states of stress (figure 1). In the first state (unprimed) the solid is under hydrostatic pressure δP at the outer boundary and zero pressure at the pore boundary. The resulting strain field is $\delta\varepsilon_{ij}$. In the second stress state (primed) surface tractions are applied so that the single stress component $\delta\sigma'_{IJ}$ is uniform throughout the solid and all other stress components vanish. The subscripts I and J correspond to the average matrix strain component $\delta\varepsilon_{IJ}$ which is to be calculated. The resultant strain is $\delta\varepsilon'_{ij}$. The reciprocal theorem states that the strain energy of a given stress field acting through the displacement produced by a second stress field is equal to the strain energy of the second stress field acting through the displacement produced by the first stress field; or in this case:

$$\iiint_{\text{matrix}} \delta\varepsilon_{IJ}\delta\sigma'_{IJ}dV = \iint_S \delta\sigma_n \delta\varepsilon'_n dS \tag{2}$$
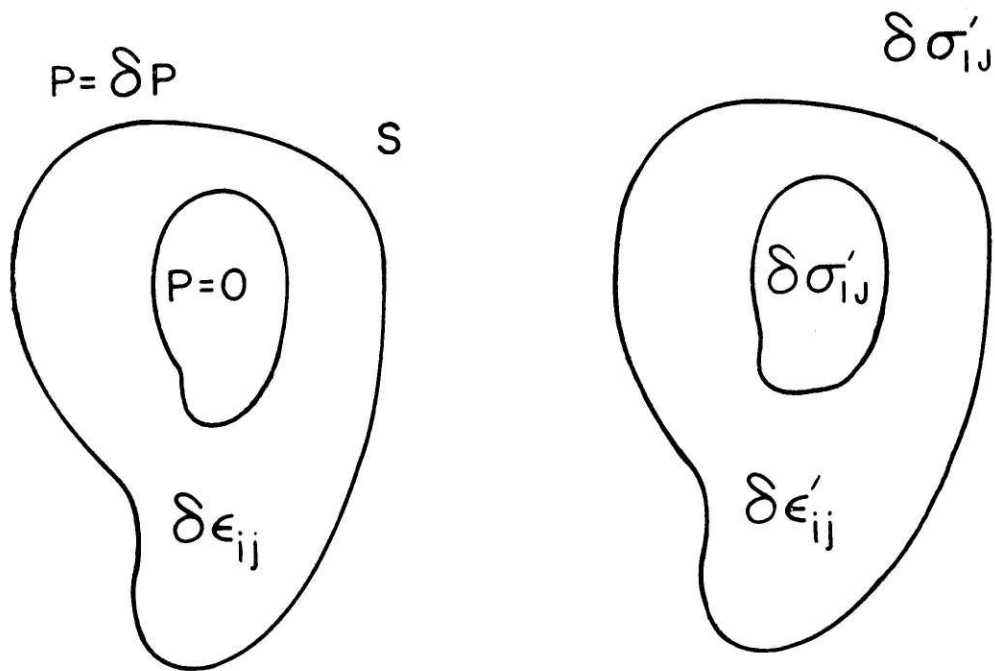
(no summation over I and J)

Figure 1.   Stress states for calculation of average matrix strain.

where the volume integral is over the matrix volume and the surface integral is over the outer surface S. $\delta\sigma_n$ and $\delta\varepsilon_n'$ are the normal stresses and strains on S. Since the stress in the unprimed case is hydrostatic,

$$\iint\limits_{S} \delta\sigma_n \delta\varepsilon_n' dS = -\delta P \Delta V' \tag{3}$$

where $\Delta V'$ is the volume change due to the displacement at the outer boundary of the solid under uniform stress $\delta\sigma_{IJ}'$. From simple elasticity theory,

$$\Delta V' = V\delta\sigma_{IJ}'(S_{11IJ} + S_{22IJ} + S_{33IJ}) \tag{4}$$

where S_{iiIJ} are components of the elastic compliance tensor. If the matrix is isotropic, (3) and (4) yield:

$$\iint \delta\sigma_n \delta\varepsilon_n' dS = -\delta P V \delta\sigma_{IJ}' \frac{1}{3}\beta_v^m \delta_{IJ} \tag{5}$$

where δ_{IJ} is the Kronecker delta. Since $\delta\sigma_{IJ}'$ is constant throughout the matrix volume, we can combine (2) and (5) to yield:

$$\delta\sigma_{IJ}'\iiint\limits_{matrix} \delta\varepsilon_{IJ} dV = -\delta P V \delta\sigma_{IJ}' \frac{1}{3}\beta_v^m \delta_{IJ} \tag{6}$$

or

$$\frac{1}{V}\iiint\limits_{matrix} \delta\varepsilon_{IJ} dV = -\delta P \frac{1}{3}\beta_v^m \delta_{IJ} \tag{7}$$

The left hand side of (7) is just the average matrix strain $\delta\varepsilon_{ij}^m$, so

$$\delta\varepsilon_{ij}^m = -\delta P \frac{1}{3}\beta_v^m \delta_{ij} \tag{8}$$

From (1),

$$d\varepsilon_{ij}/dP = d\varepsilon_{ij}^m/dP + d\eta_{ij}/dP \tag{9}$$

or

$$\beta_{ij} = \frac{1}{3}\beta_v^m \delta_{ij} - d\eta_{ij}/dP \tag{10}$$

since

$$\beta_{ij} = -d\varepsilon_{ij}/dP \tag{11}$$

If a component of strain due to the cracks that close at some pressure P_c increases linearly from $P = 0$ to $P = P_c$ (linear crack closure), we can express $\eta_{ij}(P)$ in terms of the distribution function $\nu_{ij}(P_c)dP_c$:

$$\eta_{ij}(P) = \int_P^\infty (1 - \frac{P}{P_c}) \nu_{ij}(P_c) dP_c \tag{12}$$

This expression merely sums up the contributions due to all cracks that remain partially open at pressure P. We can differentiate (12) with respect to P to obtain:

$$d\eta_{ij}/dP = -\nu_{ij}(P) - \int_P^\infty \frac{1}{P_c}\nu_{ij}(P_c)dP_c + P \cdot \frac{1}{P}\nu_{ij}(P) \tag{13}$$

$$= -\int_P^\infty \frac{1}{P_c}\nu_{ij}(P_c)dP_c \tag{14}$$

From (10)

$$\beta_{ij} = \frac{1}{3}\beta_v^m \delta_{ij} + \int_P^\infty \frac{1}{P_c}\nu_{ij}(P_c)dP_c \tag{15}$$

Differentiating (15) again:

$$d\beta_{ij}/dP = -\frac{1}{P}\nu_{ij}(P) \tag{16}$$

$$\nu_{ij}(P) = -P(d\beta_{ij}/dP) \tag{17}$$

or, in terms of strain:

$$\nu_{ij}(P) = P(d^2\varepsilon_{ij}/dP^2) \tag{18}$$

From the definition of $\zeta_{ij}(P)$, we have

$$\zeta_{ij}(P) = \int_0^P \nu_{ij}(P_c)dP_c \tag{19}$$

$$= \int_0^P P_c(d^2\varepsilon_{ij}/dP_c^2)dP_c \tag{20}$$

Integration by parts yields:

$$\zeta_{ij}(P) = P(d\varepsilon_{ij}/dP) - \int_0^P (d\varepsilon_{ij}/dP_c)dP_c \tag{21}$$

$$= P(d\epsilon_{ij}/dP) - \epsilon_{ij}(P) \qquad (22)$$

ζ_{ij} has a simple geometric interpretation as the zero pressure intercept of the tangent to the strain curve (ϵ_{ij} vs. P) at pressure P, as shown in figure 2.

If all cracks in a sample are closed above some pressure P_{max}, then from the definitions of ζ and η,

$$\zeta_{ij}(P_{max}) = \eta_{ij}(0) \qquad (23)$$

If strain data are available to P_{max}, $\eta_{ij}(P)$ can be calculated. Equation (9) is integrated to yield:

$$\epsilon_{ij}(P) - \epsilon_{ij}(0) = \epsilon_{ij}^m(P) - \epsilon_{ij}^m(0) + \eta_{ij}(P) - \eta_{ij}(0) \qquad (24)$$

From (23), and since $\epsilon_{ij}(0) = \epsilon_{ij}^m(0) = 0$,

$$\eta_{ij}(P) = \epsilon_{ij}(P) + \zeta_{ij}(P_{max}) - \epsilon_{ij}^m(P) \qquad (25)$$

For an elastic matrix,

$$\epsilon_{ij}^m(P) = P\left.\left(\frac{d\epsilon_{ij}}{dP}\right)\right|_{P_{max}} \qquad (26)$$

thus,

$$\eta_{ij}(P) = \epsilon_{ij}(P) + \zeta_{ij}(P_{max}) - P\left.\left(\frac{d\epsilon_{ij}}{dP}\right)\right|_{P_{max}} \qquad (27)$$

The term $-\left.\dfrac{d\epsilon_{ij}}{dP}\right|_{P_{max}}$ is the 'intrinsic compressibility' of the sample ($\frac{1}{3}\beta_v^m$).

The graphical interpretation of this expression is shown in figure 3. $\eta_{ij}(P)$ is merely the difference at pressure P between the strain curve and the tangent to the curve at P_{max}.

Our actual data consist of differential strain, the difference between the strain in a sample and that of a fused silica reference exposed to the same pressure. If we assume that the com-

Figure 2. Interpretation of DSA data. 2a is the differential
strain ($\hat{e}(P)$, sample strain minus strain in the fused
silica reference sample) vs. pressure (P). Linear
strain is given in three directions, denoted by the
numbers next to the curves. The dashed line tangent
to the curve (3) at .35kb is the strain curve that
would have been obtained if all of the cracks that
have closed by .35kb were not present in the sample.
Thus, $\zeta(.35kb)$ is the zero pressure strain due to cracks
closing at $P \leq 0.35kb$ (or, in the volumetric
case, the crack porosity due to cracks closing
at $P \leq 0.35kb$). 2b is the curve of ζ
vs. closure pressure (P_C) derived from 2a. 2c is the
distribution function for P_C, which we term crack
spectrum. The close spacing of data points below 100
bars results in uncertainties in the strain data
causing large fluctuations in $d\zeta/dP_c$. In order to
ascertain whether peaks below 100 bars are real, it
is necessary to refer to the actual strain data (fig-
ure 2a). In this case, although the strain appears
linear to 50 bars, we calculate $d\zeta/dP_c \leq 0$ for
$P_c < 50$ bars. This negative spike is spurious and is
an artifact of the curve fitting technique that appears
when the data are very closely spaced. The sample is
a shocked granodiorite from the site of the Piledriver
nuclear test. (After Simmons et al., 1975.)

Piledriver 216

Piledriver 216

Piledriver 216
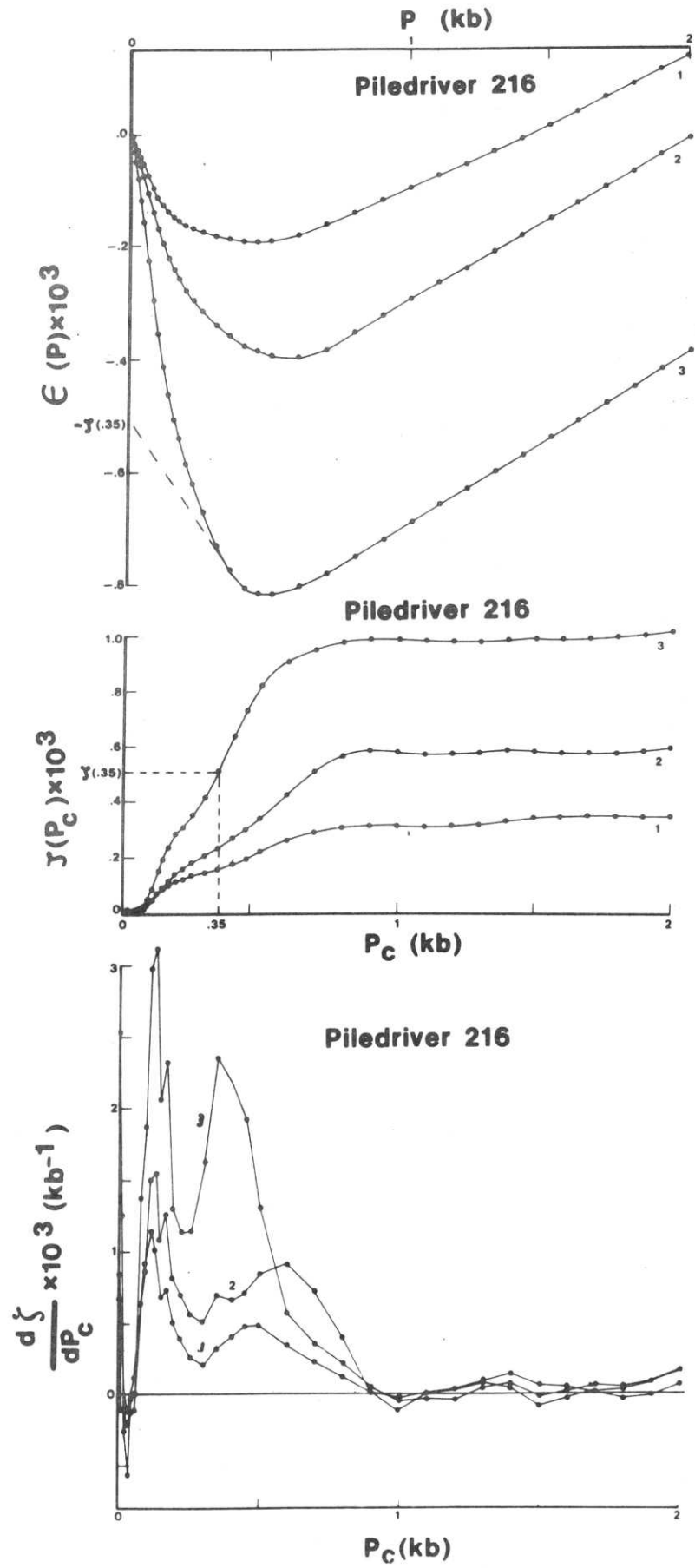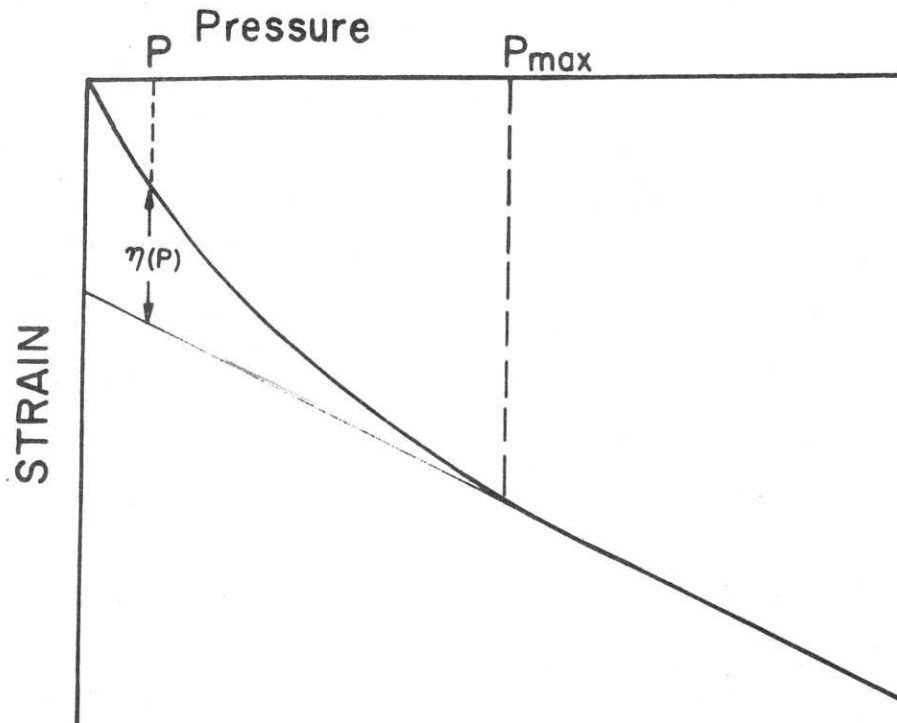
Figure 3. Determination of crack porosity vs. P. The strain due to cracks (η) at any pressure is the difference between the actual strain curve and that for a crack-free solid at that pressure.

pressibility of fused silica is linear for pressures below 2 kbar, we have

$$\hat{\varepsilon}_{ij} = \varepsilon_{ij} + \delta_{ij}\beta^{FS}P \tag{28}$$

where $\hat{\varepsilon}_{ij}$ is the differential strain tensor, and β^{FS} is the fused silica compressibility. If we write $\zeta_{ij}(P)$ in terms of $\hat{\varepsilon}_{ij}$, we have (from equation (22))

$$\zeta_{ij}(P) = P\frac{d}{dP}(\hat{\varepsilon}_{ij} - \delta_{ij}\beta^{FS}P) - \hat{\varepsilon}_{ij} + \delta_{ij}\beta^{FS}P \tag{29}$$

$$= P\frac{d\hat{\varepsilon}_{ij}}{dP} - \hat{\varepsilon}_{ij} \tag{30}$$

which is in the same form as (22) with $\hat{\varepsilon}_{ij}$ substituted for ε_{ij}. Therefore, the calculations of ζ_{ij} and ν_{ij} can be done directly from the differential strain measurements, if the fused silica strain is linear with pressure. In our previous work (Simmons et al., 1974; Simmons et al., 1975), we assumed linearity; however, in the present work, we have corrected for the fused silica compressibility pressure dependence using the data of Peselnick et al. (1967). Their measurements show that the linear compressibility of fused silica varies from .913 x 10^{-6} bar^{-1} at P = 0 to .945 x 10^{-6} bar^{-1} at 2 kbar. The actual sample strain is calculated by adding to the differential strain the fused silica strain calculated from Peselnick's data. Then, in order to expand the strain scale on plots, and to facilitate comparison with previous differential strain data, a linear strain curve with a slope equal to the zero pressure fused silica compressibility determined by Peselnick et al. is subtracted from the actual strain curve. Thus, the differential strains plotted in this paper can be con-

verted to true strain with the formula:

$$\varepsilon_{ij} = \hat{\varepsilon}_{ij} - \beta P \delta_{ij} \qquad (31)$$

where $\beta = .913 \times 10^{-6} \text{ bar}^{-1}$.

We can calculate as a function of pressure the principal axes and values of $\hat{\varepsilon}_{ij}$, ζ_{ij}, ν_{ij}, and η_{ij}. Plots of the orientation of the principal axes of ν_{ij}, and the corresponding principal values, are most valuable, as they allow one to estimate the orientations of cracks with different closure pressures. Two examples of such a calculation are given in the RESULTS section of this paper. Volumetric parameters are merely scalar invariants of the corresponding tensors, for example

$$\zeta_v = \zeta_{11} + \zeta_{22} + \zeta_{33}. \qquad (32)$$

INTERPRETATION OF DSA DATA

At the present stage of development of the DSA technique, we are able to obtain the following parameters from a complete set of data:

1. The complete linear compressibility tensor as a function of pressure.

2. The total crack porosity as a function of pressure.

3. The crack porosity due to each individual set of cracks, as a function of pressure.

4. The distribution of crack closure pressures.

5. Orientation information for cracks of different closure pressures.

6. Contribution of each set of cracks to ζ, ζ_v, β, β_v as a function of pressure.

Even partial sets of DSA are useful, however. Strains measured in three orthogonal directions yield the following:

1. The total crack porosity as a function of pressure.

2. The crack porosity due to individual sets of cracks as a function of pressure.

3. The volumetric distribution of crack closure pressures.

4. The presence or absence of strongly oriented cracks.

Strain measured in a single direction yields values of crack closure pressures, even though the strain due to these cracks is known in only one direction.

Figure 2 illustrates the way in which DSA data are inter-

preted for a set of three orthogonal strain measurements.
The sample is a shocked granodiorite from the Piledriver site.
If $\hat{\varepsilon}$, ζ, and ν were tensor components or volumetric quantities,
the method of interpretation would be identical. Figure 2a
shows the way in which ζ is determined from $\hat{\varepsilon}$ vs. P. (see
equation (22)). Figure 2b is a plot of ζ vs. P_c, and figure 2c
is a plot of $\nu = d\zeta/dP$ vs. P_c.

The calculation of $\nu(P)$ requires two differentiations of
the $\hat{\varepsilon}$ vs. P. data. $\zeta(P)$ is calculated from $d\hat{\varepsilon}/dP$, and then dif-
ferentiated to yield $\nu(P)$. Our present method for calculating
derivatives involves fitting a quadratic through each point and
the n adjacent points on each side of it. (We use n = 2 when
the data spacing is >50 bars; n = 3 when the spacing is 50 bars
or less.) The derivative of the quadratic at the particular
pressure is then taken as the derivative of the function.
The derivative at the n lowest pressure points is taken from
the quadratic used to fit the (n+1)[th] point. Due to the large
variations in $\zeta(P)$ caused by small changes in $(d\varepsilon/dP)$, the
derivatives at the n highest pressure points are calculated from
a straight line fit through the last (2n - 1) points. Compara-
tively large scatter in $\zeta(P)$ and $\nu(P)$ still results near the
ends of the data set.

In order to illustrate the resolution of the DSA technique
and our data analysis methods, synthetic data were generated
which represented a crack distribution with a total crack porosity

of .05% closing at one kbar. Random strain errors in the range $\pm$ 5 x 10^{-6} (an upper limit for the scatter that we observe in $\hat{\epsilon}$) were superimposed upon these exact 'data'. Figure 4 shows the results of analysis of both the exact and randomized data. The delta-function crack distribution is smoothed into a peak with a width of 300 bars at half-maximum amplitude. The scatter in the data is not enough to impair resolution in this case; however, end effects are very apparent at the high closure pressures.

If the strain tensor is being calculated, the strain measurements in six or more directions at each pressure are inverted using a least-squares matrix inversion technique (Mendenhall, 1968; Nye, 1957) to yield the six independent components of the differential strain tensor, $\hat{\epsilon}_{ij}$. Each component of ζ_{ij} and ν_{ij} is then calculated as shown in Figure 2. The principal values and axes of $\hat{\epsilon}_{ij}$, ζ_{ij}, and ν_{ij} are then calculated at each pressure using the iterative method described by Nye (1957).
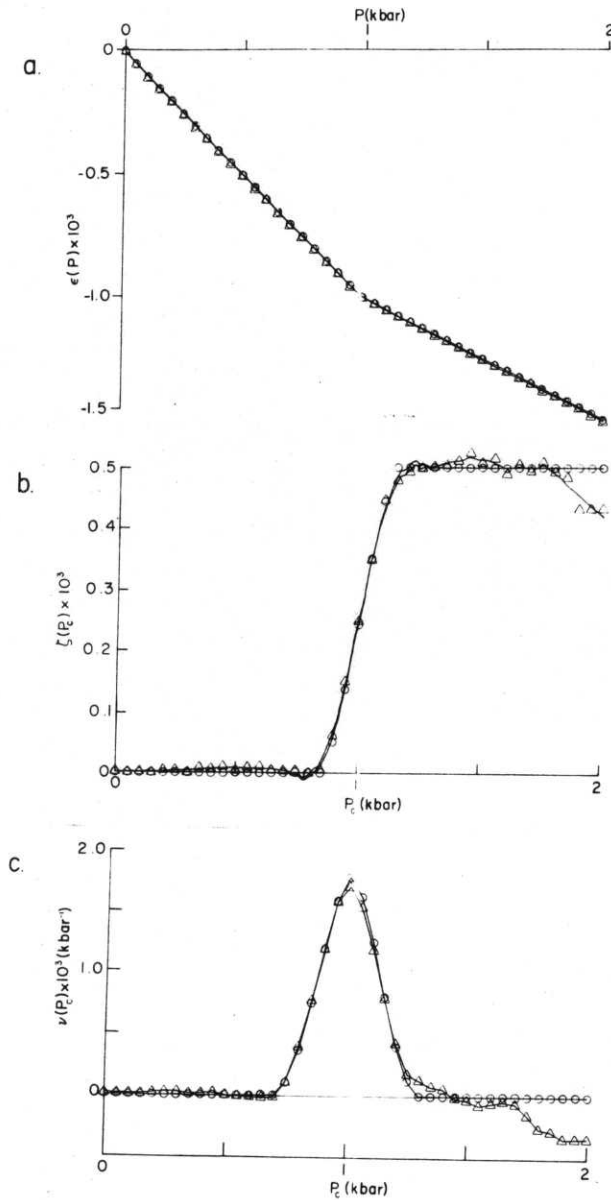
Figure 4. DSA analysis of synthetic data. Figure 4a shows $\varepsilon(P)$ for synthetic strain data generated to represent a population of .05% crack porosity closing at one kilobar. The circles represent the exact data, and the triangles represent data with random variations in the range $\pm 5 \times 10^{-6}$ superimposed. Figures 4b and c show $\zeta(P_c)$ and $\nu(P_c)$ for both sets of synthetic data.

SOURCES OF ERROR IN DSA

The sources of error in the DSA technique can be divided into two categories - errors in the measurement of the strain tensor, and systematic errors resulting from inapplicability of the models used to interpret the results. Errors due to temperature fluctuations, random instrumental variations, and inaccuracy of pressure measurement fall into the first category. These errors are minimized by the differential technique using a fused silica reference sample. From the degree of scatter observed in the data, we estimate that we achieve a precision as high as 2×10^{-6} in strain.

The most significant potential source of systematic error for a DSA measurement in a single direction is non-linear crack behaviour. Our work up to this time has primarily been done on low porosity igneous rocks, where we have often observed portions of strain curves that are linear over ranges of several hundred bars. Thus, we conclude that non-linear effects are of minor importance in the very flat cracks in igneous rock that close at the relatively low pressures of 2 kbar or less.

Sources of error in the determination of the strain tensor are individual variations in gauges, sample inhomogeneity, anisotropy in the rock matrix, and errors in the measurement of the orientations of strain gauges. Elastic anisotropy of the rock matrix is indistinguishable from an anisotropic distribution of cracks closing above the maximum pressure at which strain

data were obtained. DSA parameters are thus unaffected by matrix anisotropy. By using data from more than six gauges, the effect of the remaining sources of error above can be estimated. Following the method described by Mendenhall (1968, chapter 7), the probable error in each of the components of $\hat{e}_{ij}$ is calculated from measurements on up to twelve strain gauges.

RESULTS

Various parameters obtained from the DSA data for Westerly (RI) granite and Twin Sisters (WA) dunite are recorded in Table 1. Linear parameters are given in the three directions (x_1, x_2, x_3) used as the reference axes in subsequent tensor calculations. Westerly granite (MIT 1134) is a quartz monzonite similar to USGS sample G-2 described by Chayes (1967). Twin Sisters dunite is a massive, coarse grained (1 to 5 mm) dunite with some shear features.

Figure 5 displays the results of strain tensor calculations on a sample of Westerly granite. Figure 5a is a plot of each component of the differential strain tensor ($\hat{\varepsilon}_{ij}$) as a function of pressure, relative to the axes (x_1, x_2, x_3), shown in figure 5c. Note that the off-diagonal components of the differential strain tensor are equal to those of the actual strain tensor. The error bars in figure 5a represent the probable error in the tensor components estimated from the nine strain gauges used to calculate the six independent components. Figure 5b is a plot of the three principal values of $\hat{\varepsilon}_{ij}$ as a function of hydrostatic pressure. In figure 5c, the orientations of the principal axes are plotted on an equal area projection. Unfortunately, we have not developed an effective system for displaying the pressure to which each point corresponds on such a plot. The points bunched together on figure 5c near the x_1, x_2, and x_3 axes correspond to pressures below 500 bars. At higher

Table 1.

DSA Parameters

ζ_{ii}(2kb) x 10^6[±25]			β_{ii}(2kb)(Mb^{-1})[±.010]		
11	22	33	11	22	33
Westerly granite					
275	215	165	.667	.717	.699
Twin Sisters dunite					
0	0	370	.352	.357	.393

Figure 5. Differential strain of Westerly granite vs. P. Figure 5a
shows the components of the differential strain tensor,
$\hat{\varepsilon}_{ij}(P)$. Error bars are shown only for $\hat{\varepsilon}_{11}$. The
errors in the other five components are similar.
Figures 5b and c show the principal values
and principal axes of $\hat{\varepsilon}_{ij}(P)$. (In this and subsequent
projections, points are plotted on the lower hemisphere,
and x_3 is out of the paper.)

a.

b.

c.
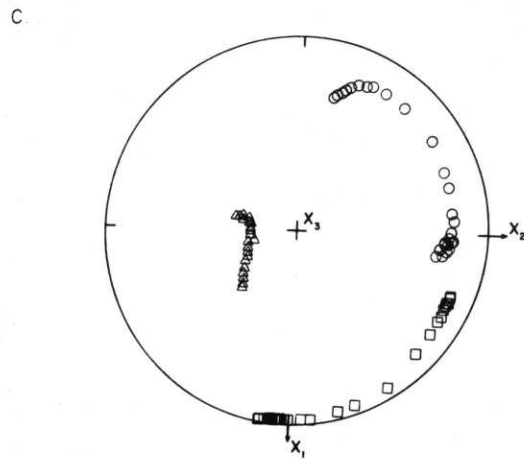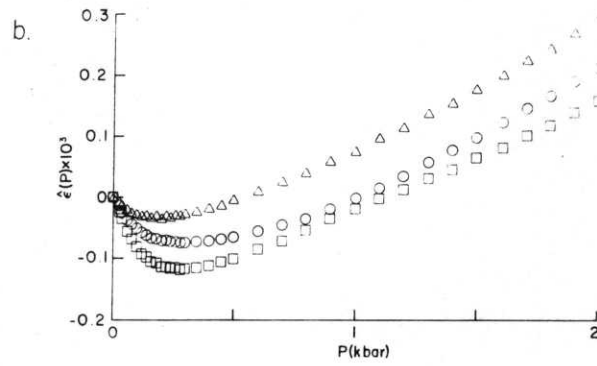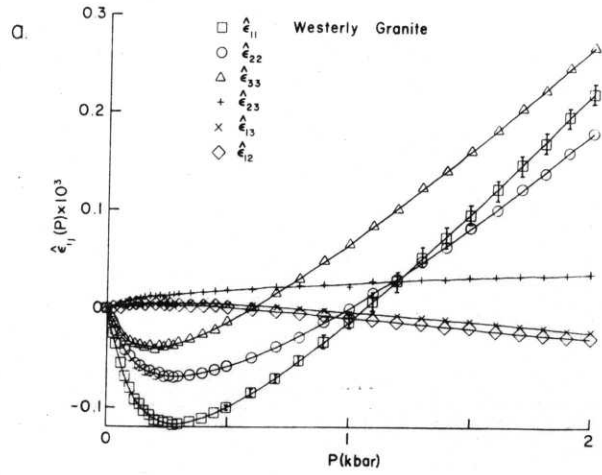
pressures, the orientations of the greatest and intermediate

principal strains rotate roughly counterclockwise around x_3,

while the axis of least principal strain moves toward x_1 with

increasing pressure. The interpretation of the variations

in orientation of the principal strain axes is fairly straight-

forward. At pressures below 500 bars, most of the strain is

due to crack closure, and the principal strain axes reflect

the principal axes of the crack distribution which are apparently

fairly constant. Above 500 bars, where the strain curves

are more linear, the strain is due mainly to mineral deformation

or deformation of pores closing at pressures higher than 2 kbar,

and the principal strain axes begin to reflect this high pressure

anisotropy.

Figures 6a, b, and c show the tensor $\zeta_{ij}(P_c)$ (the zero

pressure strain tensor due to cracks closing at $P \leq P_c$) in the

same way in which figures 5a, b, and c illustrate $\hat{\epsilon}_{ij}(P)$. The

principal axes of $\zeta_{ij}(P_c)$ are fairly constant in orientation for

all P_c less than 2 kbar, as expected since $\zeta_{ij}(P)$ reflects the

strain due to cracks closing at $P \leq 2$ kbar, independent of

mineral strains or strains due to cracks that close above 2 kbar.

There is no evidence of variation of crack orientation with

closure pressure in $\zeta_{ij}(P_c)$ of the Westerly granite.

Figures 7a, b, and c illustrate the tensor $\nu_{ij}(P_c)$ obtained

by differentiating $\zeta_{ij}(P_c)$. As $\nu_{ij}(P_c)dP_c$ is the zero pressure

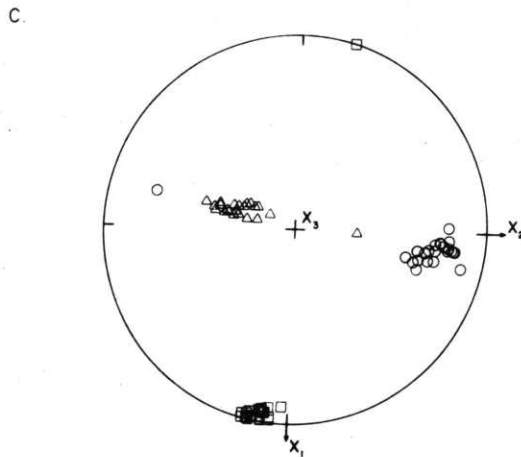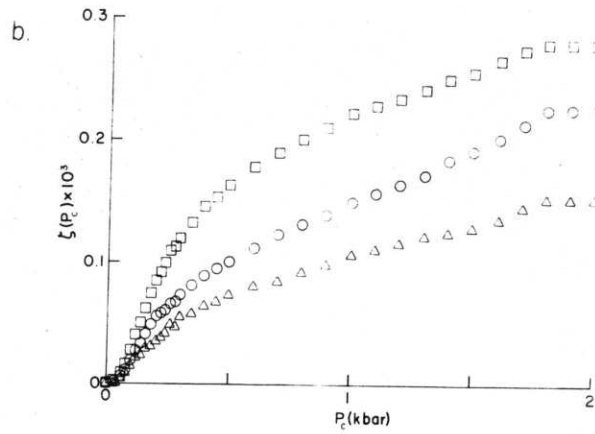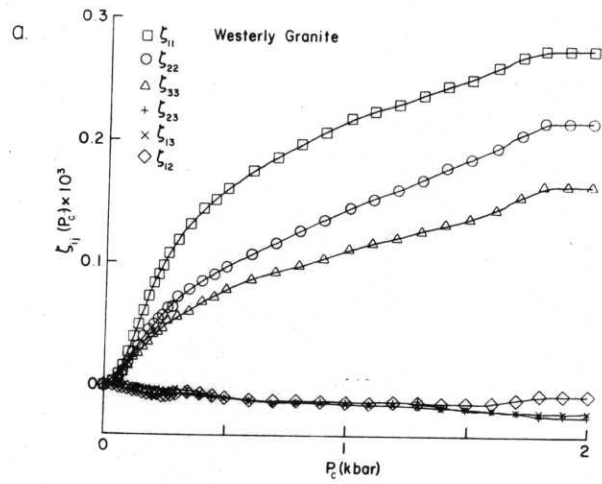strain tensor due to cracks that close between P_c and $P_c + dP_c$,

Figure 6. ζ_{ij} vs. P_c for Westerly granite. Figure 6a shows the components of $\zeta_{ij}(P_c)$. Figures 6b and c show the principal values and axes of $\zeta_{ij}(P_c)$.
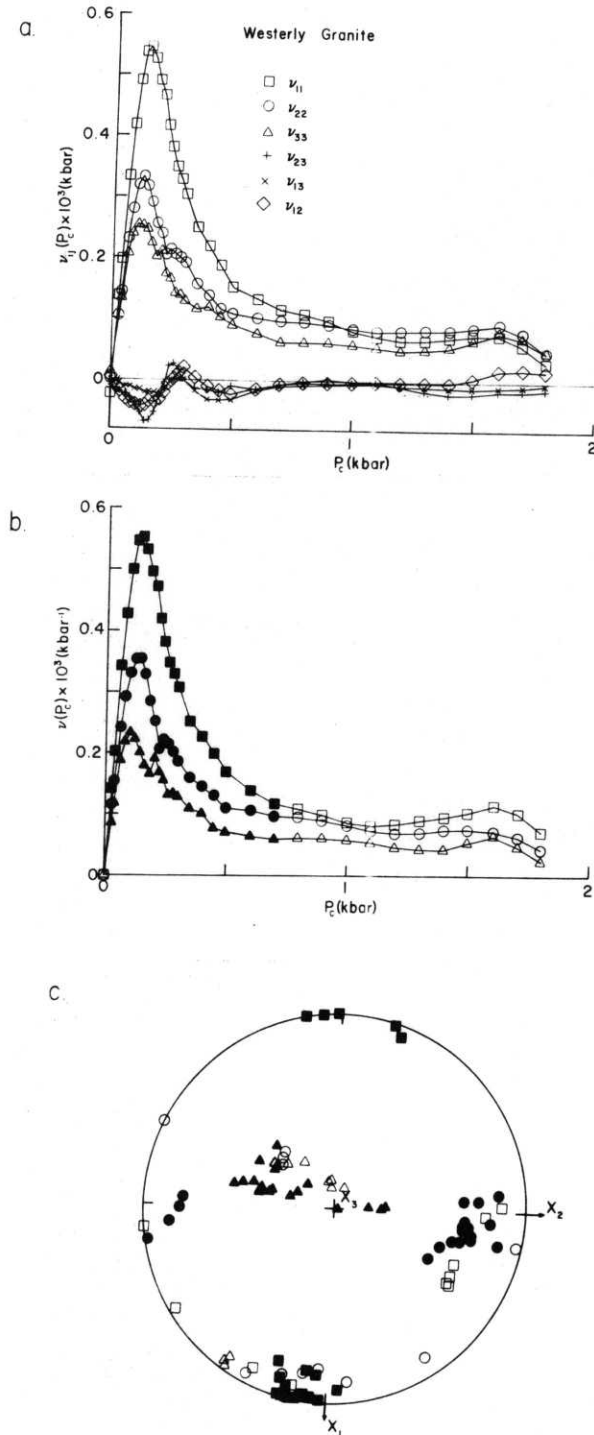
Figure 7. ν_{ij} vs. P_c for Westerly granite. Figure 7a shows the components of $\nu_{ij}(P_c)$. Figures 7b and c show the principal values and axes of $\nu_{ij}(P_c)$.

examination of $\nu_{ij}(P_c)$ affords the best opportunity to characterize the orientations of cracks closing at various pressures. The principal axis orientations shown in figure 7c have somewhat more scatter than those shown in figures 5c and 6c, due to the scatter in ν_{ij} induced by the two differentiations of $\hat{\epsilon}_{ij}$ which are necessary to calculate ν_{ij}. In addition, the principal values of $\nu_{ij}(P_c)$ are very nearly equal for values of P_c greater than 800 bars, causing the orientations of the principal axes to be poorly constrained. The principal axes of $\nu_{ij}(P_c)$ for $P_c \leq 700$ bars are fairly well defined, as shown by the solid points on figures 7b and 7c. The principal axes of ν_{ij} show no correlation with pressure for $P_c \leq 700$ bars, indicating that the cracks that contribute most to the crack porosity of this sample have similar orientation distributions, despite their variation in closure pressures, which range from near zero to about 800 bars. A more isotropically oriented set of cracks closing at pressures up to 2 kbar appears to be present, as $\nu_{ij}(P_c)$ remains distinctly positive over the entire pressure range. An indication of the importance of cracks closing at pressures higher than the maximum (in this case, 2 kbar) can be obtained by comparing the linear compressibilities observed on the sample at high pressures with those calculated for a crack-free aggregate of the same composition. The mineral composition of our sample of Westerly granite (MIT 1134) is given in table 2. Feves and Simmons (1976) compare the

Table 2.

Modes of Westerly Granite and Component Bulk Moduli

Mineral	MIT 1134	K(Mbar)
Quartz	22.5	.381
K-feldspar	30.7	.542
Plagioclase (An 17)	39.2	.595
Biotite	5.0	.487
Muscovite	0.7	.506
Opaques	0.7	1.62
Secondary	0.4	
Others	0.8	
Total	100.0	
Number of points	1000	
Density	2.644 g/cc	

composition of MIT 1134 to other samples of Westerly granite.
The Voigt and Reuss bounds (Hill, 1952) on the bulk modulus (K)
were calculated for an isotropic aggregate having the composition
and component moduli listed in table 2, with the result that
$.510 \leq K \leq .531$. The linear compressibility (β_L) in any direction
for such an aggregate is $(3K)^{-1}$, so $.628 \leq \beta_L \leq .654$. The small
difference between the isotropic aggregate β_L and the β_{ii} (no
summation) in table 1 suggests that most cracks are closed by 2kb,
and the differences among the β_{ii} are probably due to anisotropy
in the rock matrix.

The reference axes for the Westerly granite sample were
chosen in relation to the macroscopic fabric of our sample. In
quarrying terminology, the x_1-direction is normal to the rift
plane, the x_2-direction is normal to the grain plane, and the
x_3-direction is normal to the hardway plane. The data in figure
7a indicate that x_1 is near the direction of maximum zero pressure
crack strain, as anticipated if rift cracks are preferentially
oriented normal to x_1. The absence of any systematic change in
the principal directions of v_{ij} with pressure suggests that most
of the crack porosity in the sample was produced by the erosional
unloading that presumably caused the rift cracks (Jahns, 1943).

The differential strain tensor ($\hat{\varepsilon}_{ij}$) for the Twin Sisters
(WA) dunite is shown in figure 8. In this sample, essentially
all microcracks are oriented normal to the x_3-direction. The
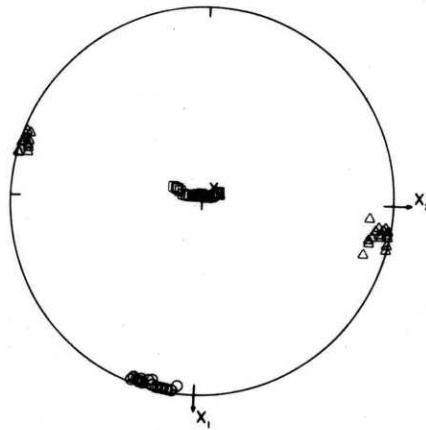intermediate and least principal strains are roughly aligned
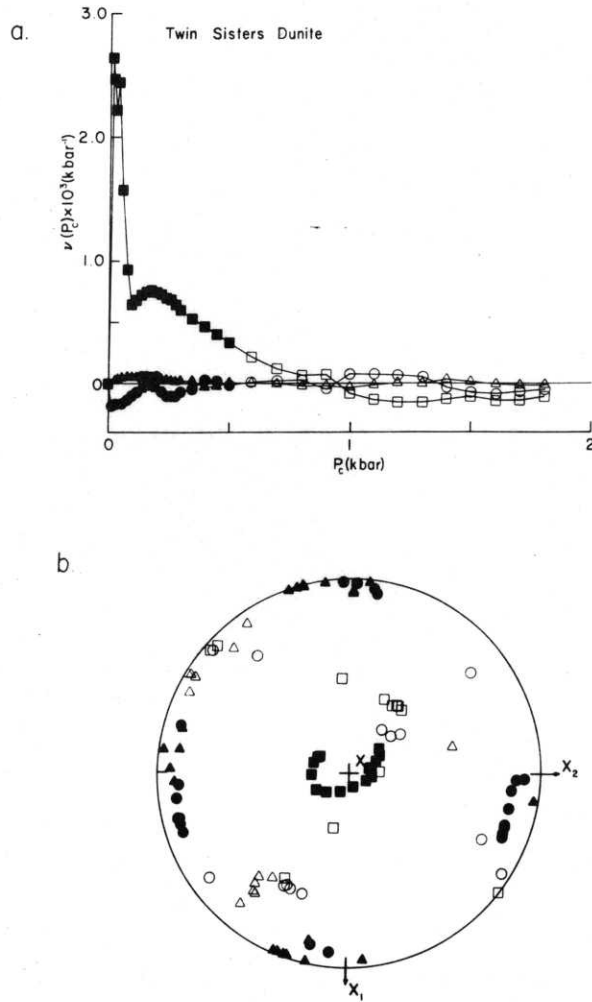
a. Twin Sisters Dunite
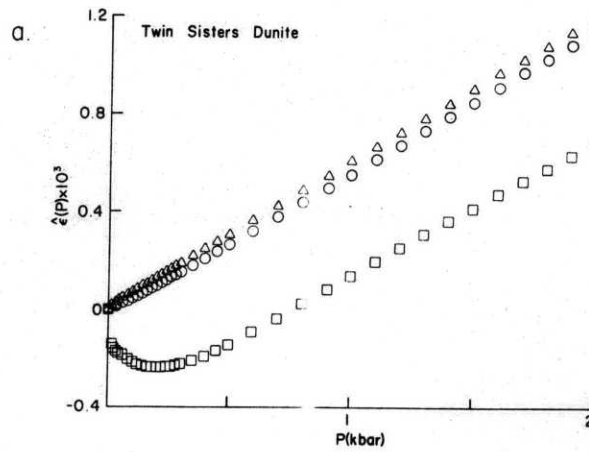
b.

Figure 8. $\hat{\varepsilon}_{ij}$ vs. P for Twin Sisters dunite. Figure 8a shows the principal values of $\hat{\varepsilon}_{ij}(P)$. Figure 8b shows the principal axes of $\hat{\varepsilon}_{ij}(P)$.

with x_1 and x_2, respectively, but are very close in value.

Figure 9 shows the crack distribution tensor (ν_{ij}) calculated from the strain tensor in figure 8. At pressures above ~500 bars, all cracks are closed, so that $\nu_{ij} \equiv 0$ and the principal axes of ν_{ij} are unconstrained. For $P_c \leq 500$ bars (shown by the filled-in points in figure 9), the cracks are oriented normal to x_3, as was determined from $\hat{\varepsilon}_{ij}$ in this case. The closure pressure distribution contains a very sharp spike for $P_c < 20$ bars superimposed upon a relatively smooth distribution to $P_c = 500$ bars.

Figure 9. ν_{ij} vs. P_c for Twin Sisters dunite. Figure 9a shows the principal values of $\nu_{ij}(P_c)$. Figure 9b shows the principal axes of $\nu_{ij}(P_c)$.

CONCLUSIONS

The DSA technique allows evaluation of important crack parameters. The porosity distribution of crack closure pressures is obtained, as well as the principal axes of the crack distribution at each closure pressure. In addition, the crack distribution and porosity as a function of pressure can be calculated. Detailed characterization of cracks as described in this paper should be useful for predicting in situ properties from laboratory data in cases where the in situ crack distribution might differ from that in laboratory samples.

ACKNOWLEDGEMENTS

REFERENCES

Adams, L.H. and E.D. Williamson, On the compressibility of minerals and rocks at high pressures, Franklin Inst. J., 195, 475-529, 1923.

Batzle, M.L. and G. Simmons, Microfractures in rocks from two geothermal areas, Earth Planet. Sci. Lett., 30, 71-93, 1976.

Birch, F., The velocity of compressional waves in rocks to 10 kilobars, part 1, J. Geophys. Res., 65, 1083-1102, 1960.

Birch, F., The velocity of compressional waves in rocks to 10 kilobars, part 2, J. Geophys. Res., 66, 2199-2224, 1961.

Brace, W.F., Some new measurements of linear compressibility of rocks, J. Geophys. Res., 70, 391-398, 1965.

Chayes, F., Modal composition of USGS reference sample G-2, Geochem. et Cosmochim. Acta, 31, 463-464, 1967.

Feves, M. and G. Simmons, Effects of stress on cracks in Westerly granite, Bull. Seism. Soc. Am., in press, 1976.

Hill, R., The elastic behaviour of a crystalline aggregate, Proc. Phys. Soc. London (A), 65, 349-354, 1952.

Jahns, R.H., Sheet structure in granites: its origin and use as a measure of glacial erosion in New England, J. Geol., 60, 71-98, 1943.

Love, A.E.H., A Treatise on the Mathematical Theory of Elasticity, Cambridge University Press, London, 643 pp., 1927.

Mendenhall, W., Introduction to Linear Models and the Design

and Analysis of Experiments, Duxbury Press, Belmont, Cali-
fornia, 465 pp., 1968.

Morlier, P., Description de l'etat de fissuration d'une roche
a partir d'essais non-destructifs simples, Rock Mech., 3,
125-138, 1971.

Nye, J.F., Physical Properties of Crystals, Oxford University
Press, London, 322 pp., 1957.

O'Connell, R.J. and B. Budiansky, Seismic velocities in dry and
saturated cracked solids, J. Geophys. Res., 79, 5412-5426,
1974.

Peselnick, L., R. Meister, and W.H. Wilson, Pressure derivatives
of elastic moduli of fused quartz to 10 kb, J. Phys. Chem.
Solids, 28, 635-639, 1967.

Richter, D., G. Simmons, and R. Siegfried, Microcracks, micro-
pores, and their petrologic interpretation for 72415 and
15418, Proc. Seventh Lunar Sci. Conf., in press, 1976.

Simmons, G., Velocity of compressional waves in various minerals
at pressures to 10 kilobars, J. Geophys. Res., 69, 1117-
1121, 1964a.

Simmons, G., Velocity of shear waves in rocks to 10 kilobars, 1,
J. Geophys. Res., 69, 1123-1130, 1964b.

Simmons, G. and D. Richter, Microcracks in rocks, in: The Physics
and Chemistry of Minerals and Rocks, edited by R.G.J. Strens,
Wiley-Interscience, New York, 105-137, 1976.

Simmons, G., R. Siegfried, and D. Richter, Characteristics of

microcracks in lunar samples, Proc. Sixth Lunar Sci. Conf.,
3, 3227-3254, 1975.

Simmons, G., R. Siegfried, and M. Feves, Differential strain
analysis: a new method for examining cracks in rocks,
J. Geophys. Res., 79, 4383-4385, 1974.

Thill, R.E., R.J. Willard, and T.R. Eur, Correlation of longi-
tudinal velocity variation with rock fabric, J. Geophys. Res.,
74, 4897-4909, 1969.

Walsh, J.B., The effect of cracks on the compressibility of rock,
J. Geophys. Res., 70, 381-389, 1965.

Chapter 3

Shock-Induced Microfractures in Six Terrestrial

Igneous Rocks Characterized with Differential

Strain Analysis

INTRODUCTION

Microfractures produced by the passage of a shock wave through a rock greatly affect its physical properties at pressures below a few kilobars (Simmons et al., 1975; Todd et al., 1973). To predict the type of fracturing that will result from a given shock event, or to interpret the existing crack distribution of a rock in terms of its shock history, the relation between the shock-induced crack distribution and various pre-shock parameters of the rock (e.g., grain size, mineralogy, and initial crack distribution) must be determined. Several authors (Short, 1966; Hörz, 1968, 1969; Richter et al., 1976) have described petrographically shock-induced fractures in lunar and terrestrial materials. In this paper, we use the differential strain analysis (DSA) technique described by Siegfried and Simmons (1977) to characterize the shock-induced microcracks in a suite of terrestrial rocks subjected to various conditions of shock loading.

We used six different rocks: the Frederick (MD) diabase, the Mellen (WI) gabbro, the Westerly (RI) granite, the Wausau (WI) granite, the Twin Sisters (WA) dunite, and the Laramie (WY) anorthosite. This suite of samples was selected to represent a range of mineralogy, grain size, and initial crack distribution common in terrestrial igneous rocks. Modal compositions of the Frederick diabase, the Mellen gabbro, the Westerly granite, and the Wausau (Prehn quarry) granite are given by Feves et al. (1976).

Richter and Simmons (1976) petrographically describe the Mellen gabbro and Wausau granite. The Laramie anorthosite is the rock described as anorthosite by Klugman (1966). The Twin Sisters dunite is described in general by Ross et al. (1954). The modal composition of our sample is as follows: olivine (Fo_{94}) - 98.45%, ore - 1.35%, serpentine - 0.19%. Pre-shock crack distribution parameters for the samples are shown in Table 1. Oriented cracks were present in the Wausau and Westerly granites, and in the Twin Sisters dunite; the crack distributions in the rest of the samples were isotropic. All cracks in the dunite were coplanar, and the granites each had a distinct direction normal to which cracks were preferentially oriented (the rift direction, in quarrying terminology).

Samples of all six rocks were subjected to a similar shock condition with an explosive driver-plate apparatus. In addition, four samples were subjected to a shock of slightly higher pressure and half the duration of that of the other series of tests. The plane of preferred crack orientation was normal to the direction of shock propagation for the dunite and parallel to the propagation direction for the granite samples. The samples were recovered and examined with DSA in order to identify the sample parameters that significantly affected the post-shock crack distribution.

Table 1.

Characterization of Pre-Shock Samples.

Sample	Rock Type	Location	$^i\zeta$(2kbar) [%]	^iP_m [bars]	^iP_o [bars]	$^i\Gamma$ [bars]	r [mm]	$^i\beta$(2kbar) [Mb^{-1}]
1243-V	diabase	Frederick (MD)	0.0000	--	--	--	.5	1.36
1132-V	quartz monzonite	Westerly (RI)	0.119 ± .004	120	420	510	.5	2.12
1331-V	gabbro	Mellen (WI)	0.007 ± .005	1300	1000	800	.5	1.35
178-V	dunite	Twin Sisters (WA)	0.037 ± .003	~0	150	130	3.0	1.10
1374-V	granite	Wausau (WI)	0.043 ± .011	250	530	710	2.0	2.06
734-V	anorthosite	Laramie (WY)	0.048 ± .011	1500	750	730	5.0	1.61

EXPERIMENTAL TECHNIQUES

The rock samples were shock loaded with an explosive flying plate accelerator of the 'mousetrap' type, illustrated in figure 1. A line wave generator is used to detonate simultaneously the high explosive (HE) along one edge of the driver plate. As the detonation front proceeds through the high explosive, the driver plate is accelerated by the expanding gases. The angle α in figure 1 is adjusted so that $\sin \alpha = V/v_{HE}$, where V is the flyer plate velocity, and v_{HE} is the velocity of the detonation front in the high explosive. This choice of α causes the driver plate to arrive everywhere on the target simultaneously, generating a plane shock wave in the sample assembly. In practice, the edges of the driver plate tend to lag behind the center, so that the shock wave approximates a plane only in the region near the center of the driver. For this reason, the edge dimension of the square driver plate used was three times the sample diameter. The apparatus used is shown schematically in figure 2. The driver assembly was constructed of plexiglass, with the exception of the polycarbonate driver plate. General Electric Lexan driver plates 0.64 and 0.32 cm thick were used, with Du Pont Detasheet high explosive 0.038 and 0.025 cm thick. Wooden supports held the driver assembly and the aluminum sample holder in the proper angular relationship. The wooden support assembly rested on top of a steel garbage can completely filled with water, from which the sample was recovered after the shot.
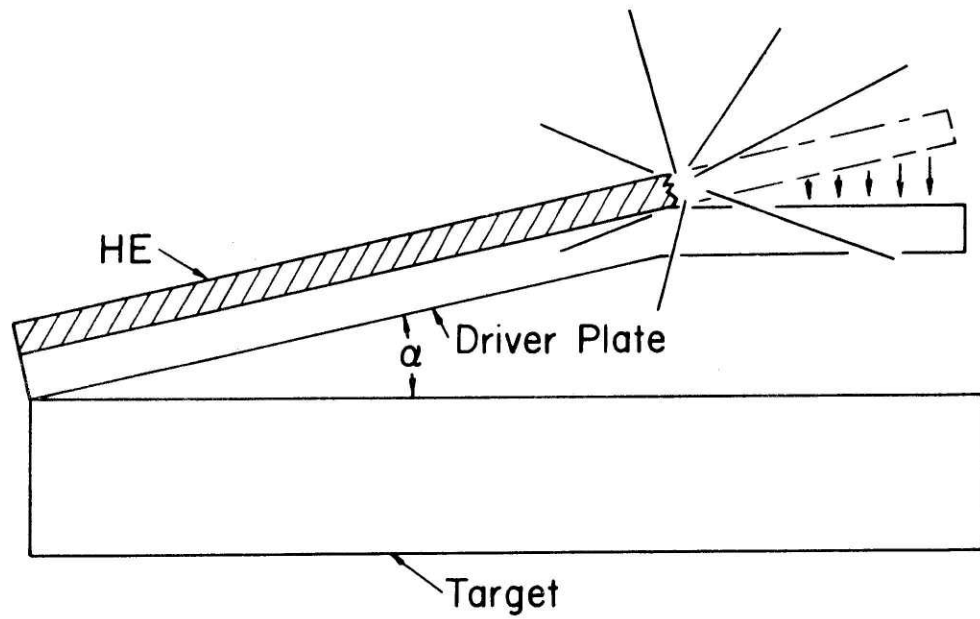
Figure 1. Schematic diagram of the flying plate apparatus. As the detonation front proceeds along the high explosive (HE), the driver is accelerated. The angle α is adjusted so that the driver arrives simultaneously at all points on the target.
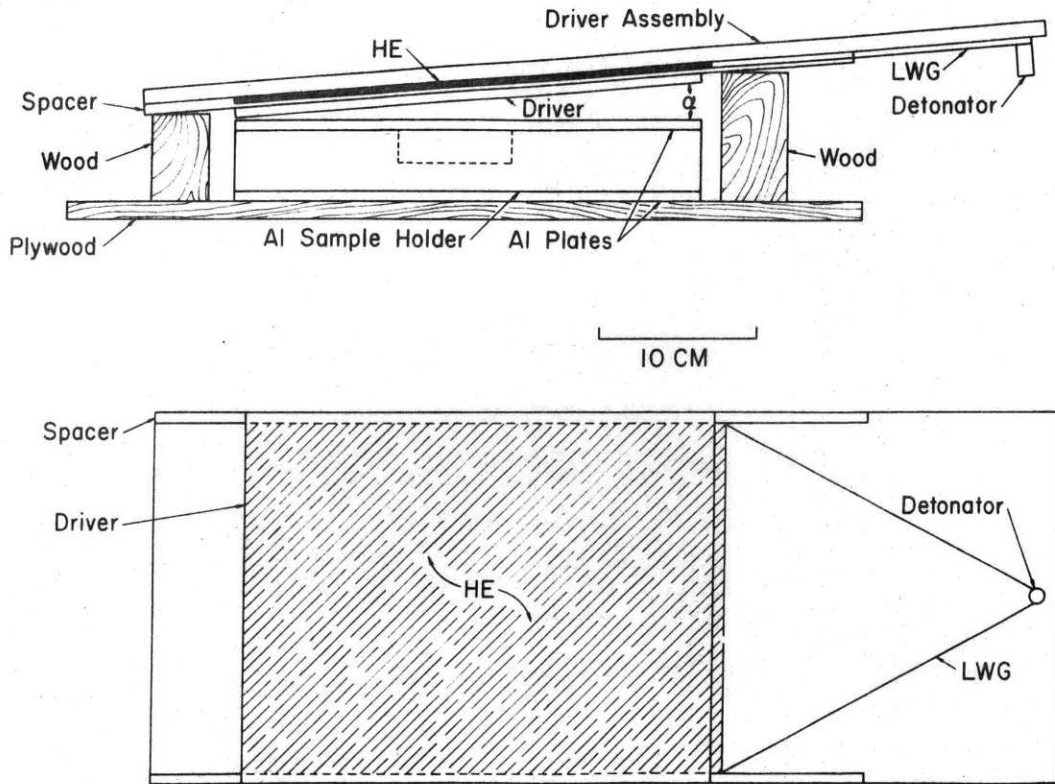
Figure 2.   Apparatus used in shock experiments. The upper
            diagram shows the relationship of the driver assembly
            to the sample holder assembly. The lower diagram
            is a view of the driver side of the driver assembly,
            showing the location of the high explosive (HE) and
            the Du Pont line wave generator (LWG).

In order to determine the proper angle α, several shots
were detonated with various combinations of explosive and
driver plate thickness. Their construction was similar to
that shown in figure 2; however, the sample assembly was
replaced by a target that allowed photographic determination
of the relative arrival time of the shock wave at various
points on the target, using the flash gap technique developed
by Walsh and Christian (1955).

The target used for the calibration shots is shown in
figure 3. When the shock wave propagates into the argon-filled
flash gap, the heated gas emits a flash of light that can be
recorded photographically. The light coming through the
slits shown in figure 3 is photographed with a rotating mirror
streak camera. The image is swept across the film with a
known velocity in the direction normal to the slits so that
if the shock wave arrives simultaneously at all points on
the target the slit images are straight lines perpendicular
to the direction of sweep. If the arrival is not simultaneous,
the velocity of the driver plate (and the appropriate correction
to α) can be determined from the angle between the slit images
and the direction of sweep.

In addition to determining the appropriate angle α to
use in the sample recovery shots, the series of calibration
shots allowed an estimate of the region over which the shock
wave was planar. In a typical shot, arrival was within 0.1 μs
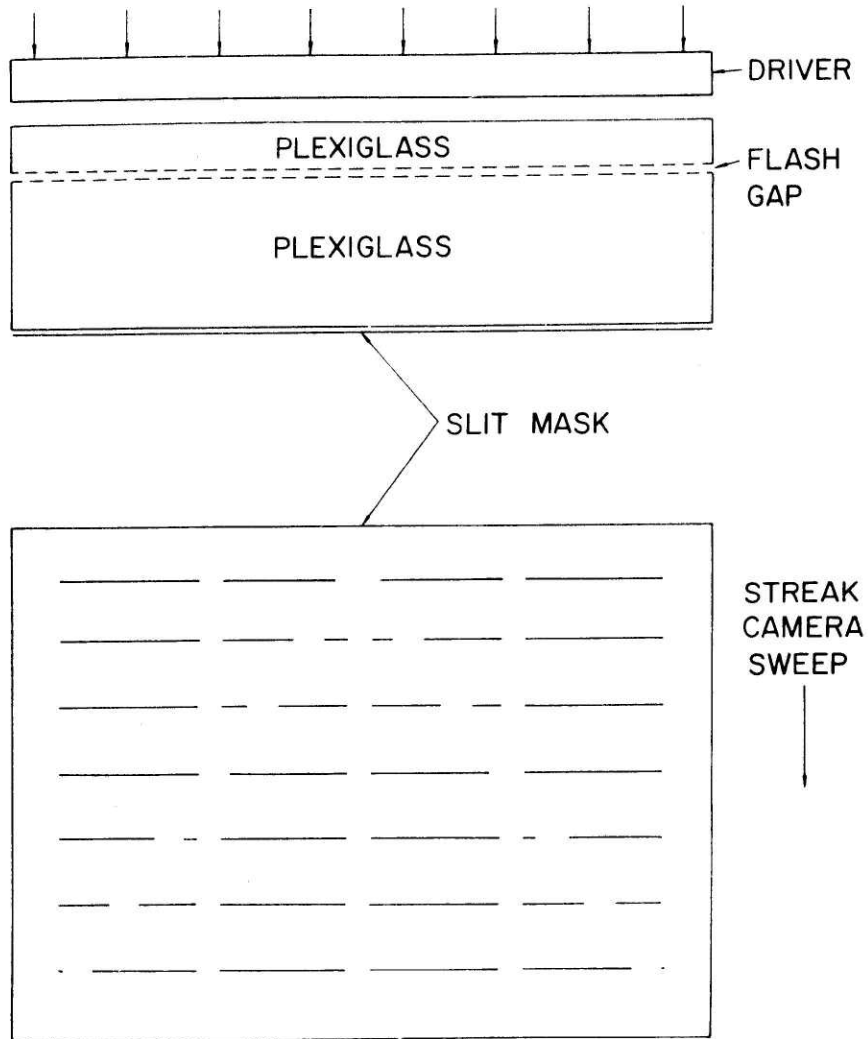
Figure 3. Target used in calibration experiments. When the driver arrives at a point on the target, the gas in the flash gap at that point luminesces, producing an image through the slit mask on the film in the streak camera.

over an area with dimensions roughly two thirds those of the driver plate.

The samples were discs 10.2 cm in diameter by 2 1/2 cm thick, cut with a diamond core drill. The parallel faces were surface ground parallel to within 0.005 cm. The samples were encased in a sample holder as shown in figure 4. A hole was machined into each sample holder, a 30 cm disc of 2024 aluminum, to fit each particular sample. Aluminum plates 0.63 cm thick were placed above and below the sample holder, as shown in figure 2, so that the polycarbonate driver impacted the top plate rather than the sample.

In the first trial recovery shot, the sample was badly broken by sets of radial and concentric fractures converging toward the center of the sample. These fractures were probably due to waves generated by the impedance mismatch at the interface between the diabase sample and the aluminum sample holder and propagated toward the center of the sample. To solve this problem, we minimized the coupling between these waves and the center portion of the sample. See figure 4. A 5.1 cm core was cut from the center of each 10.2 cm sample disc. The cylindrical surface of the 5.1 cm core was coated with silicone vacuum grease, and the 0.16 cm gap between the disc and the surrounding annulus caused by the kerf of the core drill was filled with epoxy and Al_2O_3 mixed in proper proportions to match the sample density. All of the shots reported in this paper
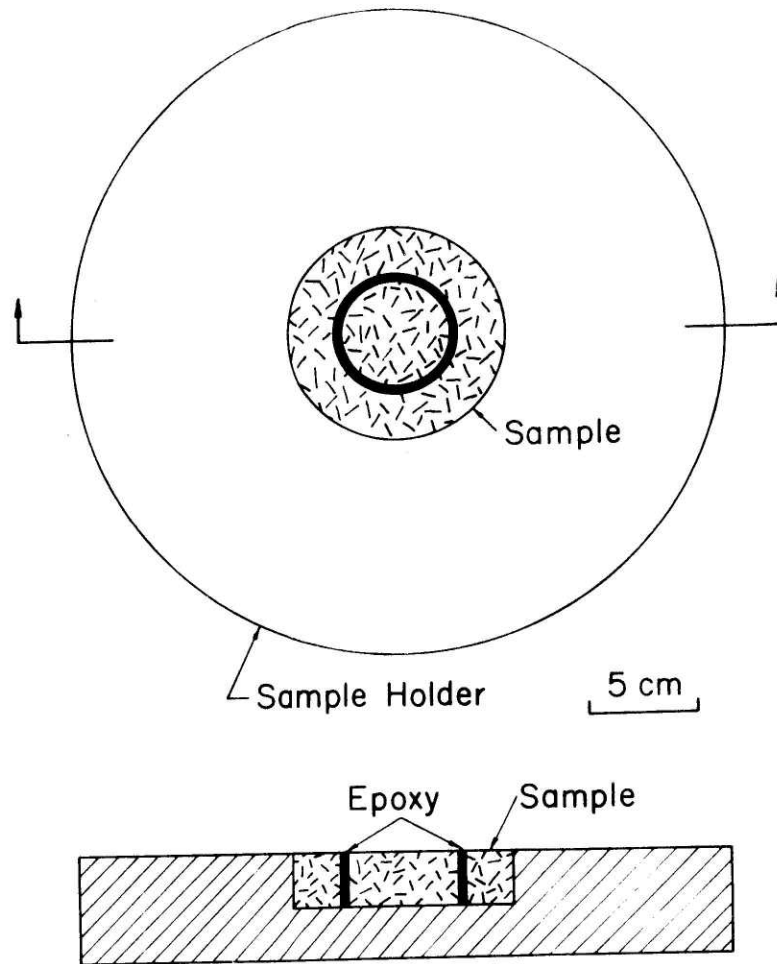
Figure 4. Sample holder. A hole was machined into the aluminum disc to fit each sample. The lower diagram is a cross section of the sample and holder.

were prepared with this central core, which seemed to solve the problem; the outer rock ring was often broken but the central disc remained physically intact.

The shock pressure in a target can be calculated from the driver plate velocity if the Hugoniot equations of state for both the driver and target materials are known. The calculation of shock pressure in a one-dimensional impact experiment has been described by several authors (Duvall and Fowles, 1963; Gault and Heitowit, 1963). The Rankine-Hugoniot equations, expressing conservation of mass, momentum, and energy across a steady shock front, form the basis for calculation of shock parameters:

$$\rho_0 U = \rho (U-u) \qquad (1)$$

$$P - P_0 = \rho_0 U u \qquad (2)$$

$$[(E - E_0) - \frac{u^2}{2}]\rho_0 U = P_0 u \qquad (3)$$

where U is the shock propagation velocity, u is the particle velocity due to the shock wave, P is pressure, ρ is density, and E is internal energy. The subscript zero refers to the initial state. If any two of the shock parameters U, u, ρ, P, or E are known, the above equations are sufficient to determine all others. Since pressure and particle velocity must be continuous across an interface, a convenient representation of the Hugoniot equation of state of a material is the locus

of points on a P-u diagram representing states connected by
a shock transition from the initial state.

In figure 5, we illustrate the calculation of u and P
for the transmitted and reflected waves due to a shock inci-
dent on an interface between two dissimilar materials. If
(u_1, P_1) is the state of material A behind the shock wave, the
reflected wave locus must also pass through (u_1, P_1). The
reflected wave locus is the mirror image of the incident wave
locus, reflected through (u_1, P_1). Since u and P must be
continuous across the interface, the state in both material A
and B behind the reflected and transmitted waves must be given
by the intersection (u_2, P_2) of the loci for the reflected wave
in A and the transmitted wave in B.

A similar graphical approach is used in the case of a
driver of material A impacting a target of material B. In
this case, the velocity of the driver (V) is the known quantity.
The reflected wave locus for the driver must pass through the
point (V,0), thus determining the state (u_2, P_2) of the target
after the passage of the transmitted wave.

Shots were detonated with three combinations of explosive
and driver plate thicknesses. The driver plate velocities,
shock durations, and calculated shock pressures in aluminim
that resulted from each of these combinations are shown in
Table 2. Hugoniot curves for polycarbonate, 2024 aluminum,
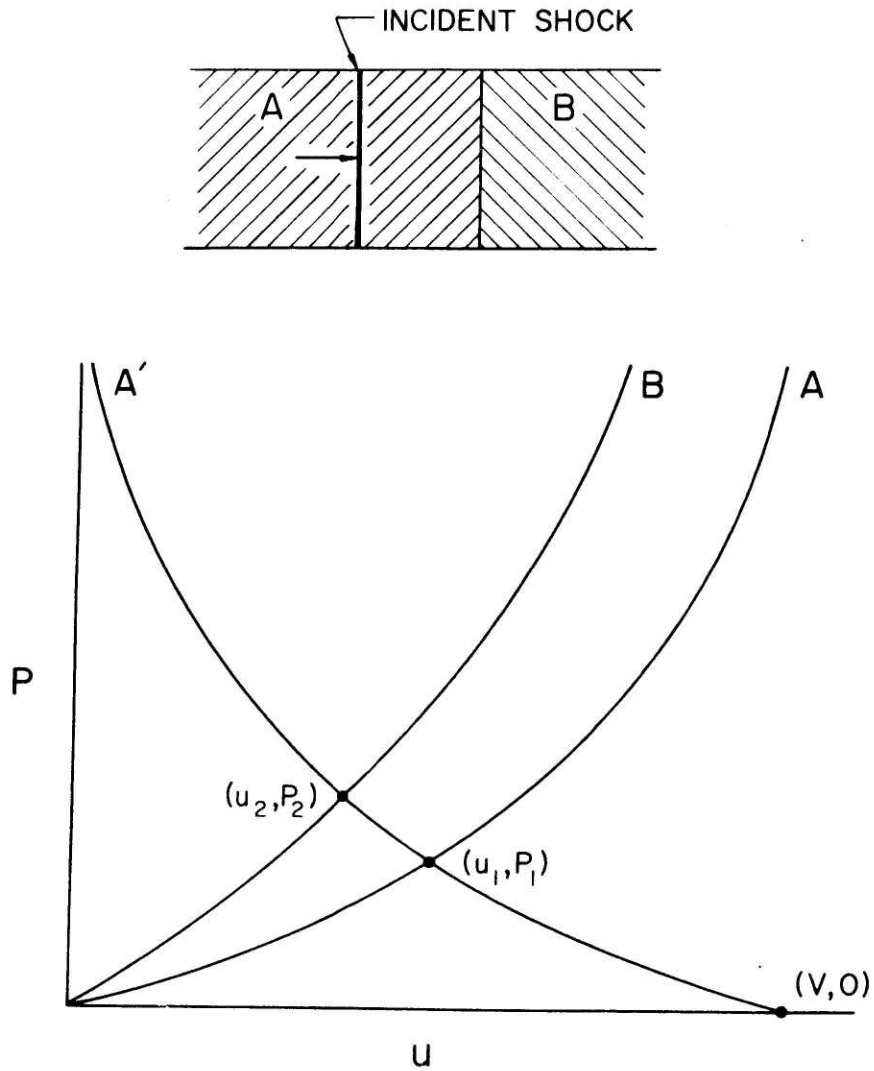and three of the rocks used for our shock recovery experiments

Figure 5.   Determination of shock pressures and particle
velocities for the reflection of a shock at an inter-
face.   The curve marked 'A' is the Hugoniot locus
for material A.   The curve marked 'A'' is the locus
for the reflected wave in material A.   The curve 'B'
is the Hugoniot locus for material B.

Table 2.

Shock Experiment Parameters.

	d(cm)	v(km/sec)	P(kbar)	t(μsec)
1	.32	.26	6.0	3.2
2	.64	.21	4.6	6.5
3	.32	.40	9.8	3.1

d: Driver thickness.

v: Driver velocity.

P: Pressure of transmitted shock in aluminum.

t: Shock duration.

are plotted in figure 6. The curves for Frederick diabase and Westerly granite are almost identical to that for aluminum, while the dunite curve differs somewhat over the pressure range of interest. The gabbro used in our experiments is mineralogically similar to the diabase, and probably has a similar Hugoniot curve. The curve for the anorthosite is probably very close to the granite and diabase curves, at least at the relatively low pressures shown in figure 6.

In all samples besides the dunite, the shock wave will be transmitted essentially without change from the aluminum cover plate into the sample. The determination of the shock pressure in aluminum for each of the three shot configurations is shown in figure 6. The resulting pressures are marked P_1, P_2, and P_3 in figure 6 and tabulated in Table 2. The shock pressure in the dunite can be determined once the state of the aluminum after shock passage is known, as shown in figure 6 by the pressure marked P_D. The shock pressure in the dunite is about 20% greater than that in the rest of the samples with the same driver velocity.

The duration of the shock pulse is controlled by the time required for the shock wave to travel to the driver-air interface and be reflected back as a pressure release wave. The pulse duration (t) for each shot configuration is listed in Table 2.
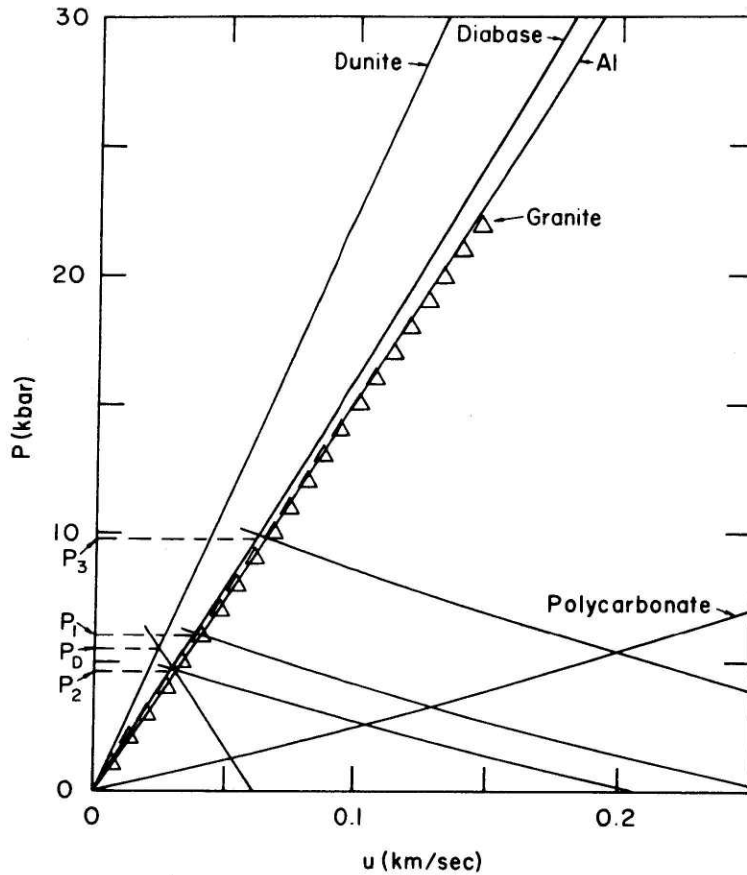
Figure 6. Hugoniot curves for the materials used in our shock
experiments. The curve for aluminum (2024) is
from McQueen et al. (1970). The diabase and dunite
curves are from McQueen et al. (1967). The data
for granite is from Brace and Jones (1971). The
polycarbonate curve is derived from unpublished
measurements of bulk sound velocity and high pres-
sure Hugoniot points by McQueen. Shock pressures
in aluminum for the various experimental configura-
tions are shown by P_1, P_2, and P_3. P_D is the pres-
sure in dunite for the one dunite shot.

DSA TECHNIQUES

The center disc of each shocked sample was cut into a rectangular block to be used for DSA measurements. The pre-shock DSA samples all came from within about 10 cm of the shocked samples, in the same rough blocks. Shocked and pre-shock samples were prepared similarly for DSA measurements, as described by Siegfried and Simmons (1977). Between 12 and 16 strain gauges were mounted on each sample.

The parameters determined from DSA measurements are $\beta(P)$, the compressibility as a function of pressure; $\zeta(P_c)$, the zero pressure strain due to cracks closing by P_c; and the distribution function $\nu(p_c)dP_c$, the zero pressure strain due to cracks closing between P_c and P_c+dP_c. In principle, data from six strain gauges are sufficient to determine the complete tensors for β, ζ, and ν; however, the crack distributions in the shocked samples were sufficiently inhomogeneous to preclude meaningful determination of tensor parameters. We use all of the available strain data to calculate the strain tensor for each sample, and then analyze the trace of the strain tensor, or volumetric strain. Redundant data from more than six strain gauges allows the error in each of the tensor components to be estimated from the deviations of their measured values about their predicted values (see Mendenhall, 1968, chapter 7). The estimated error in the volumetric strain due to sample inhomogeneity is calculated from the errors estimated for the diagonal com-

ponents of the strain tensor.

The pre-shock and post-shock crack distributions are
characterized by four parameters, which we now define. $\zeta(2\text{kbar})$
is the zero pressure porosity due to cracks closing by two
kilobars, the maximum pressure of our DSA measurements. $\zeta(2\text{kbar})$
is the total area under the distribution curve. Since the
cracks in most terrestrial igneous rocks are closed by two
kilobars, $\zeta(2\text{kbar})$ represents the total crack porosity for most
samples. The median crack closure pressure, P_0, is defined as
that pressure at which the zero pressure crack porosity due to
cracks closing below P_0 is one-half of the total crack porosity
($\zeta(P_0) = \zeta(2\text{kbar})/2$). The pressure P_m is defined as the pres-
sure at which $\nu(P_m)$ is a maximum. The width of a closure
pressure distribution is characterized by a parameter
$\Gamma = \zeta(2\text{kbar})/\nu(P_m)$. We identify pre-shock parameters with a
preceding superscript 'i', for example $^i\Gamma$, $^iP_0$.

RESULTS

The differential strain data and calculated crack closure
pressure distributions for virgin and shocked samples are
shown in figures 7 through 12. Table 3 lists the pressures
to which each sample was shocked, as well as various parameters
characterizing the resulting crack distributions. The errors
listed for ζ(2kbar) in Table 3 are estimated from the redun-
dant linear strain data used to calculate the volumetric
strain, and are due to inhomogeneity in the crack distributions.
The large uncertainties in porosity of the shocked samples makes
correlation difficult between most pre-shock parameters and
the amount of crack porosity. Fortunately, comparatively little
variation in the shape of crack closure pressure distributions
was observed among strain gauges mounted on any given sample. We
estimate that the parameters P_m, P_0, and Γ are accurate to
±20%.

The most outstanding feature of the data is the large dif-
ference in crack porosity between samples of the same rock that
have been exposed to shocks of similar pressure but different
duration. Without exception, the rocks that have experienced
the longer shock pulse have much higher crack porosity, even
though the shock pressure associated with the longer pulse
was slightly lower. Before a causal relationship is established
between the length of a shock pulse and the degree of micro-
fracturing in a rock, we must show that the fractures were actually

Figure 7. Volumetric DSA data for 1243 (Frederick diabase).

The virgin sample had zero crack porosity (within

the resolution of the DSA technique, ζ_v(2kbar) $\leq$ .002%.)

The curve for $\hat{\epsilon}$(P) is linear and $\nu(P_c)$ is uniformly

zero for 1243-V and are therefore not shown. The

crack spectrum for 1243-2 has a distinct peak at

160 bars and the cracks causing most of the porosity

are closed by 1 kbar. 1243-3 has a much broader

crack spectrum. The small peaks in the spectrum are

at the resolution limit of the technique and may

not be real. In any case, the small peak at 120 bars

is not nearly as prominent as the low closure pres-

sure peaks in the rest of the shocked samples. Note

the difference in scale between the two crack spectra.
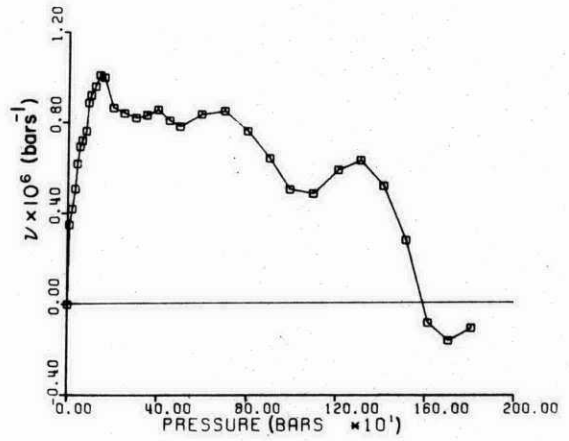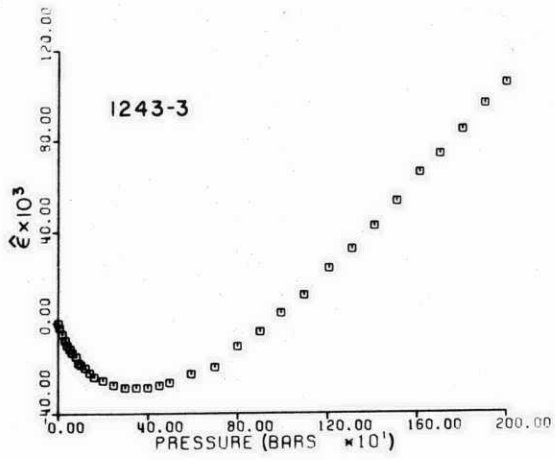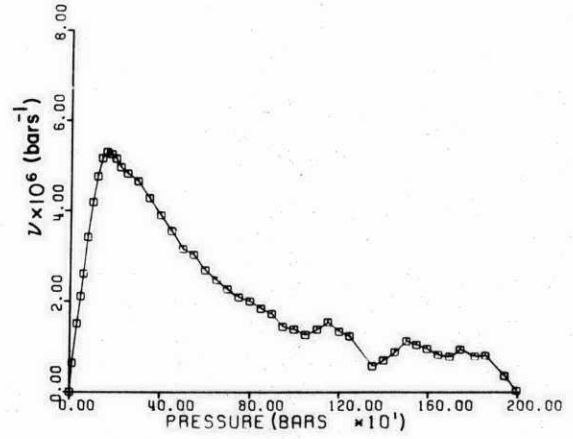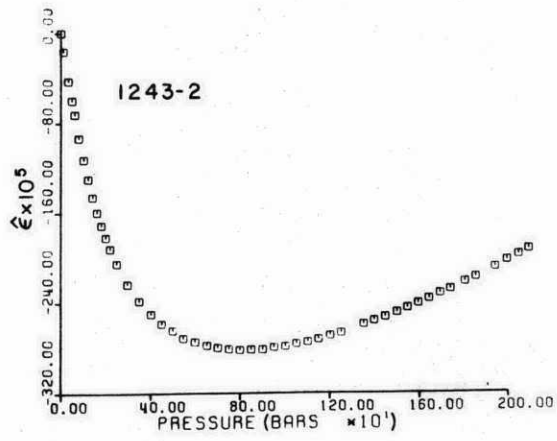
Figure 8. Volumetric DSA data for 1132 (Westerly granite). The crack spectra for the virgin and shocked samples are very similar in shape but not in magnitude (note the scale change). The fluctuations in $\nu(P_c)$ for $P_c > 1$ kbar is 1132-V are most likely due to scatter in the strain data and probably do not represent real peaks in the crack spectrum. In all three samples, the cracks responsible for most of the porosity are closed by 1 kbar. The most prominent features of the spectra are the peaks near 100 bars.
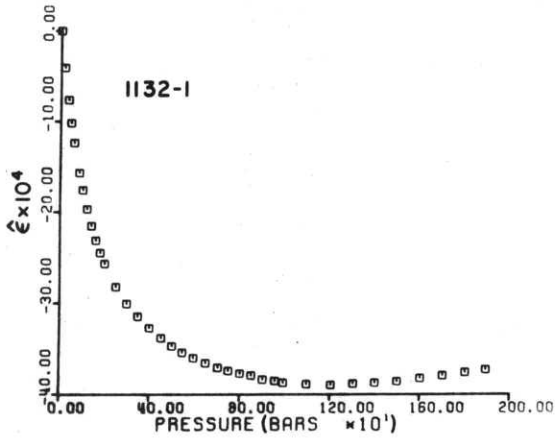
Six plots showing ε̂ (epsilon) and ν (nu) versus pressure for samples 1132-V, 1132-1, and 1132-2.
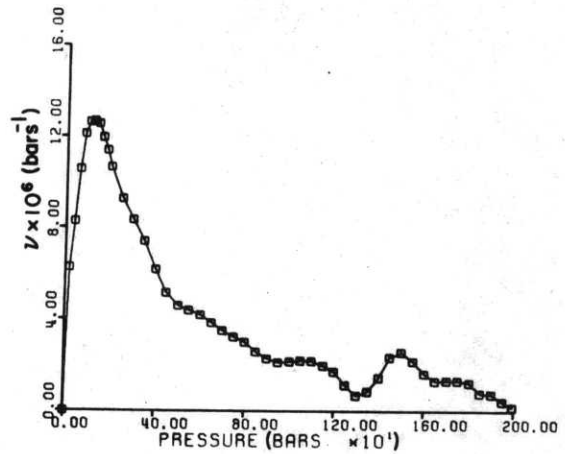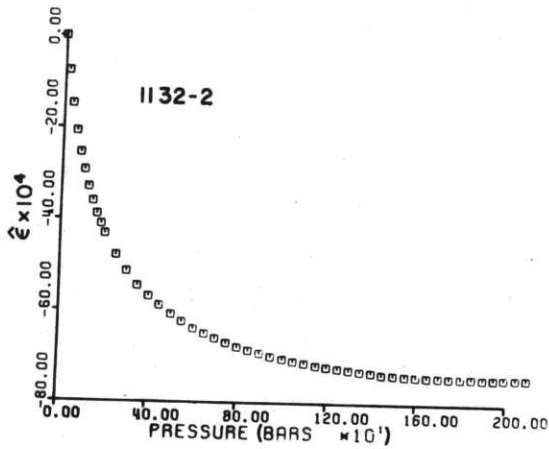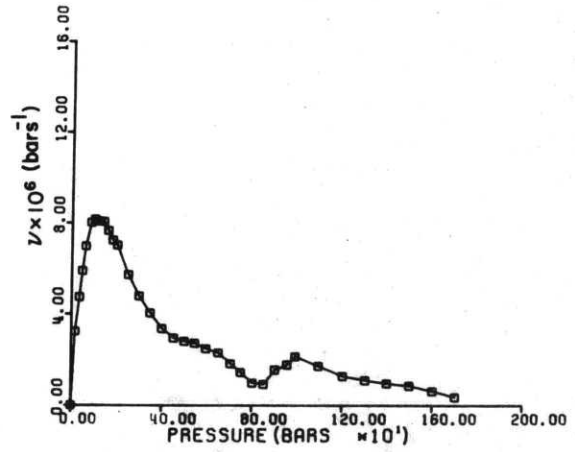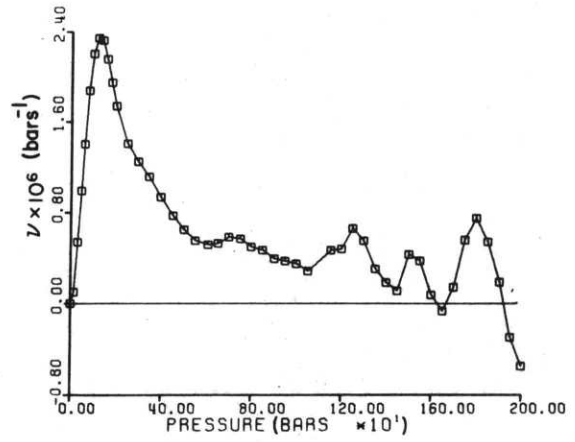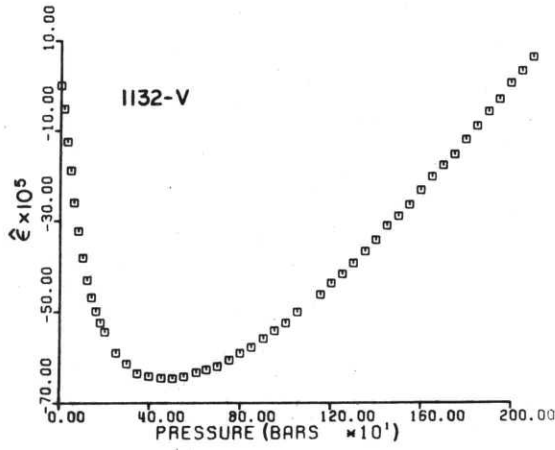
Figure 9. Volumetric DSA data for 1331 (Mellen gabbro). Resolu-
tion of the crack spectrum of the virgin sample is
very difficult because the porosity is very low,
ζ_V(2kbar) = 0.007%. The fluctuations in the crack
spectrum of 1331-V illustrate the way in which scatter
in strain data affects the $\nu(P_c)$ curves. Note the
scale difference between the crack spectrum of the
virgin sample and each of the shocked samples. Not-
withstanding the large scatter in $\nu(P_c)$ for 1331-V,
we see no evidence of a low closure pressure peak in
this sample. We have no useful strain data for 1331-1
over the pressure range from 1.2 to 1.8 kbar; however,
we do have enough data to calculate ζ(2kbar). Fortunately,
the cracks responsible for most of the porosity in 1331-1

are closed by 1 kbar. We have indicated with a
dashed line the crack spectrum for 1331-1 over the
range 1.2 - 1.8 kbars on the basis that $\nu(P_c)$ is
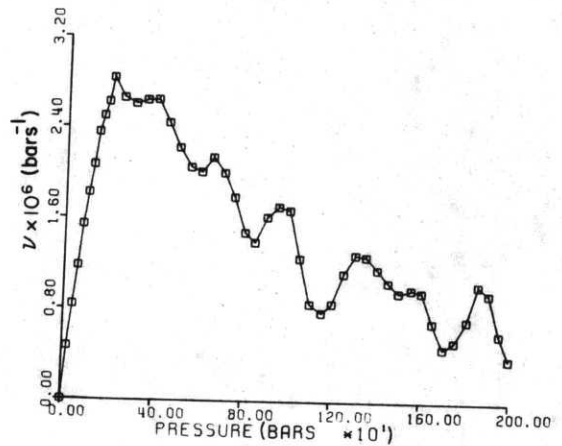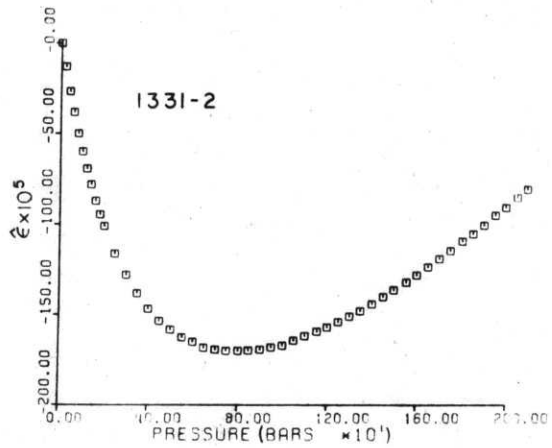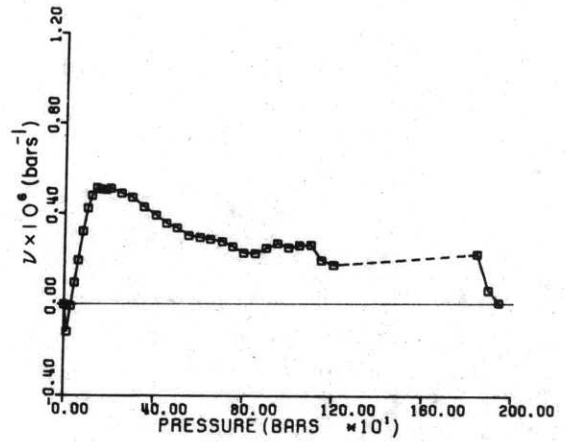evenly distributed over that range.
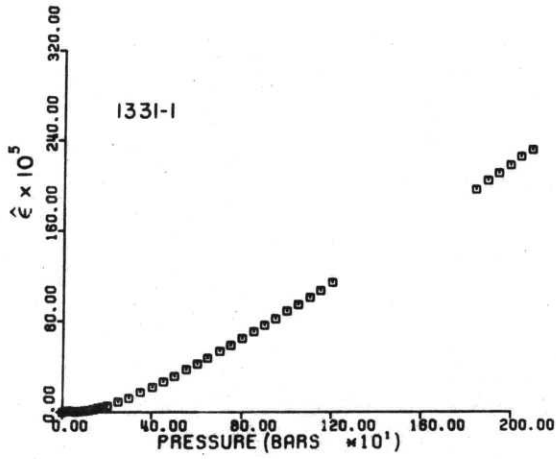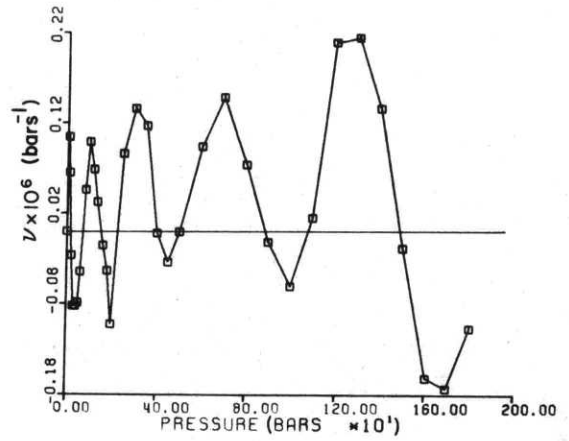
1331-V

1331-1

1331-2
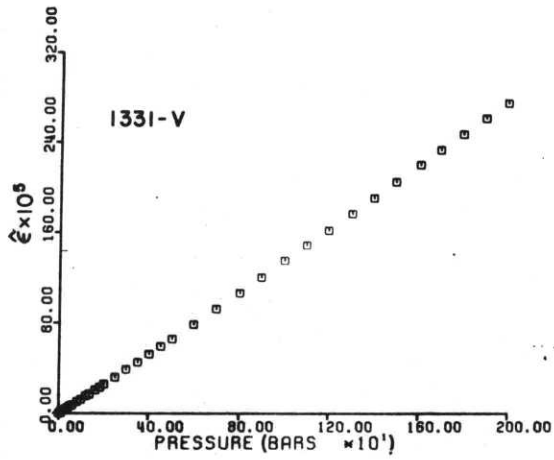
Figure 10. Volumetric DSA data for 1374 (Wausau granite). All
three spectra contain a low closure pressure peak;
however, the spectrum for 1374-2 is considerably
broader than the others. The cracks responsible
for most of the porosity are closed by a pressure of
1 kbar in all three samples. The peaks in the
spectra of 1374-V and 1374-1 at P_c > 1 kbar are
due primarily to scatter in the strain data. Note
the large differences in the scales of the spectra
among the three samples.
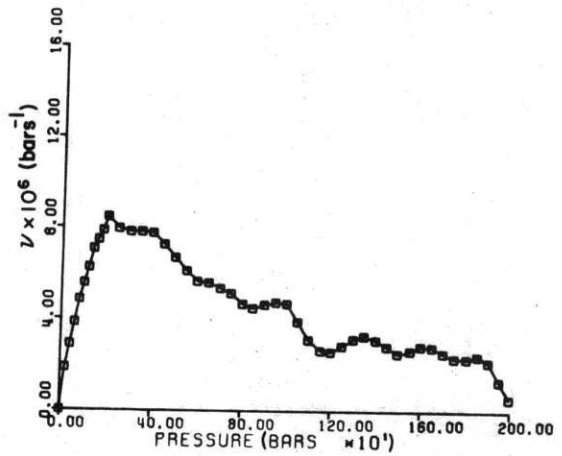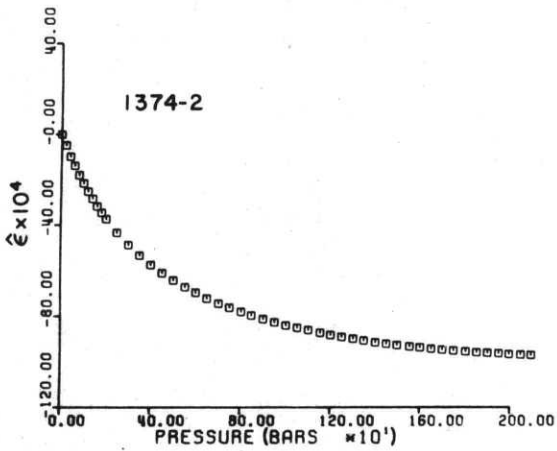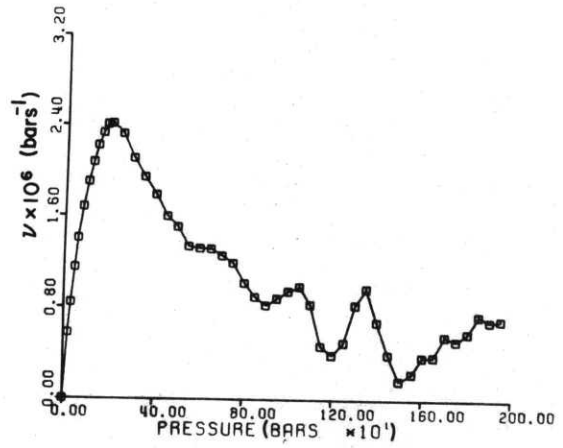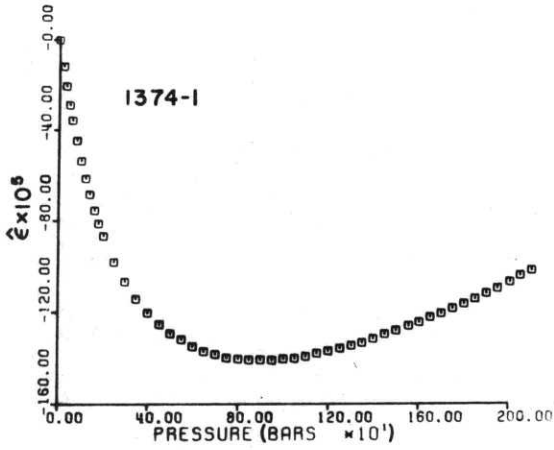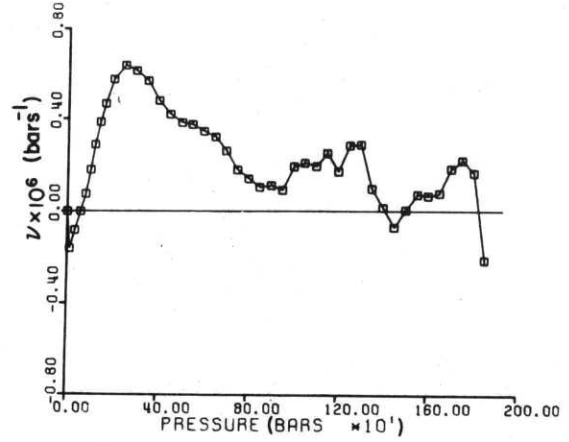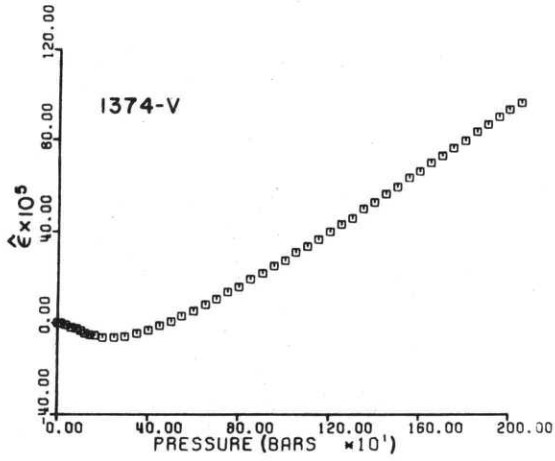
Figure 11. Volumetric DSA data for 178 (Twin Sisters dunite).
The virgin sample has significant porosity due to
cracks closing at P < 20 bars, producing a very
sharp low closure pressure spike in the crack spec-
trum.   There is no corresponding peak in the crack
spectrum of the shocked sample.   The difference in
scale between the two spectra is such that the peak
would not be apparent in the spectrum of 178-2
unless it had been greatly magnified.   Very little
of the porosity in either sample is due to cracks
closing at $P_c \geq 1$ kbar.
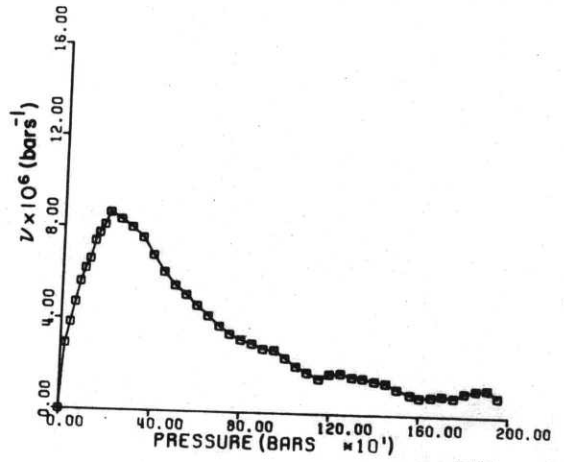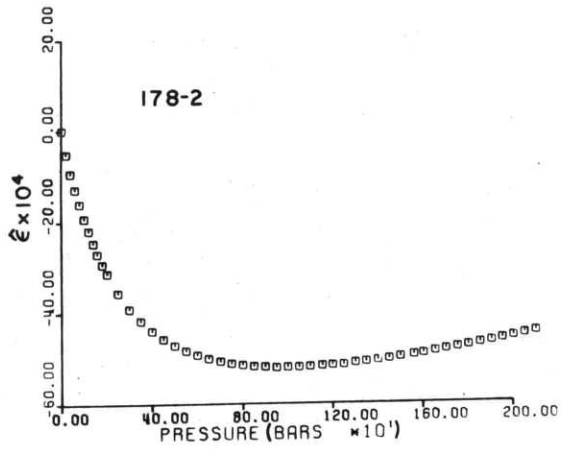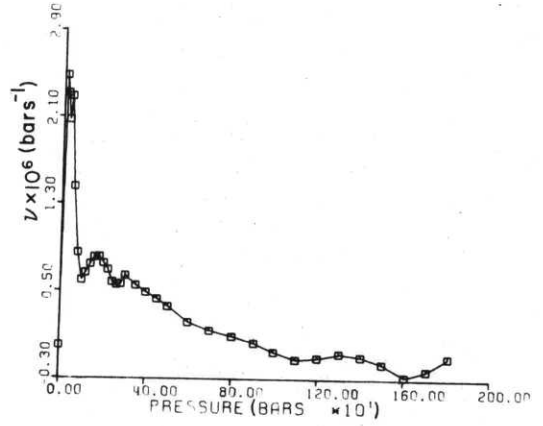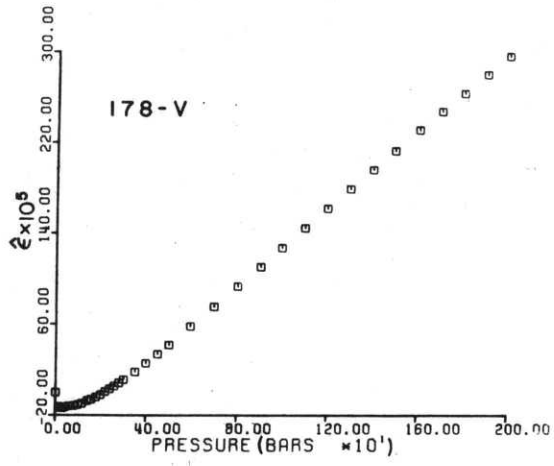
Figure 12. Volumetric DSA data for 734 (Laramie anorthosite).
The porosity of the virgin sample is fairly low,
and is not concentrated in a low closure pressure
peak. Most of the large fluctuation in $\nu(P_c)$ is
probably due to scatter in the strain data, since
in general there seem to be no corresponding discon-
tinuities in $\hat{\epsilon}(P)$. There is, however, a distinct
discontinuity in $\hat{\epsilon}(P)$ at 1.5 kbar, corresponding to
the largest peak in the spectrum. We conclude that
this peak is real, although the data does not allow
much to be said about its shape and true size. The
spectrum of the shocked sample does have a prominent
low closure pressure peak. The peak at 1500 bars is
also present in 734-2 and is increased greatly in
magnitude (note the scale change in the spectra).

734-V

734-2
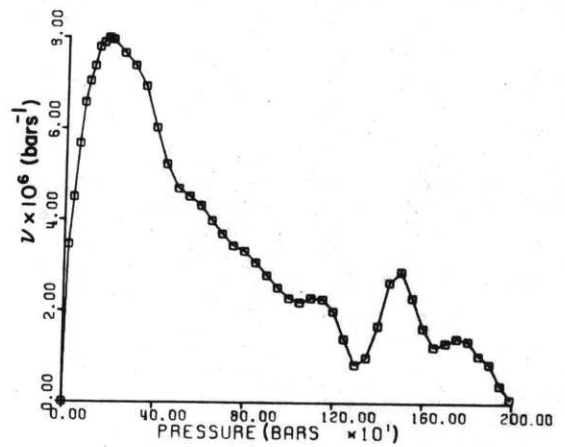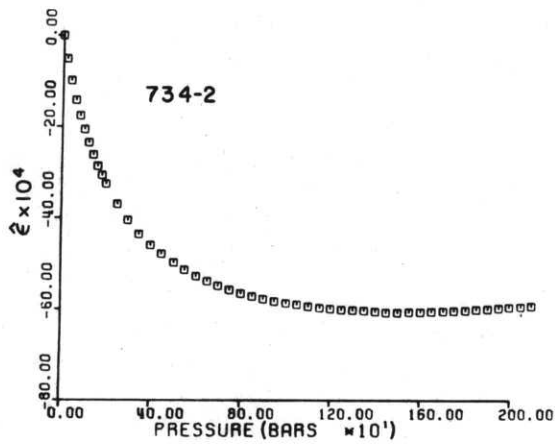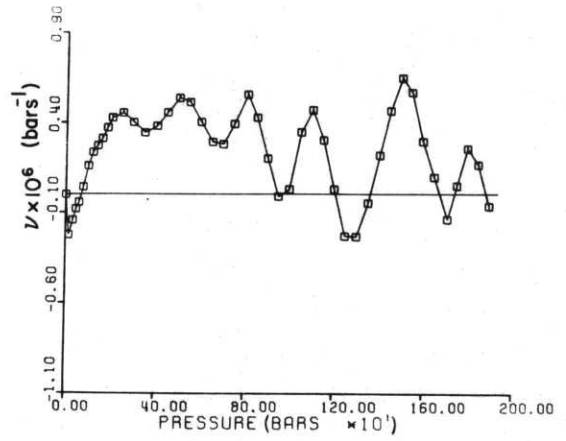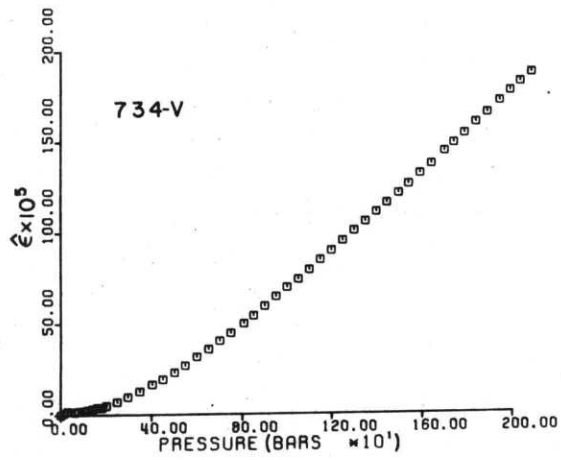
Table 3.

Parameters of Shocked Samples.

Sample	P[kbar]	t[μsec]	ζ(2kbar) [%]	P_m [bars]	P_0 [bars]	Γ [bars]	β(2kbar) [Mb^{-1}]
1243-2	4.6	6.5	.404 ± .242	160	500	760	1.72
1243-3	9.8	3.1	.101 ± .187	120	630	1060	1.71
1132-1	6.0	3.2	.435 ± .087	100	360	530	2.41
1132-2	4.6	6.5	.746 ± .298	120	380	590	2.70
1331-1	6.0	3.2	.054 ± .065	150	800	1030	1.36
1331-2	4.6	6.5	.296 ± .165	200	670	1040	1.72
1374-1	6.0	3.2	.206 ± .165	190	580	870	2.23
1374-2	4.6	6.5	.867 ± .352	200	660	1020	3.24
178-2	5.5	6.5	.654 ± .261	200	480	760	1.74
734-2	4.6	6.5	.667 ± .300	180	510	840	2.38

caused by the primary compressive shock pulse and not by a later reflected rarefaction.

Every shocked sample contained some fractures that were visible on the surface although the rock was still competent. Also, there was a slight relief imprint of the sample surface, including these fractures, on the surface of the aluminum cover plate that was next to the sample during the shot. The presence of the fractures in this imprint shows that the fractures occurred while the sample was still under pressure, before the pressure release wave pulled the cover plate away from the sample. Strain gauges mounted near areas with large concentrations of visible fractures always indicated larger microcrack porosity than gauges mounted on the same sample farther from the visible cracks, suggesting that the microcracks and visible fractures were formed simultaneously by the same process.

If we know that the fractures occurred during the shock pulse, we still must ask whether any other possible fracture-producing mechanisms could be operative during the time that the sample is under pressure. The only such source of stresses large enough to fracture a rock sample is the arrival of rarefactions while the sample is still under pressure. The velocity of the shock created in aluminum with a driver plate velocity of 0.21 km/s is 5.41 km/s, based on the Hugoniot of figure 6 and a density $\rho_0 = 2.785$ g/cm^3. Thus, the reflected wave from the bottom of the sample holder assembly will not

arrive at the sample until about 12 μs after the shock front leaves the sample. The wave from the sides of the sample holder will arrive even later, so that the sample should be free from rarefactions during the 6.5 μs shock pulse. We conclude, then, that shock duration exerts a strong influence on fracture formation in rock samples subjected to shocks having durations in the range of several microseconds.

Steverding and Lehnigk (1971) and Rinehart (1968) have shown how a compressive shock can produce fractures in an elastically inhomogeneous medium, such as a rock, through reflection and refraction of the incident shock at grain boundaries and pores. If this mechanism is causing fractures in our shocked samples, we might ask why a pulse six microseconds long would produce higher crack porosity than a three microsecond shock pulse. Two possible explanations are that the longer pulse allows cracks to propagate to a greater length, increasing their contribution to porosity, and that the longer pulse provides more time for complex interference among pulses reflected at pores and grain boundaries and development of associated high stress concentrations, as described by Rinehart (1968).

The terminal velocity of crack propagation can be estimated by equating the work done by the applied stress to the energy associated with crack deformation plus the additional surface energy of the extending fracture. Calculations by Steverding and

Lehnigk (1970) and Jaeger and Cook (1969, p. 330) indicate that the terminal crack propagation velocity is roughly one-half of the sound velocity of a medium. Thus, an acoustic velocity of 5 mm/μs corresponds to a crack propagation velocity of 2.5 mm/μs. As this is a maximum crack propagation velocity, the hypothesis that some cracks could propagate to a greater length in six microseconds than in three microseconds in our 25 mm thick samples is reasonable. The dominant grain size of our samples varies from 0.5 mm to 5 mm, resulting in transit times of between 0.1 μs and 1 μs through individual grains. The durations of the shock pulses are long enough so that more complex interference effects might be expected to develop during the six microsecond pulse than during the three microsecond pulse.

Analysis of the details of the individual closure pressure distributions shown in figures 7 through 12 reveals that shock processes produce characteristic modifications of microcrack distributions in rocks. In examining the distributions, one should bear in mind that the errors in $\zeta(P_c)$ and $\nu(P_c)$ are greater at higher pressures because the error in the zero pressure intercept of the tangent to the strain curve corresponding to a given error in the slope of the tangent increases linearly with pressure. The high closure pressure fluctuations in $\nu(P_c)$ for several virgin samples are due to this effect. The power of the DSA technique to resolve the closure pressure spectrum decreases dramatically for samples of low crack porosity, since

the random errors in the data result in fluctuations in the calculated closure pressure distribution comparable to the magnitude of the expected distribution function. We use sample 1331-V (Mellen gabbro) to illustrate this problem. Although the area under the closure pressure spectrum shown in figure 8 corresponds to the very low crack porosity of 1331-V, the shape of the spectrum provides little information about the actual shape of the closure pressure distribution, except to indicate the absence of the prominent low closure pressure peak which is typical of both virgin and shocked samples.

All of the shocked samples, with the exception of 1243-3 (Frederick diabase), have prominent peaks in their spectra in the range 100 to 300 bars. Virgin samples 1374-V (Wausau granite), 1132-V (Westerly granite), and 178-V (Twin Sisters dunite) have low closure pressure peaks in their crack distributions; however, virgin samples 1331-V and 734-V (Laramie anorthosite) have no such peak. Sample 1243-V contained no cracks, so the crack spectrum is not defined.

The peak in the 734-V spectrum at P_c = 1500 bars is clearly preserved in the shocked specimen, 734-2, increased in magnitude by nearly a factor of five. Most of the crack porosity resulting from the shock in 734-2 was due to cracks closing at lower pressures and forming a low closure pressure peak, although such a peak was absent from the crack distribution of the virgin sample.

Sample 1132-V has a crack porosity over twice as high as that of any of the other virgin samples. The closure pressure distribution in both of the shocked samples of 1132 is remarkably similar in shape to the initial distribution, when compared to the rest of the rock samples. This observation, as well as the preservation of the 1500 bar peak in the closure pressure distribution of sample 734, suggests that prominent peaks in the crack closure pressure distribution of a rock sample are preserved and increased in magnitude by the shock process. If this is due to the modification of existing pre-shock cracks, then their width and length must both be increased to maintain a similar closure pressure. Alternatively, the closure pressure of the pre-shock and shock-induced cracks might be controlled by the same mechanism, for example, a limit on crack length imposed by grain size of a pre-existing set of fractures.

Closure pressure distributions of shock-induced micro-cracks do not simply mirror the closure pressure distributions present in the pre-shock samples. The predominant low closure pressure peaks present in almost all of the shocked samples lead us to infer that shocking of rock tends to produce crack distributions with a peak at low closure pressures. One shocked sample (1243-3) which initially contained no microcracks had a fairly broad crack distribution with only a minor low closure pressure peak; however, a prominent peak was evident in another

sample of the same rock (1243-2) which experienced a shock pulse of lower pressure than did 1243-3, but twice the duration.

A comparison of pre-shock and post-shock sample parameters (Tables 1 and 3, respectively) shows no obvious set of pre-shock parameters that control the post-shock microcrack distribution. As an aid to the identification of the important pre-shock samples parameters, we performed multiple regression analyses that fit our data to models of the form $y = a_0 + \Sigma a_i x_i$, where y is a post-shock parameter, and the x_i are the pre-shock sample parameters. Such a simple linear model is not appropriate to describe completely the microcrack distributions resulting from shock in rocks. However, both the model and the size of the data set are sufficient for us to characterize qualitatively the nature of the influence of the pre-shock parameters on the post-shock spectrum.

The quantities chosen to characterize the virgin state of the samples are listed in Table 1. $^i\zeta$(2kbar), the porosity due to cracks closing below 2 kbar; ^iP_m, the closure pressure corresponding to the largest peak in the closure pressure distribution; $^iP_0$, the median closure pressure; and $^i\Gamma$, the width of the closure pressure distribution are defined precisely in the 'DSA Techniques' section. The parameter r is the most common grain size (estimated from hand specimen), and $^i\beta$(2kbar) is the volumetric compressibility of the sample at two kilobars, an index of the elastic properties (and mineralogy) of the samples. The shock duration (t) is the final independent variable.

Shock pressure was not included in the regression, since, with the exception of one sample (1243-3), only a single shock pressure was generated in conjunction with each shock duration. Thus, the effect of shock pressure and shock duration could not be separated on the basis of these experiments. The experiments of Siegfried et al. (1977), however, indicate that crack porosity is directly proportional to shock pressure in a given sample. Because we observe that the lower shock pressure experiments result in the higher crack porosities, we conclude that shock duration is the factor controlling crack porosities in our experiments.

The parameters $\zeta(2kbar)$, P_m, P_0, and Γ are also used to characterize the post-shock crack distributions. In addition, the shock response of $\Delta\beta$, which is the difference between the virgin and post-shock volumetric compressibility of a sample at two kilobars is modelled. $\Delta\beta$ is related to the porosity due to cracks closing above two kilobars caused by the shock, although the actual porosity cannot be calculated without strain measurements to pressures at which the cracks are closed.

The stepwise regression procedure described by Draper and Smith (1966, chapter 6) was used to select the 'best' model for predicting each of the post-shock parameters from the pre-shock sample characteristics. Using this procedure, the simplest possible regression, $y = a_0$, where a_0 is the mean of the observations of y, is used as a starting point. The variables x_i

are then added one at a time until a satisfactory model is obtained. The criterion for including or removing a parameter x_i from the model is the partial F-test comparing the sum of the squares of the deviations from the mean $\langle y \rangle$ due to the inclusion of the x_i term in the model to the sum of the squares due to error in the model. If a greater than 90% probability is given by the F-test that the inclusion of the x_i term in the model is significant, then the x_i term is included in the model.

The results of regression analyses for the various post-shock crack distribution parameters are summarized in Table 4. The pre-shock variables are listed across the top of the table and the post-shock parameters along the left-hand side. If a pre-shock variable enters into the regression equation for a particular post-shock parameter, the probability of significance of the corresponding model term, as given by the F-distribution, is entered into the appropriate location in the table. Blanks in any row indicate that the corresponding variables do not enter into the regression equation for the post-shock parameter in question. Sample 1243 was not included in the regression analyses, since the pre-shock crack distribution parameters ^iP_m, $^iP_0$, and $^i\Gamma$ cannot be defined for it.

The shock duration is the dominant factor in the present set that controls the amount of crack porosity produced during our shock experiments. Both ζ and $\Delta\beta$ correlate strongly with t,

Table 4.

Results of Regression Analyses.

Post-shock parameters	Initial Parameters						
	$^i\zeta(2\text{kbar})$	^iP_m	$^iP_0$	$^i\Gamma$	r	$^i\beta$	t
$\zeta(2\text{kbar})$							.965
P_m	.985						
P_0	.993		.903				
Γ	.998		.935				
$\Delta\beta$						.973	

indicating that the six microsecond duration shock pulse pro-
duced a higher crack porosity due to cracks closing both above
and below two kilobars than the three microsecond shock pulse.
Although the large errors in ζ(2kbar) make resolution of
correlations difficult, post shock crack porosity does not seem
to be significantly related to any of the other pre-shock
parameters.

The shape of the crack spectra, as defined by P_m, P_0, and
Γ, in the shocked samples appears to be influenced strongly
by the pre-shock crack porosity. All three parameters decrease
with increasing initial crack porosity. P_0 and Γ are also in-
fluenced, although somewhat less strongly, by the width of
the initial spectrum. An increase in the width of the initial
crack distribution results in increases in the median closure
pressure and width of the crack distributions in the shocked
samples. The equations for P_m, P_0, and Γ determined by the
regression analyses are given below:

$$P_m = 205 - 700 \; {}^i\zeta \tag{4}$$

$$P_0 = 550 - 2600 \; {}^i\zeta + 0.232 \; {}^i\Gamma \tag{5}$$

$$\Gamma = 856 - 3620 \; {}^i\zeta + 0.277 \; {}^i\Gamma \tag{6}$$

Γ, P_0, and P_m are in bars; and ζ is in percent.

Figure 13 is a plot of P_m vs ${}^i\zeta$. The variation in P_m
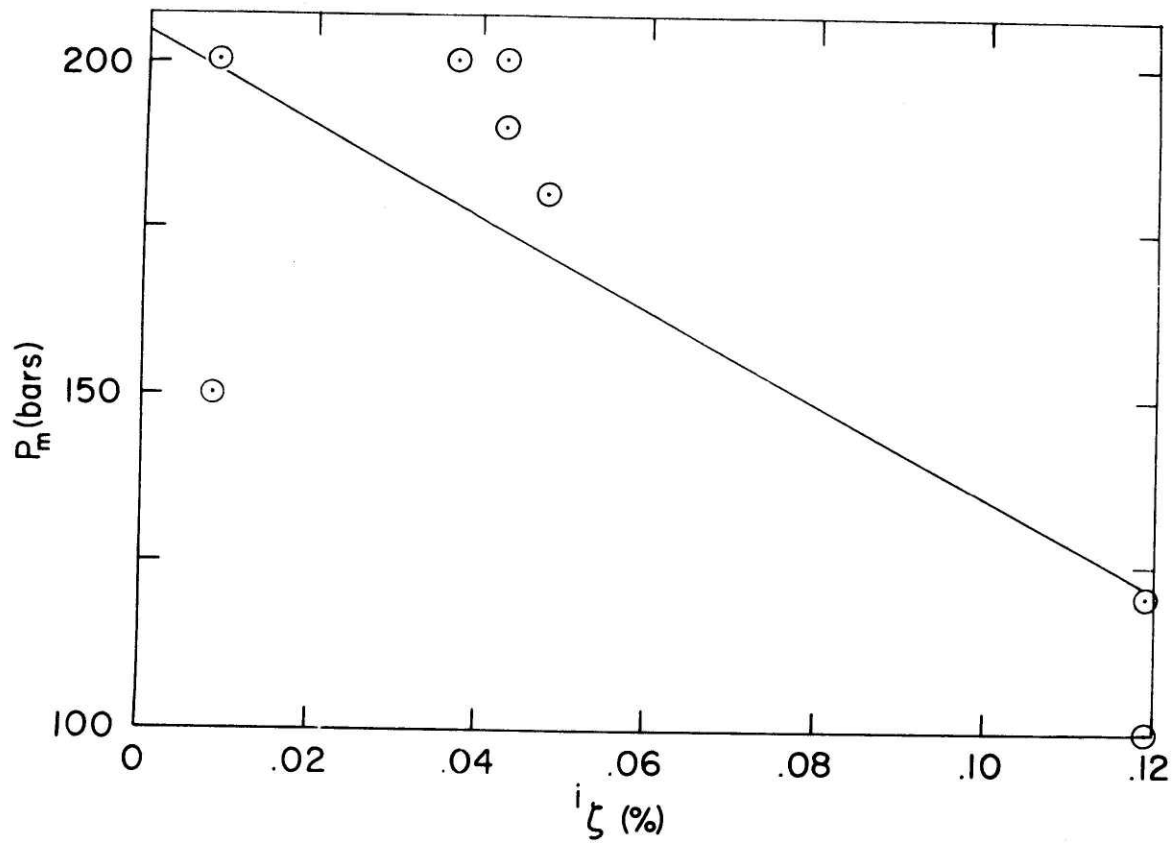within the suite of shocked samples is not large, illustrating

Figure 13. P_m as function of initial crack porosity. The least squares fit of equation (4) is shown by the solid line.

the ubiquity of low closure pressure peaks in the spectra of shocked samples. The lack of dependence of P_m on $^i\Gamma$ indicates that low closure pressure peaks persist, even at conditions that increase Γ and P_0.

The data in Table 5 illustrate the fit of the regression models for P_0 and Γ given in equations 5 and 6. The values of Γ and P_0 for each sample are shown, along with the values predicted by equations 5 and 6, and the residual, the difference between the actual and predicted values. The standard errors in the predictions, calculated from the regression analyses, are 63 bars for P_0 and 66 bars for Γ.

We infer that in low porosity igneous rocks the initial crack porosity exerts a dominant influence on the shape of the spectrum of shock-induced microfractures. Samples with large initial crack porosity tend to acquire relatively narrow closure pressure distributions, with lower median closure pressures when compared to samples with low initial crack porosity. The shape of the initial closure pressure distribution has a lesser influence on shock-induced microfractures, although there is some evidence that the width ($^i\Gamma$) of the initial closure pressure distribution correlates positively with the width and median closure pressure of the closure pressure distribution of shock-induced microcracks.

Table 5.

Fit of Regressions for P_0, Γ.

	P_0			Γ		
Sample	Predicted	Actual	Residual	Predicted	Actual	Residual
1132-1	359	360	+1	567	530	−37
1132-2	359	380	+21	567	590	+23
1331-1	717	800	+83	1052	1030	−22
1331-2	717	670	−47	1052	1040	−12
1374-1	605	580	−25	899	870	−29
1374-2	605	660	+55	899	1020	+121
178-2	484	480	−4	760	760	0
734-2	549	510	−84	884	840	−44

CONCLUSIONS

1. The duration of the shock pulse is the primary deter-
minant of the amount of crack porosity generated, for cracks
closing at both above and below two kilobars. There is no evi-
dence that any pre-shock sample parameters influences the amount
of post-shock crack porosity.

2. The shock process tends to preserve peaks at all
closure pressures present in the initial crack spectrum, although
the size of the peaks is increased greatly in the post-shock
samples. In addition to preserving existing peaks, shocking
tends to generate large peaks at closure pressures between 100
and 300 bars, even in samples that initially have no such peak
in their crack spectrum.

3. Although the amount of crack porosity in the shocked
samples was not significantly influenced by the pre-shock
porosity, the shape of the crack spectra of the shocked samples
depended fairly strongly on initial crack porosity. As the
initial crack porosity increased, post-shock spectra tended
to become narrower, with lower median closure pressures and
a peak value at lower closure pressures. The width of the
initial spectrum seemed to exert a weaker influence on the
post-shock distribution, with wider initial distributions
resulting in wider post-shock distributions with relatively
higher median closure pressures.

Neither the amount of shock-induced crack porosity nor the

shape of the spectrum was influenced by the grain size or high pressure (2kbar) compressibility of the virgin samples. The crack distributions in shocked igneous rocks, then, reflect the shock history of the rock and the initial crack distribution.

ACKNOWLEDGEMENTS

REFERENCES

Brace, W.F. and A.H. Jones, Comparison of uniaxial deformation in shock and static loading of three rocks, J. Geophys. Res., 76, 4913-4921, 1971.

Draper, N.R. and H. Smith, Applied Regression Analysis, John Wiley and Sons, New York, New York, 407 pp., 1966.

Duvall, G.E. and G.R. Fowles, Shock waves, in: High Pressure Physics and Chemistry, vol. 2, edited by R.S. Bradley, 209-291, Academic Press, New York, New York, 1963.

Feves, M., G. Simmons, and R. Siegfried, Microcracks in crustal igneous rocks: physical properties, in: The Nature and Physical Properties of the Earth's Crust, edited by J.G. Heacock, in press, 1976.

Gault, D.E. and E.D. Heitowit, The partition of energy for hypervelocity impact craters formed in rock, in: Proceedings of the Sixth Hypervelocity Impact Symposium, vol. 2, 419-456, Firestone Rubber Co., Cleveland, Ohio, 1963.

Hörz, F., Statistical measurements of deformation structures and refractive indices in experimentally shock loaded quartz, in: Shock Metamorphism of Natural Materials, edited by B.M. French and N.M. Short, 243-253, Mono, Baltimore, Md., 1968.

Hörz, F., Structural and mineralogical evaluation of an experimentally produced impact crater in granite, Contr. Mineral. and Petrol., 21, 365-377, 1969.

Jaeger, J.C. and N.G.W. Cook, Fundamentals of Rock Mechanics, Methuen and Co., London, 515 pp., 1969.

Klugman, M.A., Resume of the geology of the Laramie anorthosite mass, Mountain Geologist, 3, 75-84, 1966.

McQueen, R.G., S.P. Marsh, and J.N. Fritz, Hugoniot equation of state of twelve rocks, J. Geophys. Res., 72, 4999-5036, 1967.

McQueen, R.G., S.P. Marsh, J.W. Taylor, J.N. Fritz, and W.J. Carter, The equation of state of solids from shock wave studies, in: High Velocity Impact Phenomena, edited by R. Kinslow, 293-417, Academic Press, New York, New York, 1970.

Mendenhall, W., Introduction to Linear Models and the Design and Analysis of Experiments, Duxbury Press, Belmont, California, 465 pp., 1968.

Richter, D., G. Simmons, and R. Siegfried, Microcracks, micro-pores, and their petrologic interpretation for 72415 and 15418, Proc. Seventh Lunar Sci. Conf., in press, 1976.

Richter, D. and G. Simmons, Microcracks in crustal igneous rocks: microscopy, in: The Nature and Physical Properties of the Earth's Crust, edited by J.G. Heacock, in press, 1976.

Rinehart, J.S., Intense destructive stresses resulting from stress wave interactions, in: Shock Metamorphism of Natural Materials, edited by B.M. French and N.M. Short, 31-42, Mono, Baltimore, Md., 1968.

Ross, C.S., M.D. Foster, and A.T. Meyers, Origin of dunites and of olivine-rich inclusions in basaltic rocks, Am. Mineralogist, 39, 693-737, 1954.

Short, N.M., Effects of shock pressures from a nuclear explosion on mechanical and optical properties of granodiorite, J. Geophys. Res., 71, 1195-1215, 1966.

Siegfried, R.W., F. Hörz, and G. Simmons, Microfractures produced by a laboratory scale hypervelocity impact into granite, in preparation. 1977.

Siegfried, R. and G. Simmons, Characterization of oriented cracks with differential strain analysis, submitted, J. Geophys. Res., 1977.

Simmons, G., R. Siegfried, and D. Richter, Characteristics of microcracks in lunar samples, Proc. Sixth Lunar Sci. Conf., vol. 3, 3227-3254, 1975.

Steverding, B. and S.H. Lehnigk, Response of cracks to impact, J. Appl. Phys., 41, 2096-2099, 1970.

Steverding, B. and S.H. Lehnigk, Collision of stress pulses with obstacles and dynamics of fracture, J. Appl. Phys., 42, 3231-3238, 1971.

Todd, T., D.A. Richter, G. Simmons, and H. Wang, Unique characterization of lunar samples by physical properties, Proc. Fourth Lunar Sci. Conf., vol. 3, 2639-2662, 1973.

Walsh, J.M. and R.H. Christian, Equation of state of metals from shock wave measurements, Phys. Rev., 97, 1544-1556, 1955.

Chapter 4

Microfractures Produced by a Laboratory Scale

Hypervelocity Impact into Granite

Introduction

The physical characteristics of microcracks in lunar samples have been studied by Simmons et al. (1975) and Richter et al. (1976), who concluded that the crack closure pressure distributions, termed spectra, for lunar samples differ significantly from those of terrestrial samples. Since microcracks control many physical properties of rocks at pressures below a few kilobars (Thill et al., 1969; Brace, 1965; Simmons, 1964a and b; Birch, 1960 and 1961), knowledge of the microcrack distribution with depth in situ on the earth or the moon is necessary for the correct interpretation of in situ measurements of physical properties, for example, seismic velocity profiles.

To determine whether the microcrack distributions in returned lunar samples are likely to be similar to the in situ distributions, we must understand the mechanism causing the fractures. Todd et al. (1973) indicate that shock is the most important crack producing mechanism for lunar samples. Cracks in terrestrial samples produced under controlled shock conditions have only recently been studied by Siegfried et al. (1977) using the same techniques as Simmons et al. (1975) and Richter et al. (1976) used on the lunar samples. In an effort to expand the set of data available for the interpretation of lunar sample spectra, we have studied the cracks produced by a laboratory scale hypervelocity impact of an aluminum sphere into a block of granite.

We have used the differential strain analysis (DSA) technique described by Siegfried and Simmons (1977) to characterize the cracks produced previously in granite by the impact experiment of Hörz (1969). We have made DSA measurements on a suite of samples located at various distances from the point of impact. Since the pre-shock states of all samples were identical, we can isolate the effect of shock pressure on the production of microfractures. In addition, the orientation information available from DSA measurements enables determination of the relationship between the shock geometry and the symmetry of the resultant crack distribution.

Description of Impact Experiment

Hörz (1969) describes completely the impact experiment, the crater produced, and various shock metamorphic effects seen in samples from the granite block. We will describe briefly the experimental set up.

A granite block 60 cm x 60 cm x 36 cm was impacted with an aluminum projectile accelerated to 7.3 ± 0.3 km/sec by a two stage light gas gun. The projectile had a diameter of 1.26 cm and mass of 3.029 g. The modal composition of the granite, taken from Hörz (1969), is listed in Table 1, along with the compressibility of each of the component minerals (from Simmons and Wang, 1971). Figure 1 illustrates the geometry of the shot and the location of the slab, centered on the impact point, from which our samples were taken.

Table 1.

Modal Composition and Mineral Compressibilities

for the Granite Block.

Mineral	%	$\beta_v[Mb^{-1}]$
Quartz	27	2.63
Orthoclase	48	1.84
Plagioclase	12	1.68
Biotite	11	2.05
Accessories	2	
	100	

Figure 1. Geometry of shock experiment and sample locations.

The slab through the center of the crater outlined

with dashed lines in 1a is shown in 1b. The locations

of samples 2 through 13 relative to the direction of

shock propagation and the coordinate axes are shown.

Spall fractures produced by the reflected rarefaction

from the sides and rear of the block are shown by

light lines. Note the coordinate system which is

used for all of our results. The x_3 axis is orthogonal

to x_1 and x_2 and points out of the plane of the figure.

Figure 3 of Hörz (1969) is a photograph of the slab

in figure 1b.

60 cm

36 cm

7.3 km/sec

X_1

X_2

r

2
3
4
5
6
7
8
9
10
11
12
13

10 cm
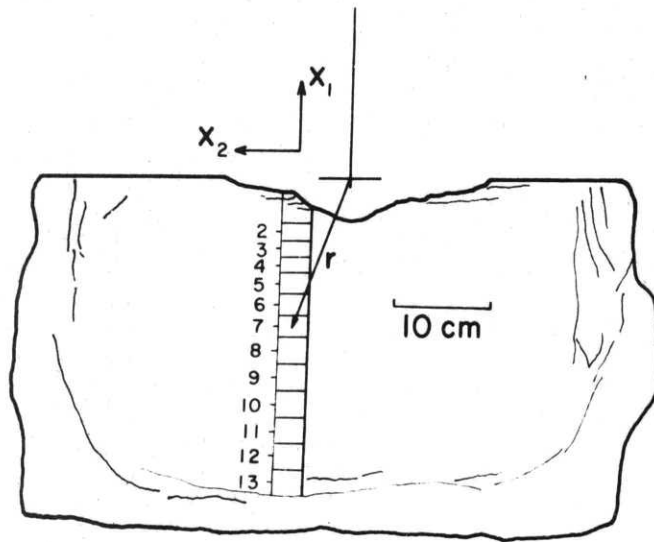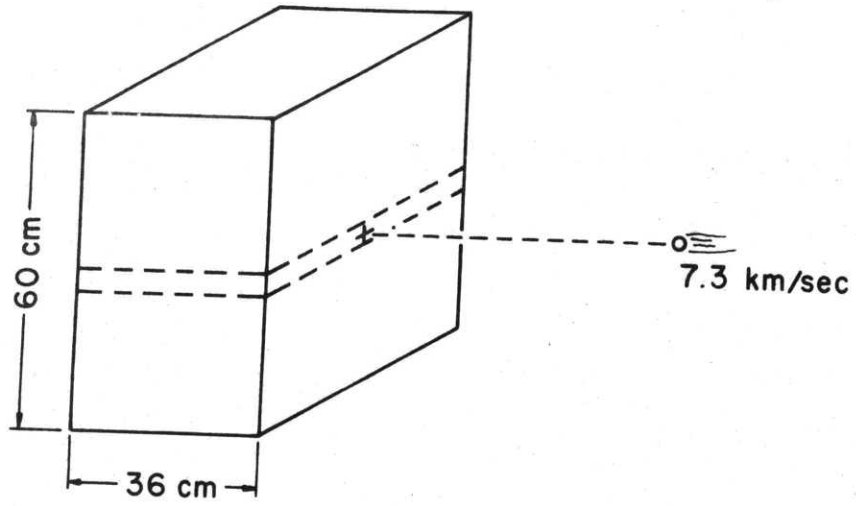
The locations of the samples that were prepared for DSA measurements are shown by numbers 2 through 13 on Figure 1. The samples do not lie along a line containing the impact point, and thus the direction of shock propagation through the samples varies somewhat. Since the samples are near the symmetry axis of the shot, the wave front is probably nearly spherical at the sample locations, and the shock propagation direction is well estimated by the vector from the impact point to the sample, shown as "r" in Figure 1.

The shock pressures in the granite block were calculated as a function of the distance (r) from the shot point by Hörz (1969), using the model of Gault and Heitowit (1963). The results of that calculation are shown in Figure 2. Locations of samples that we have examined with DSA are marked in Figure 2 by circles.

DSA Techniques

The DSA technique that we use to characterize microcracks is described by Siegfried and Simmons (1977). High precision measurements of the linear strain of a rock sample under hydrostatic pressure are used to determine the zero pressure strain in the sample due to the presence of cracks closing at various pressures.

The parameter $\zeta(P_c)$ is the zero pressure strain due to cracks closing by pressure P_c. The crack closure pressure distribution, termed crack spectrum, is given by $\nu(P_c)dP_c$, the zero pressure strain due to cracks closing between P_c and $P_c + dP_c$.
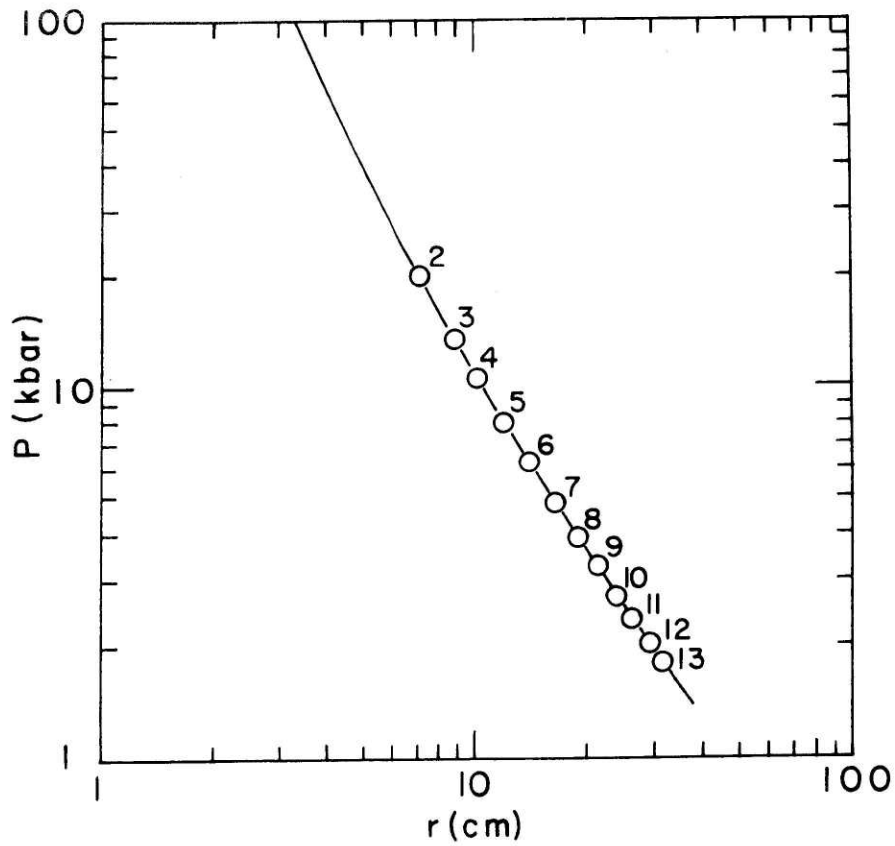
Figure 2. Calculated shock pressure (P) versus distance from impact point (r). Sample locations are shown by circles with the sample numbers indicated.

ζ and ν can be either volumetric, linear, or tensor quantities. If they are volumetric (ζ_v, ν_v), the zero pressure strain that they represent is porosity. Linear parameters ζ_i and ν_i provide information about the zero pressure linear strain due to cracks in the particular direction x_i in the same way that porosity is a measure of the zero pressure volumetric strain due to cracks. The tensor quantities ζ_{ij} and ν_{ij} reflect the complete zero pressure strain tensor due to the presence of cracks closing at the appropriate pressures.

Linear strain measurements in any three orthogonal directions are sufficient and also necessary in general to determine $\zeta_v(P_c)$ and $\nu_v(P_c)$. Strain data in at least six independent directions are required to calculate the tensors $\zeta_{ij}(P_c)$, $\nu_{ij}(P_c)$. If data in more than six independent directions are available, the redundant information can be used to estimate the error in each of the tensor components, and in the volumetric parameters ζ_v and ν_v given by the traces of ζ_{ij} and ν_{ij}. The principal values of ζ_{ij} and ν_{ij}, and the orientations of their principal axes, provide information about the orientations of cracks closing at various pressures. Actual crack orientations cannot be resolved; however, any directions of preferred orientation can be determined. Linear, volumetric, and tensor compressibilities, β, can also be calculated as a function of pressure from DSA data.

Several parameters are needed to characterize the shape of a crack spectrum $\nu(P_c)$. $\zeta(2 \text{ kbar})$ is the zero pressure strain due to cracks closing below two kilobars. It is the total area

under the $\nu(P_c)$ curve from $P_c = 0$ to $P_c = 2$ kbar. Since most cracks are closed by 2 kbar in terrestrial igneous rocks, $\zeta(2$ kbar$)$ is very close to the total zero pressure strain due to cracks (total crack porosity, in the volumetric case). The median closure pressure P_0, is defined as the pressure by which the cracks accounting for one half of the porosity closing below two kilobars are completely closed ($\zeta(P_0) = \zeta(2$ kbar$)/2$). The width of a closure pressure distribution is characterized by the parameter Γ, equal to the total porosity divided by the maximum value of ν, ($\Gamma = \zeta(2$ kbar$)/\nu_{max}$).

Results

Nine to eleven strain gauges were mounted on each sample. However, due to various experimental difficulties, the complete strain tensor was obtained on only eight samples. For samples 2 and 3, we have data from three orthogonal strain gauges, so that the volumetric strain and the diagonal terms of the strain tensor can be estimated; however, the errors associated with these strains cannot be estimated. We have no low pressure strain data for sample 10; therefore, we report only the com-pressibility $\beta_{ij}(2$ kbar$)$. Strain data from sample 4 are not available in any of the directions x_1, x_2, and x_3, but the data for the directions that are available are consistent with the other data reported herein and are not included in this paper.

The coordinate system to which our measurements are re-ferred is shown in Figure 1. The shock propagation direction lies in the x_1-x_2 plane.

Differential strain data for a typical sample (number 6) are shown in Figure 3. Figure 3a shows each of the components of the differential strain tensor $\hat{e}_{ij}$ as a function of pressure. The principal values and axes of $\hat{e}_{ij}$ are shown in Figures 3b and 3c. The shock propagation direction is indicated on Figure 3c. The crack spectrum $\nu_{ij}(P_c)$ calculated from the data of Figure 3 is shown in Figure 4.

Many important features of the DSA data for sample 6 are common to all of the samples. A prominent peak in the closure pressure distribution at P_c < 300 bars is present in each sample, although some cracks always close at higher pressures. The orientations of the principal axes of ν_{ij} do not show systematic variation with pressure, and tend to be fairly well defined, implying that cracks closing at all pressures have similar orientations. The slight systematic changes in the principal axes of $\hat{e}_{ij}$ with pressure are probably due to slight differences in the orientations of cracks closing above two kilobars and those closing at lower pressures. (See Siegfried and Simmons (1977) for a more complete description of the interpretation of the principal axis orientations of $\hat{e}_{ij}$, ζ_{ij}, ν_{ij}.)

Since the gross features of the crack distributions of all samples are similar to those of sample 6, we have not illustrated each distribution. The differences in the crack distributions can be seen from the parameters tabulated in Tables 2 and 3 and the principal axis orientations plotted in Figure 5. Table 2 includes values of ζ_{ii}(2 kbar) (no summation) and the

a.

b.

c.
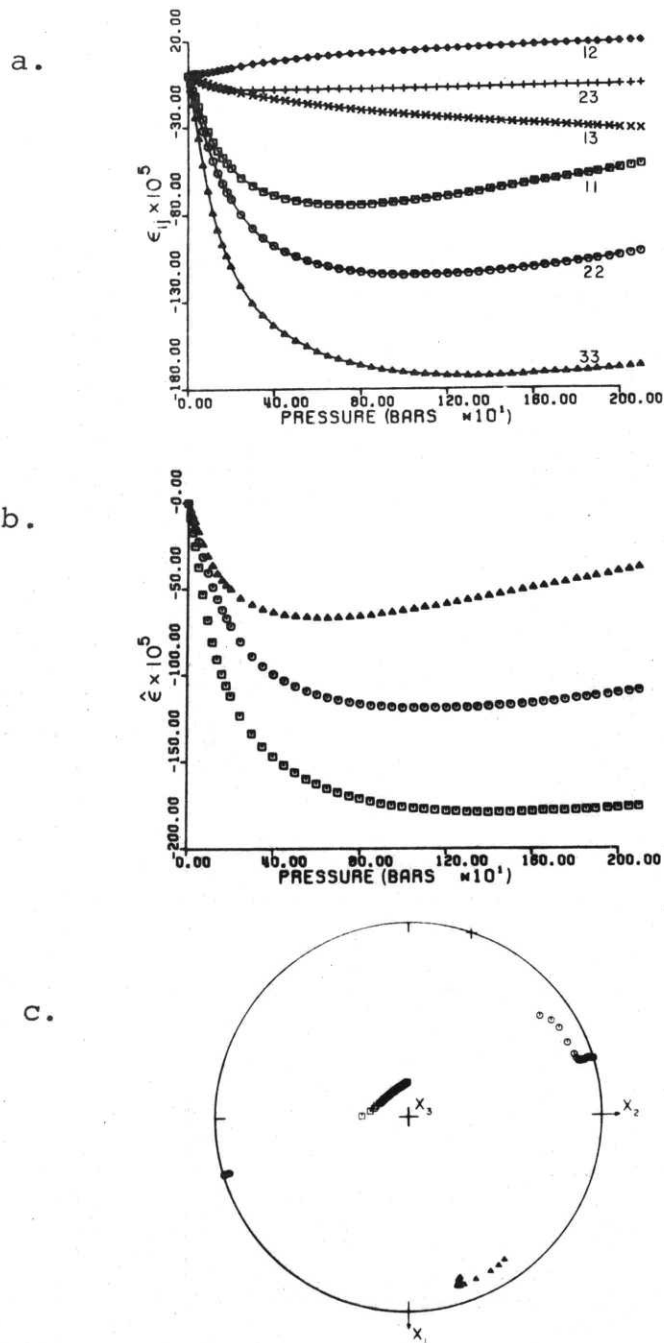
Figure 3. Differential strain data for sample 6. Figure 3a
shows each component of the differential strain
tensor, $\hat{\varepsilon}_{ij}$, as a function of pressure. Figures 3b
and 3c illustrate the principal values of $\hat{\varepsilon}_{ij}$ and
the orientation of the principal axes. The shock
propagation direction is shown by a cross.

Figure 4. Crack closure pressure distribution for sample 6. Figure 4a shows each component of $\nu_{ij}(P_c)$. The principal values of $\nu_{ij}(P_c)$ and the orientations of the principal axes are shown in figures 4b and 4c.

Table 2.

DSA Parameters of Shocked Samples.

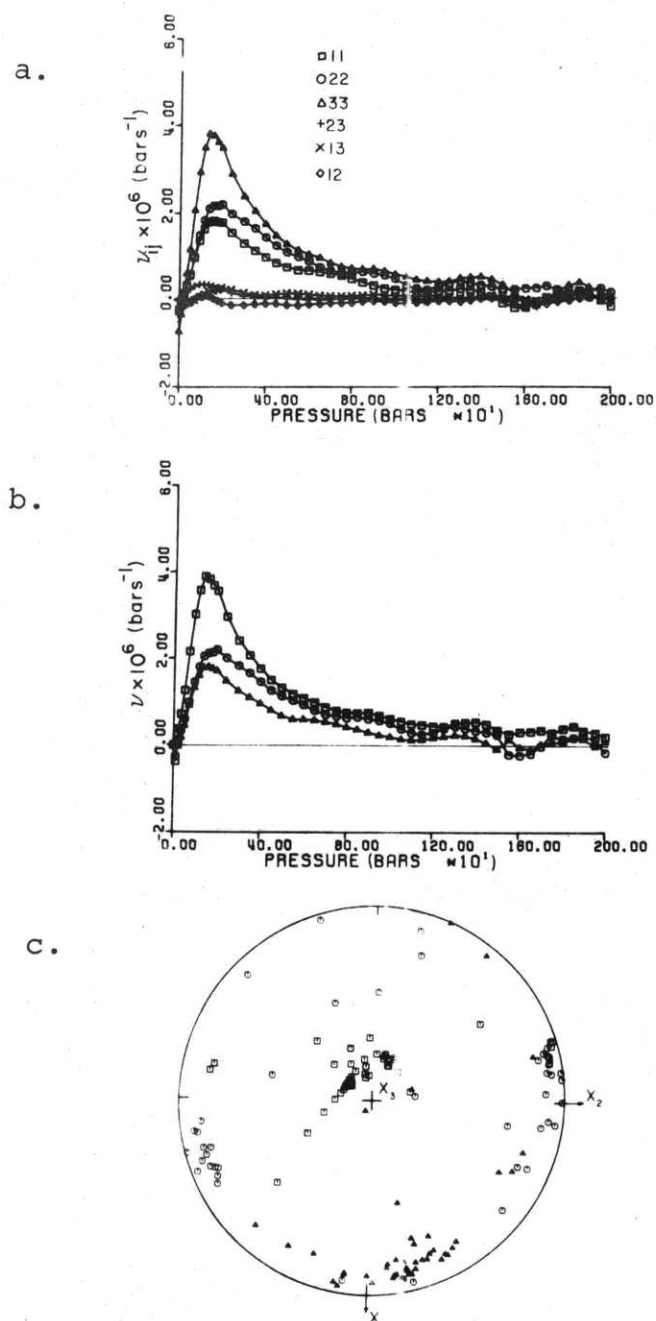| Sample	Component[1]	r (cm)	P (kbar)	ζ(2kbar) %	P_0 bars	Γ bars
2	11	7.1	20	.387	520	765
	22			.235	540	799
	33			.494	530	869
	V			1.116	540	818
3	11	8.8	13.5	.177	480	663
	22			.218	560	831
	33			.294	500	675
	V			.689	520	720
5	11	12.0	8.0	.130±.026	460	642
	22			.175±.025	440	603
	33			.232±.030	400	523
	V			.537±.040	430	575
6	11	13.9	6.3	.096±.045	360	523
	22			.142±.055	450	643
	33			.189±.067	370	495
	V			.427±.075	380	549
7	11	16.4	4.8	.083±.029	340	421
	22			.108±.034	380	477
	33			.180±.033	380	445
	V			.371±.046	370	450
8	11	18.9	3.9	.073±.026	320	451
	22			.106±.020	350	494
	33			.155±.019	340	466
	V			.334±.030	340	471

Table 2 (continued).

Sample	Component[1]	r (cm)	P (kbar)	ζ(2kbar) %	P_0 bars	Γ bars
9	11	21.5	3.3	.063±.002	320	413
	22			.091±.002	400	525
	33			.144±.004	400	494
	V			.298±.004	380	487
10	11	24.1	2.7	.052±.003	440	594
	22			.070±.004	480	592
	33			.141±.004	410	565
	V			.263±.005	440	604
11	11	26.6	2.3	.064±.014	360	475
	22			.078±.013	380	514
	33			.129±.014	400	531
	V			.271±.019	380	513
12	11	29.0	2.0	.072±.024	360	405
	22			.111±.026	380	460
	33			.128±.026	380	444
	V			.311±.036	380	443
13	11	31.5	1.8	.124±.052	400	503
	22			.079±.042	320	451
	33			.167±.030	390	513
	V			.370±.062	370	495

[1]The symbol 'v' in the component column refers to volumetric parameters.

corresponding parameters Γ and P_0 for each sample. Parameters
characterizing the volumetric crack strains are also tabulated.
The elements of the compressibility tensor β_{ij}(2 kbar) are
tabulated in Table 3. The axes x_1, x_2, and x_3 shown in Figure
1 are the reference axes for the tensor quantities in Tables 2
and 3. Since our data is insufficient for the calculation of
the complete tensor ζ_{ij}(2 kbar) of the two samples nearest the
impact point (samples 2 and 3), we have tabulated the values of
ζ(2 kbar) in the reference directions (ζ_{ii}) rather than the
principal values. Fortunately, as Figure 5 illustrates, the
principal axes of ζ_{ij}(2 kbar) are near the reference axes for
most samples. The orientations of the principal axes of
ζ_{ij}(2 kbar) for all samples for which tensor data are available
are shown in Figure 5. The orientations shown represent princi-
pal axes for cracks closing at all pressures ($\leq$ 2 kbar) in each
sample. (No systematic variation of orientation with crack
closure pressure was observed, as illustrated in Figure 4c
for sample 6.) The shock propagation directions for the samples
are also shown on the projection.

The principal axes of the crack distributions do not
reflect the symmetry of the shock. For each sample the maximum
principal axis of ζ(2 kbar) lies near x_3. With the exception
of sample 13, the intermediate and least principal axes of
ζ(2 kb) are near x_2 and x_1, respectively. If cracks were
formed with normals parallel to the direction of shock propaga-
tion, and pre-shock fractures were isotropic, then we would
expect $\zeta_{22} \sim \zeta_{33} < \zeta_{11}$. If cracks were formed with normals

Table 3.

Compressibility Tensor β_{ij} (2kbar).

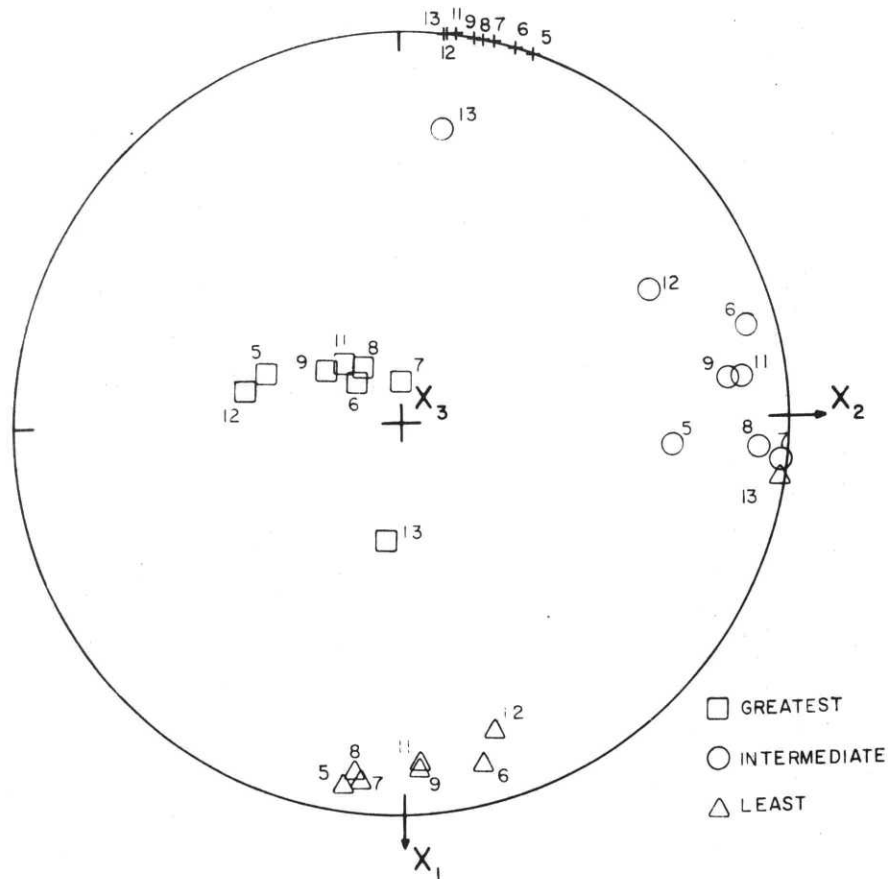|	Component (Mbar^{-1}) [$\pm$.010]					
Sample	11	22	33	23	13	12
2	.796	.759	1.11	--	--	--
3	.761	.790	.922	--	--	--
5	.719	.752	.902	.017	.031	-.084
6	.704	.723	.815	-.021	.069	-.040
7	.701	.689	.834	.025	-.016	.022
8	.731	.712	.765	-.022	-.003	.006
9	.723	.752	.804	-.023	-.001	-.012
10	.724	.696	.791	-.010	.018	-.027
11	.723	.708	.794	.019	.010	-.017
12	.713	.717	.766	-.020	-.023	.022
13	.717	.711	.820	.011	-.033	-.009

Figure 5.   Principal axes of ζ_{ij} (2kbar) for each sample for which sufficient data is available to calculate the complete strain tensor.   Squares - maximum principal axes.   Circles - intermediate principal axes.   Triangles - least principal axes.   The shock propagation directions for these samples are shown by the crosses.

perpendicular to the shock propagation direction, we would expect $\zeta_{22} \approx \zeta_{33} > \zeta_{11}$. However, these expectations are not fulfilled by the experimental data. ζ_{33} exceeds ζ_{22} by 30 to 110%. Such a large difference can only be attributed to pre-existing anisotropy in the granite, either in the pre-shock crack distribution or mineral orientation. Although we have not statistically studied mineral orientation, we see no strong preferred mineral orientation in either hand specimen or thin section. We suggest that the pre-shock crack distribution is the most likely controlling factor.

The orientations of the principal axes of ζ_{ij} (2 kbar) for sample 13 differ from those of the rest of the samples. The intermediate axis of ζ (2 kbar) lies near x_1 and the least axis is near x_2. The location of sample 13 at the time of shock was near the area where spallation fractures due to the wave reflected from the rear surface of the block were observed macroscopically by Hörz (1969). We suggest that the interchange of the orientations of the intermediate and least principal crack strain axes in sample 13 is due to microscopic spall fractures with normals near x_1.

The degree of microfracturing produced by the decaying shock wave and the reflected rarefaction is illustrated in Figure 6. The values of ζ_{ii} (2 kbar) (no summation), representing the zero pressure crack strain in the reference directions, are plotted as a function of r, the radial distance from the impact point. The magnitude of ζ_{ii} (2 kbar) for each direction decays systematically with r and then increases slightly after
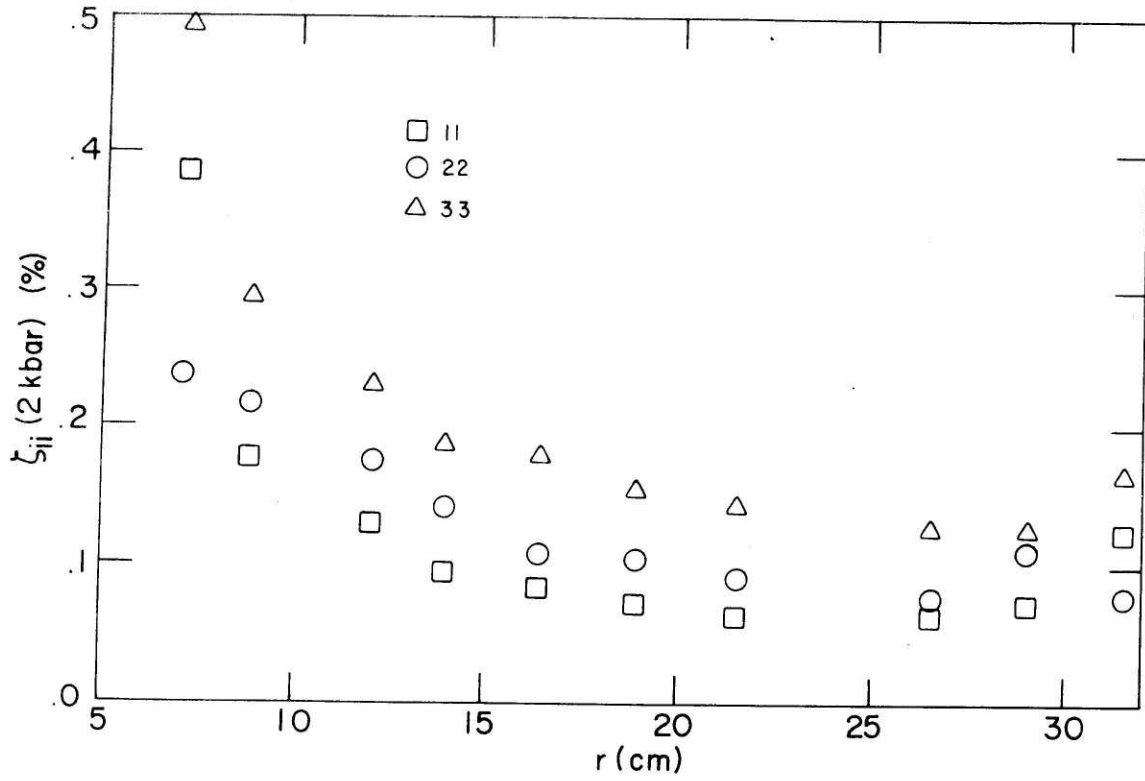
Figure 6. Zero pressure crack strain (ζ_{ii}(2kbar)) in directions x_1, x_2, and x_3 versus distance from impact point (r).

r = 29 cm, presumably due to the presence of spall fractures. With the exception of samples nearest to and farthest away from the impact point, the relative magnitudes of ζ_{11}, ζ_{22}, and ζ_{33} for an individual sample are similar, although each $\zeta_{ii}(r)$ depends strongly on r. The shock process has produced a distinctly anisotropic crack distribution that does not reflect the symmetry of the experiment. These data support our earlier conclusion that the orientations of the shock induced micro-fractures are primarily controlled by the pre-shock properties of the rock and not by the direction of shock propagation.

In the samples nearest to and farthest away from the impact point, ζ_{11} is greater than ζ_{22}. The x_1 axis is most closely aligned with the direction of shock propagation. The samples subjected to the highest shock and reflected rarefaction stresses have a greater percentage of their crack porosity oriented normal to the direction of shock propagation than the other samples.

A plot of $\zeta_{ii}(2 \text{ kb})/\zeta_v(2 \text{ kb})$ for each reference direction as a function of distance from the shot point, as in Figure 7, is a sensitive indicator of preferred microcrack orientations. A clear relation is evident between the proportion of crack strain in the x_1 direction and the distance from the impact point for samples with $r \leq 12$ cm. Thus, the shock passage has increased the fraction of cracks with normals parallel to the direction of shock propagation, although the post shock crack distribution is dominated by the pre-shock sample characteristics.
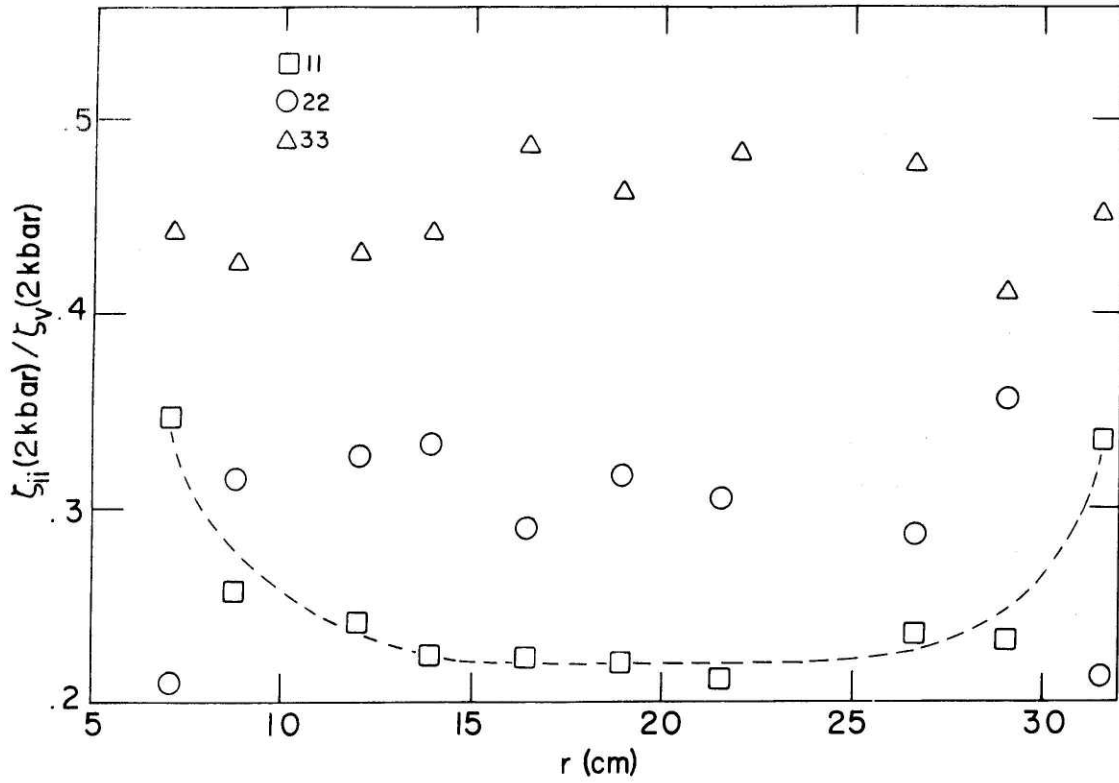
Figure 7. Proportion of the total zero pressure crack strain ζ_{ii}/ζ_v in each reference direction as a function of distance from the impact point (r).

Figure 8 illustrates the dependence of crack porosity on shock pressure. The errors in ζ_V(2kbar) estimated from redundant strain data are shown on the figure. Except for the porosity due to spall fractures in the three samples farthest from the impact, a linear relation between crack porosity (ζ_V(2kbar)) and shock pressure is indicated. The line drawn in Figure 8 is a least squares fit through the data points, described by the following equation:

$$\zeta_V = .140 + .047 \ P \qquad (1)$$

where ζ_V is in percent and P is shock pressure in kilobars. We do not suggest that this particular relationship be used to predict crack porosity in other types of samples exposed to different conditions of shock loading; however, these data do indicate that crack porosity and shock pressure are likely to be linearly related for low porosity igneous rocks subjected to shock pressures below 20 kbar.

Crack porosities for several granodiorite samples shocked by the Piledriver nuclear test are reported by Simmons et al. (1974). For samples that have been exposed to shock pressures below 20 kbar, they find crack porosities of about 0.1%, and see no systematic variation of crack porosity with shock pressure. The fractures generated by similar shock pressures in the Piledriver event and in a laboratory scale impact thus appear to be quite different. These differences could be due to differences either in the pre-shock characteristics of the rocks or the shock conditions to which the samples were exposed.
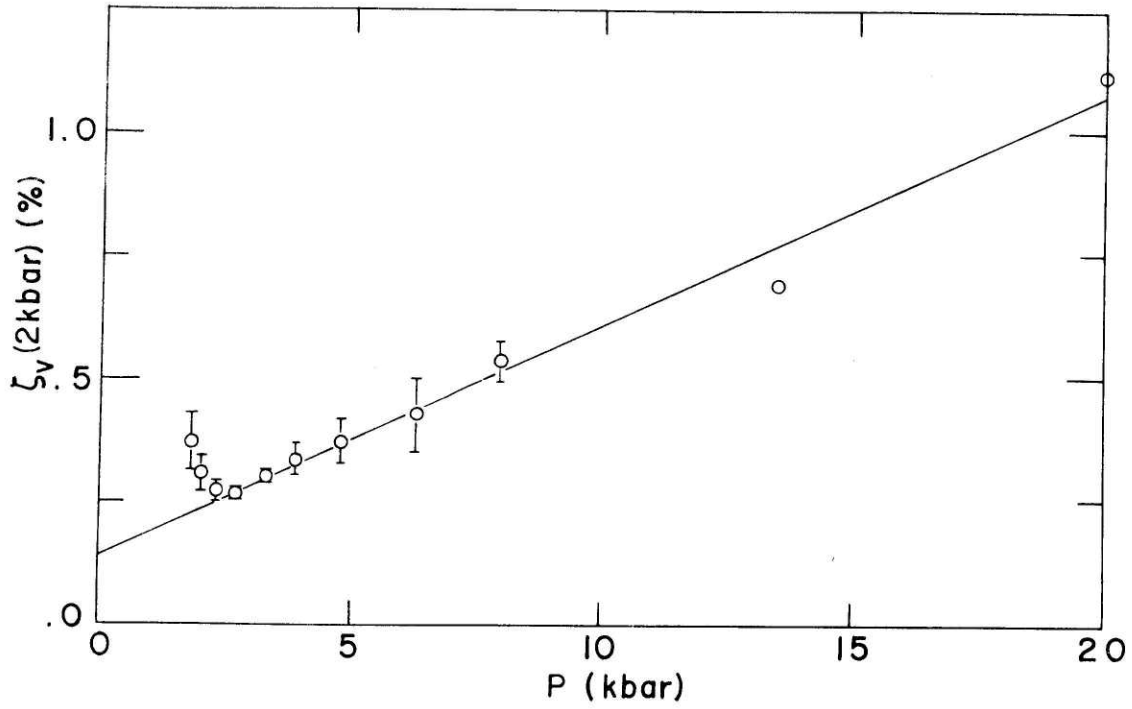
Figure 8. Porosity due to cracks closing below two kilobars
(ζ_v(2kbar)) versus shock pressure. The errors shown
are estimated from redundant strain data, and are
due to inhomogeneities in the crack distributions.

Siegfried, McQueen, and Simmons (1977) did not find evidence that pre-shock sample characteristics influenced the crack porosity produced in their experimentally shocked samples. The large uncertainties in the post-shock crack porosities they report, however, made such correlations difficult to resolve. Siegfried, McQueen, and Simmons (1977) did observe that the pre-shock crack porosity strongly influences the shape of the post-shock crack spectrum, and we have noted the large effect that pre-existing fractures seem to have on the orientations of shock-induced cracks. We think that pre-shock crack porosity is probably an important factor affecting the shock-induced crack porosity of a sample.

The pre-shock porosity of our experimentally shocked granite can be estimated from equation (1) to be 0.14%. The porosity reported by Simmons et al. (1974) for the pre-shock Piledriver sample is 0.10%. We have measured a crack porosity of 0.029% for a different pre-shock Piledriver sample. The large difference in the porosity of the two pre-shock samples indicates that the initial crack distribution in the Piledriver samples may have been very heteregeneous, and that the initial porosity of any given sample might have been quite different from either of the two reported values. In particular, the lower initial porosity of the two Piledriver pre-shock samples is more than a factor of five smaller than the initial porosity estimated for the laboratory shocked samples. Such low initial crack porosities could at least partially explain the relatively

low crack porosities in the shocked Piledriver samples.

The Piledriver samples, although subjected to similar shock pressures as our laboratory shocked samples, were shock loaded under somewhat different conditions. The duration of the shock, shown by Siegfried, McQueen, and Simmons (1977) to be an important factor controlling shock-induced crack porosity, is on the order of a few milliseconds for a nuclear explosion (Butkovich, 1965). The duration of the shock produced in a hypervelocity impact is controlled by the time required for the shock to propagate through the projectile (Gault et al., 1968). The 1.6 cm diameter aluminum projectile would thus generate a shock with a duration of approximately 2 μsec. Since Siegfried, McQueen, and Simmons (1977) found that shocks of longer duration produced higher crack porosity, the duration effect they observe is probably not responsible for the difference in porosity between the Piledriver samples and the samples shocked by the laboratory impact. The Piledriver samples had an overburden pressure of around 100 bars when they were shocked (Borg, 1973). Intuitively, we would suspect that the difference between the shock pressure and the pre-existing stress would control the shock-induced crack distribution, although we have no experimental data on samples shocked while under confining pressure. The curvature of the shock front was much greater for the laboratory impact samples than for the Piledriver samples. We have not experimentally determined the importance of shock front curvature, but we suspect that the difference between the shock curvature in the

two sets of samples might have accounted for some of the difference in shock-induced crack porosity. The differences between the cracks generated by the Piledriver test and by the laboratory impact emphasize the fact that laboratory results cannot be applied predictively unless all of the relevant parameters are identified and accounted for.

Although the crack porosity in our shocked samples and most terrestrial samples is greatly reduced at an effective pressure of two kilobars, considerable porosity in the form of both roundish pores and high closure pressure cracks might remain open at pressures of two kilobars (Brace, 1965). Although the actual amount of crack porosity cannot be determined without DSA measurements to pressures where all cracks are closed, the difference between β(2kbar) and the intrinsic compressibility calculated from the modal composition of the rock is an indication of the importance of high closure pressure porosity.

The Voigt and Reuss bounds (Hill, 1952) on the compressibility were calculated for an isotropic aggregate having the composition and component compressibilities listed in Table 1. The bounds on the linear compressibility (β_L) thus determined are .670Mbar^{-1} $\leq \beta_L \leq$ .687Mbar^{-1}. The linear compressibilities of the shocked samples are plotted in Figure 9. β_1 and β_2 are generally within 10% of the mean of the Voigt and Reuss bounds; however, β_3 is consistently higher than β_1 and β_2 and increases greatly with decreasing distance from the impact point, for r less than about 15 cm. Oriented microcracks closing at
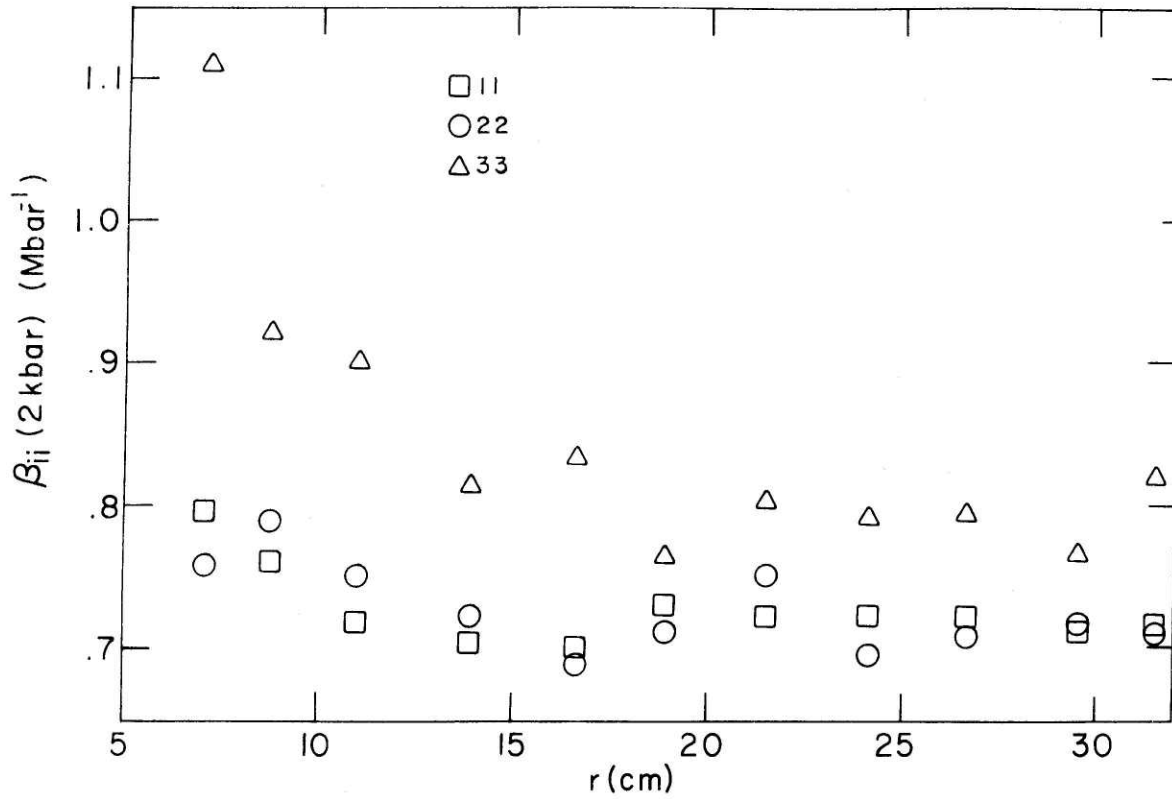
Figure 9. Linear compressibility at two kilobars in each of the three directions x_1, x_2, and x_3 versus distance (r) from impact point. The Voigt-Reuss bounds on intrinsic compressibility are 0.670 and 0.687 Mbar^{-1}.

pressures above two kilobars are produced by the shock; however, since we do not know whether the high value of β_3 relative to β_1 and β_2 in the low shock level samples is due to pre-shock crack porosity or preferred mineral orientation, these data do not allow us to determine which of these two parameters control the orientation of the shock-induced high closure pressure micro-cracks.

Simmons et al. (1975) and Richter et al. (1976) have indicated that the crack spectra for lunar samples differ markedly from those measured for both shocked and unshocked terrestrial samples. We have, therefore, investigated the shape of the crack spectra in our shocked samples, as character-ized by the width (Γ) and median closure pressure (P_0) defined in the "DSA Techniques" section of this paper. We observe no significant variation of Γ and P_0 among the diagonal elements (ν_{ii}) of the crack closure pressure distribution tensors for our samples. Therefore, we have plotted Γ and P_0 for volu-metric crack closure pressure distributions ($\nu_{11} + \nu_{22} + \nu_{33}$) in Figures 10 and 11.

Both the width and the median closure pressure of the crack distributions increase sharply as the impact point is approached. Although porosity of the shocked samples was greatly increased at all closure pressures, the shock process did tend to produce wider crack spectra with higher median closure pressures at higher shock pressures. The values of the parameters Γ and P_0 seem to stabilize for samples farther than about 15 cm from the shock point, where shock pressures were
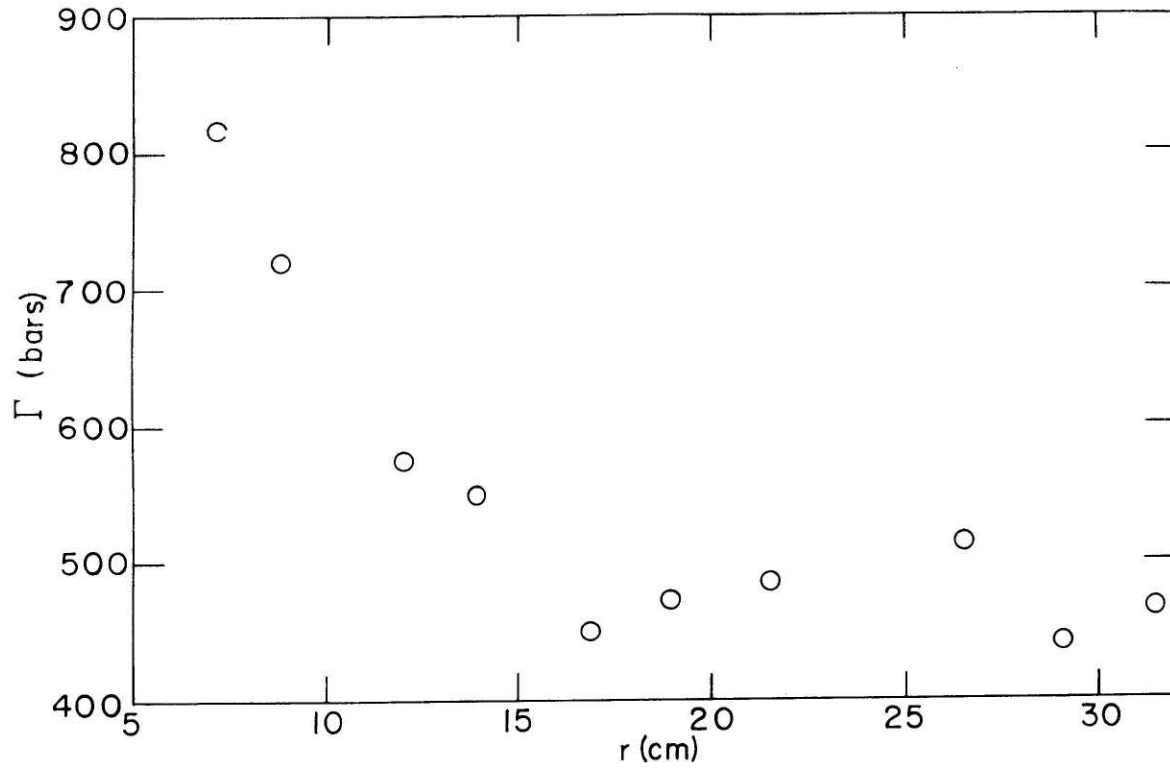
Figure 10. Width Γ of volumetric crack closure pressure distributions versus distance (r) from impact point. $\Gamma = \zeta_v(2\text{kbar})/\max(\nu_v)$.
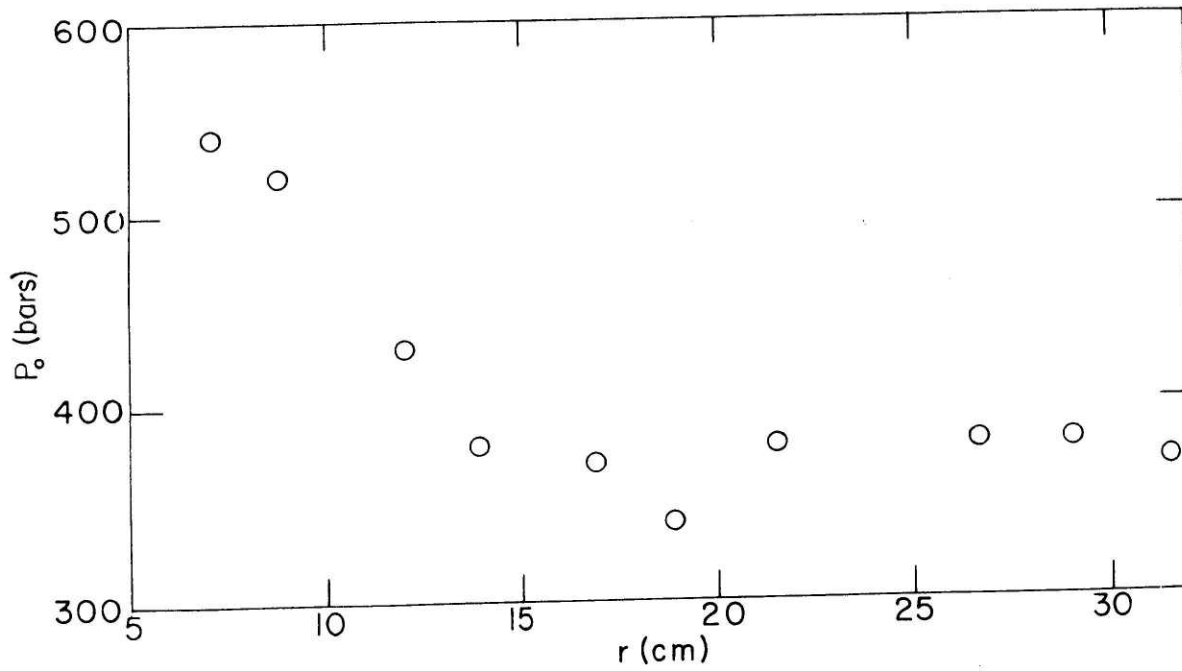
Figure 11. Median closure pressure P_0 of volumetric crack closure pressure distributions versus distance (r) from impact point. $\zeta(P_0) = \zeta(2kbar)/2$.

5 kbar or less. Thus, even though total crack porosity increases for samples experiencing shock pressures between 2 and 5 kbar, no changes in the shape of the crack distributions are evident in these samples. The shapes of the crack spectra for samples 12 and 13, which contain spall fractures, do not differ from those of the other low shock pressure samples.

Conclusions

1. The orientations of microcracks in low porosity samples shocked to pressures below 20 kilobars are controlled primarily by the initial anisotropy of the sample and not the direction of shock wave propagation.

2. Samples shocked to pressures higher than 5 kbar have a larger proportion of the shock-induced microcracks oriented with normals parallel to the direction of shock propagation than samples shocked to lower pressures. Samples containing spall fractures also tend to have a larger than normal (for a given shock pressure) proportion of their cracks oriented with normals parallel to the shock propagation direction.

3. The relationship between total crack porosity (closing below two kilobars) and shock pressure is linear over the pressure range of 2 to 20 kbar.

4. The differences in the compressibilities of the samples at two kilobars indicate that the porosity due to cracks closing above two kilobars in a sample is directly related to the shock pressure that sample has experienced.

5. The width and median closure pressure of shock-induced crack distributions are both directly related to shock pressure.

Increasing shock pressures result in wider crack distributions with higher median closure pressures.

Acknowledgements

References

Birch F. (1960) The velocity of compressional waves in rocks to 10 kilobars, part 1, J. Geophys. Res., 65, p. 1083-1102.

Birch F. (1961) The velocity of compressional waves in rocks to 10 kilobars, part 2, J. Geophys. Res., 66, p. 2199-2224.

Borg I.Y. (1973) Extent of pervasive fracturing around underground nuclear explosions, Int. J. Rock Mech. Min. Sci., 10, p. 11-18.

Brace W.F. (1965) Some new measurements of linear compressibility of rocks, J. Geophys. Res., 70, p. 391-398.

Butkovich T.R. (1965) Calculation of the shock wave from an underground nuclear explosion in granite, J. Geophys. Res., 70, p. 885-892.

Gault D.E. and Heitowit E.D. (1963) The partition of energy for hypervelocity impact craters formed in rock, in Proceedings of the Sixth Hypervelocity Impact Symposium, vol. 2, p. 419-456, Firestone Rubber Co., Cleveland, Ohio.

Gault D.E., Quaide W.L., and Overbeck, V.R. (1968) Impact cratering mechanics and structures, in Shock Metamorphism of Natural Materials, edited by B.M. French and N.M. Short, p. 87-99, Mono, Baltimore, Md.

Hill, R. (1952) The elastic behaviour of a crystalline aggregate, Proc. Phys. Soc. London (A), 65, p. 349-354.

Hörz F. (1969) Structural and mineralogical evaluation of an experimentally produced impact crater in granite, Contr. Mineral. and Petrol., 21, p. 365-377.

Richter D., Simmons G. and Siegfried R. (1976) Microcracks,
    micropores, and their petrologic interpretation for 72415
    and 15418, Proc. Lunar Sci. Conf. 7th, in press.

Siegfried R.W., McQueen, R.G., and Simmons G. (1977) Shock-
    induced microfractures in six terrestrial igneous rocks
    characterized with differential strain analysis, in
    preparation.

Siegfried R.W. and Simmons G. (1977) Characterization of oriented
    cracks with differential strain analysis, submitted to
    J. Geophys. Res.

Simmons G. (1964a) Velocity of compressional waves in various
    minerals at pressures to 10 kilobars, J. Geophys. Res., 69,
    p. 1117-1121.

Simmons G. (1964b) Velocity of shear waves in rocks to 10 kilo-
    bars, 1, J. Geophys. Res., 69, p. 1123-1130.

Simmons G. and Wang H. (1971) Single Crystal Elastic Constants
    and Calculated Aggregate Properties, MIT Press, Cambridge,
    Mass., 370 pp.

Simmons G., Siegfried R., Richter D., and Schatz J. (1974)
    Estimating peak shock pressures for lunar rocks (abstract),
    in Lunar Science V, p. 709-711, The Lunar Science Institute
    Houston.

Simmons G., Siegfried R., and Richter D. (1975) Characteristics
    of microcracks in lunar samples, Proc. Lunar Sci. Conf.
    6th, p. 3227-3254.

Thill R.E., Willard R.J. and Bur T.R. (1969) Correlation of

longitudinal velocity variation with rock fabric, J. Geophys.
Res., 74, p. 4897-4909.

Todd T., Richter D.A., Simmons G., and Wang H. (1973) Unique
characterization of lunar samples by physical properties,
Proc. Lunar Sci. Conf 4th, p. 2639-2662.

Chapter 5

Are the Microcracks in Lunar Samples Representative
of Those *In* *Situ* in the Lunar Crust?

INTRODUCTION

Data obtained with the differential strain analysis (DSA) technique on lunar samples differ greatly from similar data obtained on virgin and shocked terrestrial samples [1,2,3,4]. On the basis of these new data, we believe that the many data obtained already in the laboratory on the physical properties of lunar samples as a function of pressure should not be used directly to estimate the properties of lunar material within the moon. In the rest of this paper, we explain why.

THE DSA TECHNIQUE

Differential strain analysis (DSA) yields information on the nature of cracks in rocks [5,6]. Specifically, from DSA data we obtain the hydrostatic pressure at which different sets of cracks close. If the data set is complete (i.e., strains are measured in at least six independent directions as a function of pressure), then we obtain the second order tensor ζ_{ij} as a function of P_c, the crack closure pressure. $\zeta_{ij}(P_c)$ is the zero pressure strain tensor due to all cracks that close completely at pressures less than or equal to P_c. If strain data are available in three orthogonal directions, the volumetric zero pressure strain, or porosity, due to cracks closing at pressures less than P_c ($\zeta_v = \zeta_{11} + \zeta_{22} + \zeta_{33}$) can be determined. The crack porosity defined by Walsh [7] is $\zeta_v(P_{max})$, where P_{max} is the pressure by which all cracks are completely closed. Strain data in any single direction are sufficient to determine $\zeta(P_c)$ in that direction.

The crack closure pressure distribution $\nu_{ij}(P_c)$, or crack spectrum, is obtained by differentiating $\zeta_{ij}(P_c)$ with respect to P_c. $\nu_{ij}(P_c)dP_c$ is the zero pressure strain tensor due to cracks closing completely at pressures between P_c and P_c+dP_c. If the complete strain tensor is not determined, the linear or volumetric closure pressure distributions can be calculated from strain measurements in one direction or in any three orthogonal directions, respectively.

SUMMARY OF DSA RESULTS

The crack spectra for virgin, stressed, and shocked terrestrial igneous rocks reported by Simmons et al. [1], Feves and Simmons [8], Siegfried and Simmons [6], Siegfried, McQueen, and Simmons [3], and Siegfried, Hörz, and Simmons [4] differ substantively from the spectra for lunar samples reported by Simmons et al. [1] and Richter et al. [2]. The lunar samples typically have a large fraction of their porosity contained in cracks that close at pressures above one kilobar, and prominent peaks in the spectra are absent. Figure 1 illustrates the linear crack spectrum for lunar sample 14310,128, derived from DSA data in a single direction.

Most crack porosity in terrestrial samples is contained in cracks that close by one kilobar, and a prominent peak in the crack spectrum at some pressure below 400 bars is almost universal. We illustrate these features with data on two quite different terrestrial samples, virgin Westerly (RI) granite (MIT 1134) and experimentally shocked Frederick (MD) diabase (MIT 1243-2). See figure 2. The six components of the tensor crack spectrum, $\nu_{ij}(P_c)$, are shown for Westerly granite and the volumetric spectrum $\nu_v(P_c)$ is shown for Frederick diabase.

Although we have examined approximately 150 samples with DSA, the low closure pressure peak is absent from only two terrestrial samples, the virgin Mellen (WI) gabbro and the virgin Laramie (WY) anorthosite [3]. The Mellen gabbro has a crack
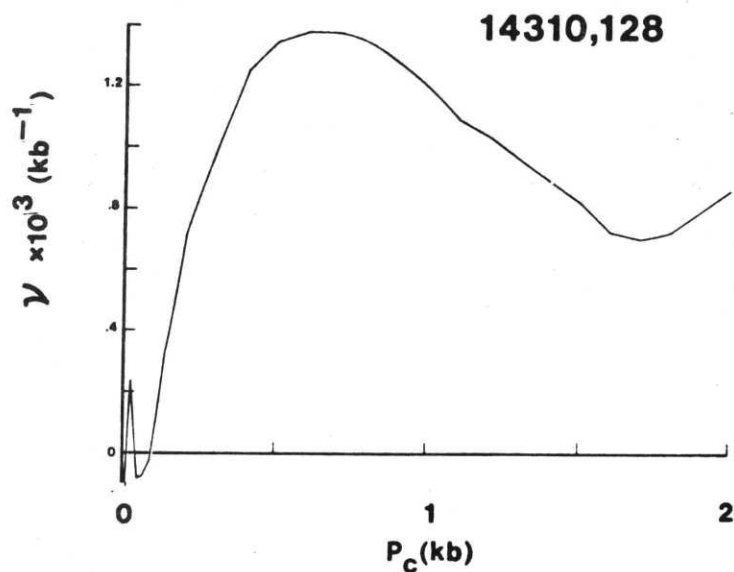
Figure 1. Crack spectrum for lunar sample 14310,128. This
spectrum was calculated from strain data in a single
direction. A large fraction of the porosity of
this sample is due to cracks that close at P_c > 1 kbar.
Although there is a broad maximum near P_c = 0.6 kbar,
the prominent peaks characteristic of terrestrial
samples (see figure 2) are absent. The fluctuations
in the spectrum for P_c < 0.1 kbar are an artifact
of the curve fitting technique used to calculate
the crack spectrum from the differential strain data.
(After Simmons et al. [1].)
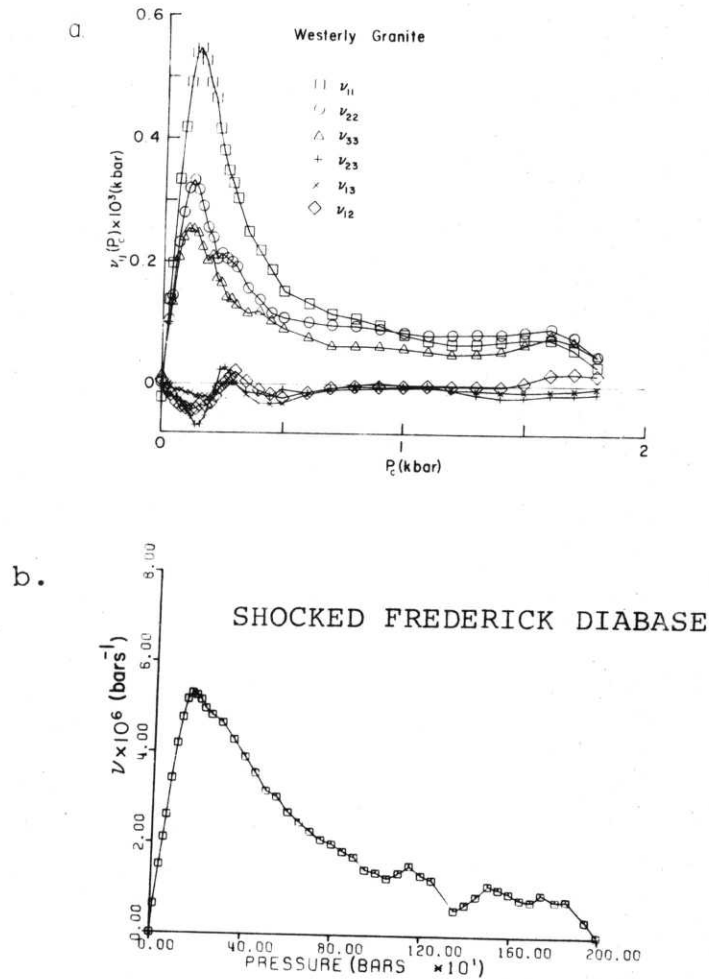
Figure 2.   Crack spectra for two terrestrial samples.   Figure 2a
            illustrates the tensor crack spectrum of Westerly
            granite (from Siegfried and Simmons [6]).   The volu-
            metric crack spectrum of an experimentally shocked
            sample of Frederick diabase is shown in figure 2b
            (from Siegfried, McQueen, and Simmons [3]).   In each
            sample, only a small fraction of the total crack
            porosity is due to cracks that close at P_c > 1 kbar.
            The prominent peaks at P_c < 0.4 kbar are character-
            istic of terrestrial samples, but absent in lunar
            samples.

porosity of .007 $\pm$ .005%, two orders of magnitude less than

that typical of the lunar samples, and so low that DSA cannot

resolve the details of the spectrum. We do not think that the

virgin Mellen gabbro, with its extremely low crack porosity, is

representative of the high crack porosity shocked lunar samples.

The Laramie anorthosite contains abundant healed and sealed cracks

visible in thin section and in hand specimen. We therefore

suspect that the crack spectrum has been altered by the exten-

sive healing and sealing of microcracks. Some lunar samples

characterized with DSA do not have such extensive healing

and sealing features, so we reject the hypothesis that the

absence of significant low closure pressure peaks in all of

the lunar sample crack distributions is due to healing and

sealing.

IMPLICATIONS OF DSA RESULTS

A pressure of two kilobars, the limit of existing DSA data, corresponds to a depth of about 40 km in the moon. The high values of the compressibilities at two kilobars reported by Simmons et al. [1] for lunar samples indicate a significant population of cracks closing at pressures higher than two kilobars. Thus, if the crack distributions in situ in the moon are similar to those in the returned samples, in situ physical properties (in particular, elastic properties) will be dominated by microcracks at depths to 40 km and beyond. In order to ascertain whether these cracks are likely to be present in situ, we must ask what process could form them and whether they would be preserved when the samples were brought to the surface of the moon. The most important mechanism for producing microcracks in the lunar crust is large shock stresses generated by meteorite impacts [9]. In this paper, we use the experimental results of Siegfried, McQueen, and Simmons [3] and Siegfried, Hörz, and Simmons [4] to assess the likelihood that the observed microcrack distributions might be generated by shock wave passage through the lunar crust and subsequent excavation by a meteorite impact.

The results of the laboratory shock experiments indicate that the width of a crack distribution and its median closure pressure increase with increasing shock pressures and decrease with increasing initial crack porosity. One shocked sample of

Frederick diabase studied by Siegfried, McQueen, and Simmons [3]
has a broad crack spectrum with a significant fraction of its
porosity due to cracks that close at pressures above one kilobar.
This sample had very low pre-shock porosity (zero, within the
resolution of the DSA technique) and was shocked to a higher
pressure than the other samples. Thus, it is possible that
regions of the lunar crust that have experienced passage of a
single shock wave with a pressure greater than those achieved
experimentally (about ten kilobars) might have a crack distribu-
tion similar to that observed in the lunar samples.

It is extremely unlikely, however, that a sample in the upper
40 km of the lunar crust has experienced only a single shock.
In each of the rocks having any pre-shock crack porosity, either
with or without a low closure pressure peak, a significant peak
at a closure pressure below 400 bars was produced by shock.
The widths of the resultant crack distributions, as well as
the median closure pressures, were strongly negatively correlated
with initial crack porosity. The crack porosity of lunar samples
determined from DSA measurements ranges from 0.17% to 1.6%.
Todd et al. [9] have measured crack porosities as large as 3.5%
for lunar samples. Crack porosities of terrestrial igneous rocks
are typically around 0.1% or below [3,6,10]. Based on the experi-
mental relation between initial porosity and crack closure pres-
sures, we conclude that rocks with the high porosity of the
lunar samples could not likely undergo repeated shocking in the

lunar crust without developing low closure pressure peaks in their crack spectra. In all of the shock experiments, if the spectrum of the pre-shock sample contained a low closure pressure peak, that peak was clearly preserved in the post-shock spectrum. We conclude that the broad crack spectrum characteristic of lunar samples is not likely to represent the crack spectrum in situ in the lunar crust.

If the crack spectra of lunar samples samples were not produced in situ, then how and where were they produced? In answer to this question, we can supply mainly informed speculation and suggestions for future work.

After subjecting samples with a range of mineralogy, grain size, and initial crack distributions to similar shock conditions, Siegfried, McQueen, and Simmons [3] concluded that only the shock conditions and the properties of the initial crack distribution exerted an important influence on the shock-induced microcrack distribution of a sample. Thus, the differences in the crack distributions among various lunar samples, reported by Simmons et al. [1], must represent real differences in the shock history of the samples and not merely differences in the response of the various rock types to the same shock conditions.

The lunar samples characterized with DSA include three mare basalts (15058, 15075, and 75055), one breccia (77035), one gabbroic anorthosite (15418), and one feldspathic basalt

(14310) thought to be a impact melt. This suite of lunar samples
includes rocks with very different shock and petrologic histories
that all have a crack distribution that was only reproduced
experimentally under the rather specialized condition of zero
initial porosity. We conclude that the crack distributions
were produced by conditions common to all of the samples that
were not reproduced in the experiments of Siegfried, McQueen,
and Simmons [3] or Siegfried, Hörz, and Simmons [4].

The passage of a shock wave through a rock under a confining
pressure of a few kilobars might create a different sort of
crack distribution than those observed in atmospheric confining
pressure experiments. We have not performed any DSA measure-
ments on rocks subjected to either static or shock stresses
under confining pressure, but the difference between the shock
stress and the confining pressure would likely determine the
post-shock crack distribution. Even if shocking under confining
pressure does affect shock-induced crack distributions, we
doubt that this mechanism could explain the lunar DSA results.
Some lunar samples have probably never been buried to signifi-
cant depths in the crust since the time of their last recrystal-
lization, for example 14310, thought to be an impact melt, and
15418, which contains abundant healed and glass-sealed cracks
[1,2]. Yet all samples without exception have similar crack
spectra. The distinctive crack spectra were likely produced
by a process that operated on all samples either during their

excavation from a massive rock unit to become a sample small enough to be collected by the astronauts, or after the excavation, while the samples were part of the lunar regolith.

The effect of shock on the microcrack distributions of the unconsolidated lunar regolith might be quite different from its effect on microcracks in competent rocks. The physical mechanisms of impact crater formation in an unconsolidated target [11] are quite different from those in a competent, low porosity igneous rock [12], reflecting the differences in the shock response of the two types of materials.

Rinehart [13] describes the way in which stress intensifications are generated by the interactions of the reflected and refracted waves accompanying the passage of a shock through an inhomogeneous medium. We would expect a shock passing through a highly porous material with relatively small grain to grain contacts to generate a much more complex pattern of shock wave interactions on the scale of the individual grains than a shock passing through a competent medium, in which most reflections are caused by the differences in shock impedance of various minerals.

The microcrack distributions produced in the individual grains (analogous to individual rocks in the lunar regolith) could be studied with driver plate experiments similar to those performed by Siegfried, McQueen, and Simmons [3]. Instead of a solid target, an unconsolidated target containing at least

some rock fragments a few centimeters in size could be constructed. Various ranges of grain sizes and degrees of sorting of the unconsolidated target could be studied.

We have not discussed one possible source of microfractures in the lunar samples. Cracks could be formed in the samples during the collection, transport, or preparation process. We have not studied cracks produced by the exact sample handling procedures used with the lunar samples. In our experience with terrestrial sample collection and preparation, however, we have never produced crack distributions similar to those in the lunar samples. Thermal stresses are potentially one of the most important sources of microfractures during lunar sample collection and preparation. Thermal cycling cracks have been studied by Simmons and Cooper [14], who conclude that they typically have closure pressures below a few hundred bars. We believe that the broad crack spectra in the returned lunar samples were probably present in these rocks when they resided on the lunar surface.

SUMMARY OF CONCLUSIONS

We believe that the crack distributions in returned lunar samples do not correspond to the crack distributions in situ in the lunar crust. Thus, measurement of crack-controlled physical properties (such as seismic velocity) as a function of pressure in the laboratory on returned lunar samples should not be used directly to interpret in situ measurements of the same properties. The reasons why in situ cracks are not likely to be similar to the cracks in the returned samples are summarized below:

1. Laboratory scale shock experiments indicate that broad crack spectra with a large fraction of porosity due to cracks that close above one kilobar could probably not be created or maintained by the passage of shock waves through material confined in the lunar crust.

2. The distinctive crack spectra of the returned lunar samples were most likely produced by either the process of excavating the samples from the crust of the moon to form the regolith or the effects of shock waves on the samples once they were part of the regolith.

ACKNOWLEDGEMENTS

REFERENCES

[1] G. Simmons, R. Siegfried and D. Richter, Characteristics of microcracks in lunar samples, Proc. Sixth Lunar Sci. Conf. 3 (1975) 3227-3254.

[2] D. Richter, G. Simmons and R. Siegfried, Microcracks, micropores, and their petrologic interpretation for 72415 and 15418, Proc. Seventh Lunar Sci. Conf (1976) in press.

[3] R.W. Siegfried, R.G. McQueen and G. Simmons, Shock-induced microfractures in six terrestrial igneous rocks characterized with differential strain analysis, in preparation (1977).

[4] R.W. Siegfried, F. Hörz and G. Simmons, Microfractures produced by a laboratory scale hypervelocity impact into granite, in preparation (1977).

[5] G. Simmons, R. Siegfried and M. Feves, Differential strain analysis: a new method for examining cracks in rocks, J. Geophys. Res. 79 (1974) 4383-4385.

[6] R. Siegfried and G. Simmons, Characterization of oriented cracks with differential strain analysis, submitted to J. Geophys. Res. (1977).

[7] J.B. Walsh, The effect of cracks on the compressibility of rock, J. Geophys. Res. 70 (1965) 381-389.

[8] M. Feves and G. Simmons, Effects of stress on cracks in Westerly granite, Bull. Seism. Soc. Am. 66 (1976) 1755-1765.

[9] T. Todd, D.A. Richter, G. Simmons and H. Wang, Unique characterization of lunar samples by physical properties, Proc. Fourth Lunar Sci. Conf. 3 (1973) 2639-2662.

[10] M. Feves, G. Simmons and R. Siegfried, Microcracks in crustal igneous rocks: physical properties, in The Nature and Physical Properties of the Earth's Crust, J.G. Heacock, ed., in press (1976).

[11] D. Stöffler, D.E. Gault, J. Wedekind and G. Polkowski, Experimental hypervelocity impact into quartz sand: distribution and shock metamorphism of ejecta, J. Geophys. Res. 80 (1975) 4062-4077.

[12] F. Hörz, Structural and mineralogical evaluation of an experimentally produced impact crater in granite, Contr. Mineral. and Petrol. 21 (1969) 365-377.

[13] J.S. Rinehart, Intense destructive stresses resulting from stress wave interactions, in Shock Metamorphism of Natural Materials, B.M. French and N.M. Short, eds. (Mono, Baltimore, Md., 1968) 31-42.

[14] G. Simmons and H. Cooper, Thermal cycling cracks in three igneous rocks, in preparation (1977).

ACKNOWLEDGEMENTS

BIOGRAPHICAL NOTE

The author was born in Elmhurst, Illinois in 1950. He attended public schools in Villa Park, Illinois, and graduated from Willowbrook High School in 1968. He was awarded an honorary Illinois State Scholarship and a sponsored National Merit Scholarship, which assisted in paying the bills at the California Institute of Technology. He graduated from Caltech in 1972 with a degree in Physics. The author attended M.I.T. from 1972 to the present, where he was supported by a Chevron Fellowship for two years, and a research assistantship for the remainder of the time. Previous publications of the author are listed below:

Siegfried, R.W., and S.C. Solomon, Mercury: internal structure and thermal evolution, Icarus, 23, 192-205, 1974.

Siegfried, R.W., G. Simmons, J. Schatz, and D. Richter, Effect of shock waves on elastic properties of rocks, EOS, 55, (ABS), 418, 1974.

Simmons, G., R.W. Siegfried, and M. Feves, Differential strain analysis: a new method for examining cracks in rocks, J. Geophys. Res., 79, 4383-4385, 1974.

Simmons, G., R. Siegfried, D. Richter, and J. Schatz, Estimating peak shock pressures for lunar rocks, Lunar Science V., (ABS), 709-711, 1974.

Simmons, G., R. Siegfried, and D. Richter, Characteristics of microcracks in lunar samples, Proc. Sixth Lunar Sci. Conf., in press, 1975.

Richter, D., G. Simmons, and R. Siegfried, Combined petrographic and scanning electron microscopy of microstructures in igneous rocks, (ABS), EOS, 56, 447, 1975.

Richter, D., G. Simmons, and R. Siegfried, Microcracks, micropores, and their petrologic interpretation for 72415 and 15418, in press, Proc. Seventh Lunar Sci. Conf., 1976.

Simmons, G., D. Richter, R. Siegfried, and M. Feves, Micro-
    cracks,in ancient rocks, (ABS), EOS, 57, 327, 1976.

Feves, M., G. Simmons, and R. Siegfried, Microcracks in
    crustal igneous rocks: physical properties, in The
    Nature and Physical Properties of the Earth's Crust,
    edited by J.G. Heacock, in press, 1976.